Kumar Selvarajoo

Immuno Systems Biology

A macroscopic approach for immune cell signaling

Springer

Systems Biology

Volume 3

Series Editor
Sangdun Choi

Kumar Selvarajoo

Immuno Systems Biology

A macroscopic approach
for immune cell signaling

Springer

Kumar Selvarajoo
Institute for Advanced Biosciences
Keio University
Tsuruoka, Yamagata, Japan

Preface

Systems biology is an emerging field integrating traditional and modern biological techniques with systemic approaches adopted from physics, mathematics, engineering, and computer science. Immuno systems biology specifically aims to study the host immune system in a more integrated manner as to how different cells and molecules participate at system levels to invoke the global proinflammatory response to fight against intruders.

In this book, I focus on the dynamic analyses of mammalian innate immune response to bacterial and viral perturbations using computational models based on simple physical rules. The majority of the book is concerned with interpreting population-level immune cell-signaling response in wild-type and mutant cells. The last few chapters are devoted to highlighting the complexities observed from recent single-cell analyses and their potential implications.

Geared toward a researcher with limited immunological and computational analytical experience, the book provides a broad overview to the subject and some instruction in basic computational, theoretical, and experimental approaches. The text is written in a nontechnical manner as an introduction for physicists, chemists, computer scientists, biologists, and immunologists who are interested in understanding the mammalian immune system as an integrated process. The book is the first of its kind to link complex immunological processes with simple computational analysis that can be reproduced with relative ease by the reader, as ample materials and references are provided. Overall, the book provides insights for a comprehensive view of the immune system.

No book is possible without the help of others. In this respect, I thank my students and colleagues who have supported this project in one way or another. Specifically, I wish to thank Vincent Piras, Kentaro Hayashi, Masaru Tomita, Masa Tsuchiya, Sangdun Choi, Shizuo Akira, Koichi Matsuo, Jun-ichiro Inoue, and Alessandro Guiliani. Most importantly, my dear wife Krisvene Kumar and children Lucas Kumar and Davisha Kumar are deeply appreciated for their never-ending love.

Yamagata, Japan   Kumar Selvarajoo

Contents

Chapter 1
Systems Biology of Population Cell Response

Living organisms are well known to survive, adapt, and even reproduce under adverse or challenging conditions. The ability to handle diverse environmental changes or perturbations is inherent to the large repertoire of genes, proteins, and metabolites that interact in response to external cues. The detection of extracellular or intracellular signals is channeled through molecular networks within and between cells, resulting in dynamic responses that process and disseminate information for necessary biological action, collectively, at an organismal level. The formation of biofilms, or cellular structures, through the aggregation and adhering of cells with one another (Fig. 1.1) by bacteria to enhance individual survivability to environmental attacks is a good example of interactive and adaptive behavior in biology [1, 2]. Mechanistically, how do living systems self-organize to achieve their purpose to survive?

Historically, biological processes have been understood from the microscopic point of view, and then progressed toward in vitro experimental techniques where cells are lysed and individual molecules are analyzed in a purified and isolated environment. In this way, the role of a single gene, protein, or metabolite has been studied, independently, which has provided a tremendous wealth of useful molecular information. For example, by comparing individual protein expression in different experimental condition (e.g., unstimulated versus stimulated), one is able to identify a role for the protein (Fig. 1.2).

Notably, cellular systems are in dynamic evolution involving numerous tightly controlled molecular interactions to achieve global behavior such as metabolism to balance the cell system energy requirement and the immune response for tackling invading pathogens. That is, treating biological entities in isolation cannot help us to understand the emergent, self-organizing, and complex spatiotemporal behavior of living systems (Fig. 1.1). The reliance on a single molecule reductionist approach to investigate evolving biological properties such as morphology, growth, metabolism, and disease progression is obviously deficient. Thus, for a comprehensive understanding of living systems behavior, there is clearly a need to assemble biological information from a single molecular level to global physiological response in dynamic fashion.

Fig. 1.1 *Formation of collective structures or biofilms from individual cells.* Certain cells in free-living bacteria secrete autoinducers or signaling molecules, which are recognized by the remaining cells, resulting in the synchronization of molecular processes to form global structures. The resultant biofilms are much more resistant to environmental attacks than individual cells (Adapted from Fuqua and Greenberg [1])
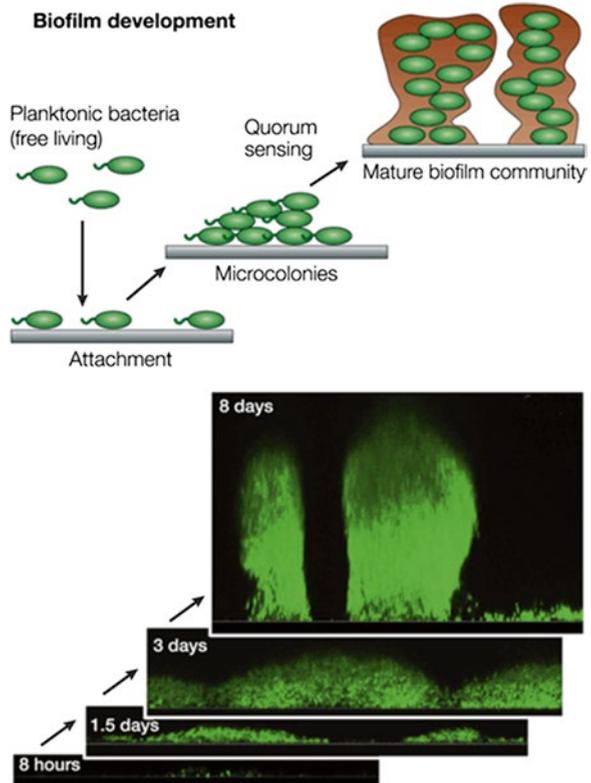
Fig. 1.2 *Tumor necrosis factor* (*TNF*)-*α and interleukin* (*IL*)-*1β in lipopolysaccharide* (*LPS*)-*stimulated murine macrophages.* Upregulation of these proteins reveals their significance as proinflammatory mediators. See Chap. 4 for details on *LPS*-stimulated response (Adapted from Kawai et al. [3])
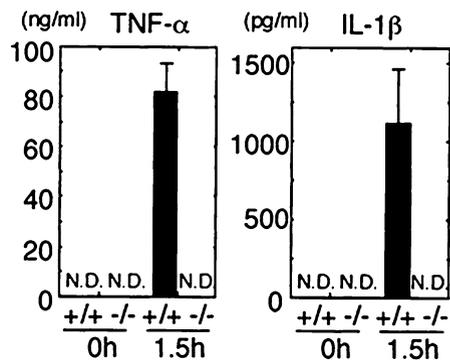
High-Throughput Biology

During the past two decades, in a quest to understand the system-level properties of living systems, the development and analysis of high-throughput experimental technologies for genomics [4], proteomics [5], and metabolomics [6] have proceeded. These methods generate large quantities of biological data at different scales crucial for unraveling the detailed molecular composition and complexity of living organisms.
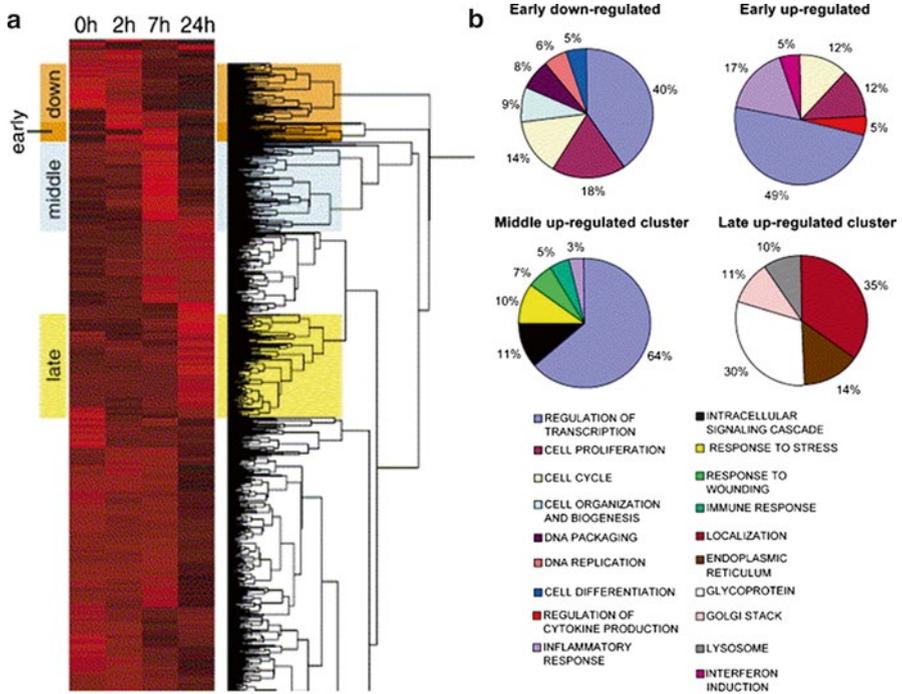
Fig. 1.3 *cDNA microarray response for LPS-stimulated macrophages*. (**a**) Statistically clustered temporal gene expression data show early, middle, and late upregulated gene clusters as well as downregulated cluster. (**b**) Annotation of major gene expression clusters (Adapted from Nilsson et al. [7])

For instance, what types of genes and how many are induced by the immune cells in response to invading pathogens? To address such elementary questions, the single-molecule approaches (whether traditional methods of Western or Northern blotting or modern techniques involving dynamic imaging) are rather tedious, time consuming, and not suitable when there are hundreds of responsive genes.

Using high-throughput complementary DNA (cDNA) microarrays [7], macrophages stimulated with lipopolysaccharide (*LPS*) induced almost 3,000 genes, belonging to diverse cellular processes, over a period of 24 h with distinct temporal response. The large number of responsive genes was clustered according to their response patterns, which revealed the activation of distinct signaling pathways over different time periods (Fig. 1.3a, b). Such valuable information for similar experimental conditions could not be revealed using a single-molecule approach (see Fig. 1.2 and Kawai et al. [3]).

In a study on *Escherichia coli* [8], to identify crucial genes for basic metabolic needs and to maintain the growth phenotype, the metabolism of wild-type cells was compared with 24 single-gene knockouts (KOs) belonging to crucial glycolysis and pentose phosphate pathways. Surprisingly, the study found that the messenger RNA (mRNA), proteins, and metabolite levels were stable for most KOs.

The remarkable robustness to perturbation was achieved through the rechanneling of metabolic fluxes by alternative routes within the system. Overall, through monitoring 130 metabolites, 57 proteins, and 85 mRNA transcripts, the investigation shed light on the global property, or robustness to perturbation, of *E. coli* to genetic and environmental attacks by adaptive metabolic flux distribution.

Scale-Free Property

The property of biological robustness has also been demonstrated by numerous other studies in which random deletions, mutations, or duplication of genes did not affect the overall network behavior or phenotypic outcome of living systems, revealing the persistence of stable behavior under diverse environmental and genetic perturbations [9–14]. On the other hand, biological systems have been shown to be fragile on a number of occasions and are vulnerable to attacks [15–18].

To understand the large-scale protein–protein interaction (*PPI*) of *Saccharomyces cerevisiae*, Rothberg and colleagues undertook two-hybrid screen measurements and detected about 1,000 putative interactions [19]. From these results, Barabási and coworkers constructed an organized map of the PPI networks (Fig. 1.4a) and found that the probability of a protein interacting with *k* other proteins followed a power law [20]. Subsequently and notably, this feature, which is commonly found in social behavior, finance, and internet, was also shown for other biological species [21]. That is, a few highly connected individuals (proteins) play a central role in mediating interactions among numerous, less-connected individuals (proteins), a property of a scale-free network (Fig. 1.4b). This postulation suggests that biological networks are not connected randomly but center around a small proportion of "hub" elements [18, 20, 21]. Thus, the removal of a relatively few highly linked "hub" molecules can lead to system failure.

For example, the activation of tumor necrosis factor (*TNF*)-receptor-associated factor 6 (TRAF6) occurs in several distinct signaling cascades. Targeted disruption of this molecule in mice has led to systemic failure and premature death [23, 24], suggesting that TRAF6 is a "hub" element. Similarly, "hub" molecules such as *cycA* or *cdk2* together with *p53* are also identified in the p53 network, a well-known tumor-suppressing pathway that controls apoptosis, the cell cycle, etc. [25]. Therefore, catastrophic failure can occur because of the loss of function of such a crucial family of "hub" molecules. On the whole, it is now convincing that the scale-free design of biological networks produces the inherent robustness and fragility to distinct environmental threats.

The high-throughput technologies have been crucial for revealing global properties and organizing principles. Although discovering the general organization of biological networks, robust to perturbation and fragile to targeted attacks obeying the scale-free or power law, is interesting from a scientific aspect, the comprehensive understanding of dynamic cellular behaviors and their control mechanisms still
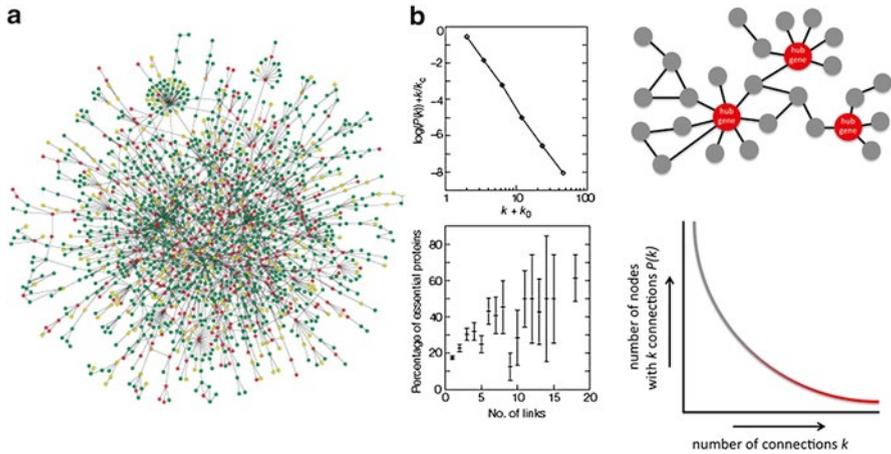
Fig. 1.4 *Scale-free architecture of biological networks*. (**a**) Protein–protein interaction (*PPI*) network found in *S. cerevisiae* obeys the power law (**b**), where increasing number of nodes decreases with increasing number of connections following $P(k) \sim k^{-\gamma}$. (Adapted from Jeong et al. [20] and van Kesteren et al. [22])

remains a big challenge. For example, how does a certain deterministic cell differentiation trajectory deviate into a cancerous state? To put high-throughput data together so that dynamic properties can be better understood requires analytical techniques. Thus, there is a crucial need to develop integrated theoretical and experimental approaches to discover, model, and understand the topological and dynamic properties of the various networks that, in quantifiable terms, control the behavior of living systems.

During the past few years, there has been active development of systemic methodologies to interpret dynamic cell behavior. This phenomenon has led to the creation of a rather new interdisciplinary field, called systems biology, inviting scientists across various fields to actively participate in joint research. Systems biology methods are based upon formalized theories, in most cases utilizing physicochemical laws, that combine with spatiotemporal high-throughput experimental data to provide better insights into the underlying molecular circuitry that controls complex behaviors of living systems.

Although interdisciplinary research involving biology has been in existence for a long time, in a rather ad hoc manner, only in the past 10 years have we witnessed a global consorted effort. In short, the goal of systems biology is to generate, integrate, and analyze biological data, both in time and in space, to (i) understand molecular cell circuit design in detail and to (ii) predict or interpret the response of a cellular system to various extracellular and intracellular perturbation, from genome to physiome. Thus, systems biology approaches, in principle, will enable us to better recognize the mechanisms for disease onset or the diversification of cell developmental process.

Simplifying Biological Complexity

A typical cellular system possesses large number of interacting genes, proteins, and metabolites. To consider them in their entirety, although desirable, is overwhelming and may not be a feasible task. Therefore, to reduce the complexity, it would be appropriate to modularize cellular systems into functions of biological interest [26]. Functional modules are compartments that can be considered as a system in isolation and have been widely used in engineering. In biology, this concept has been inherently observed for many years through in vitro experimental conceptualization: for example, the modularization of a gene regulation system for the determination of transcriptional machinery, signal transduction cascades for the understanding of extracellular signal propagation into the nucleus (Fig. 1.5a), and metabolic pathways for evaluating the distribution of fluxes to a given concentration perturbation (Fig. 1.5b). The ability to create functional modules through synthetic biology has become more popular in recent years [27].

Using the modularization concept, to date, distinct mathematical and computational methodologies have been developed and studied for almost all known biological networks. Popular quantitative approaches include kinetic methodologies based on chemical equilibrium and the law of mass action to analyze the dynamic response of biological networks [28, 29], multiscale modeling that integrates the interactions between different levels of spatial and temporal organization for understanding system behavior [30, 31], and stochastic models which investigate the temporal probability of switching from one state to another, or remaining in the native state, especially for cell fate decisions [32, 33]. Other approaches include stoichiometric methods, which consider reaction stoichiometry to identify reaction mechanisms [34, 35], singular value decomposition methods and statistical clustering for visualizing and identifying coordinated self-organizing behavior from high-throughput data [36, 37], and Bayesian network approaches for constructing biological network connectivity using probabilistic graphs [38, 39].

In one study, Hoffmann and colleagues were interested in elucidating the mechanisms behind distinct gene expression programs triggered by the same IKK–IκB–NF-κB signaling module for different stimuli in murine embryonic fibroblasts (MEF) [40]. They developed a simple mass-action response equations model with 24 molecular species and 70 reactions for the dynamic immune response induced by both tumor necrosis factor (TNF) and lipopolysaccharide (LPS) stimulation. Their model suggested that the mechanism for the rapid termination of IKK activity in TNF stimulation is the result of negative feedback control by post induction of A20, whereas the prolonged activation of IKK observed in LPS stimulation is caused by positive feedback of autocrine TNF signaling (Fig. 1.6). Although several hundreds of proteins are activated in TNF and LPS stimulation, it is remarkable that Hoffmann and colleagues were able to pinpoint a simple regulatory mechanism of perceived complex mammalian immune responses using only a limited number of protein reaction species.
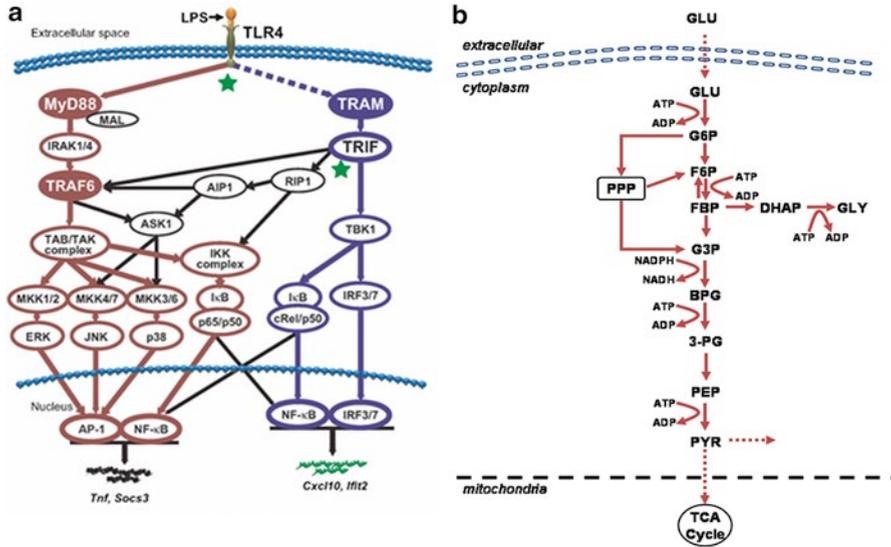
Fig. 1.5 *Functional modularization of biological networks*: Toll-like receptor 4 (*TLR4*) (**a**) and glycolysis (*Glu*) (**b**) schematic pathways
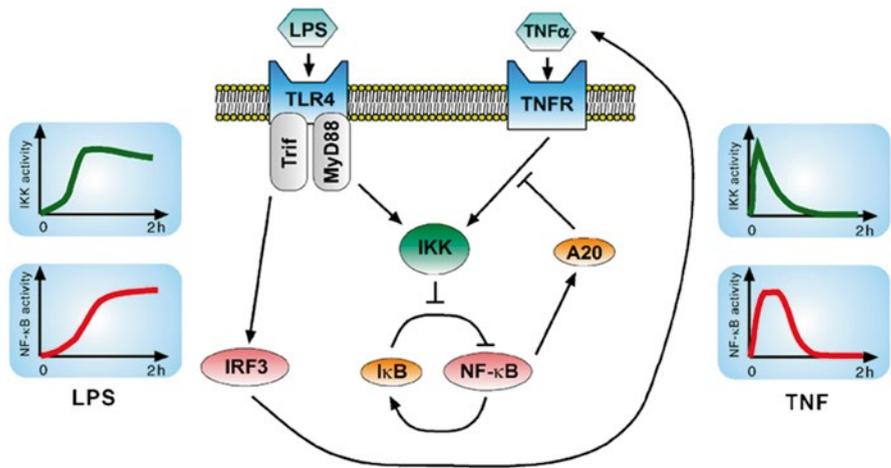
Fig. 1.6 *Negative and positive feedback loops regulated by IKK activity in stimulus-specific manner*. Schematic dynamic profiles of IKK and nuclear NF-κB activity show distinct temporal profiles for LPS (*left*) and TNF (*right*) stimulation. The temporal dynamics was interpreted with the aid of a computational model to suggest that TNF triggers the A20-mediated negative feedback loop whereas LPS induces a positive feedback loop through TNF pathways [40] (Adapted from Cheong et al. [41])
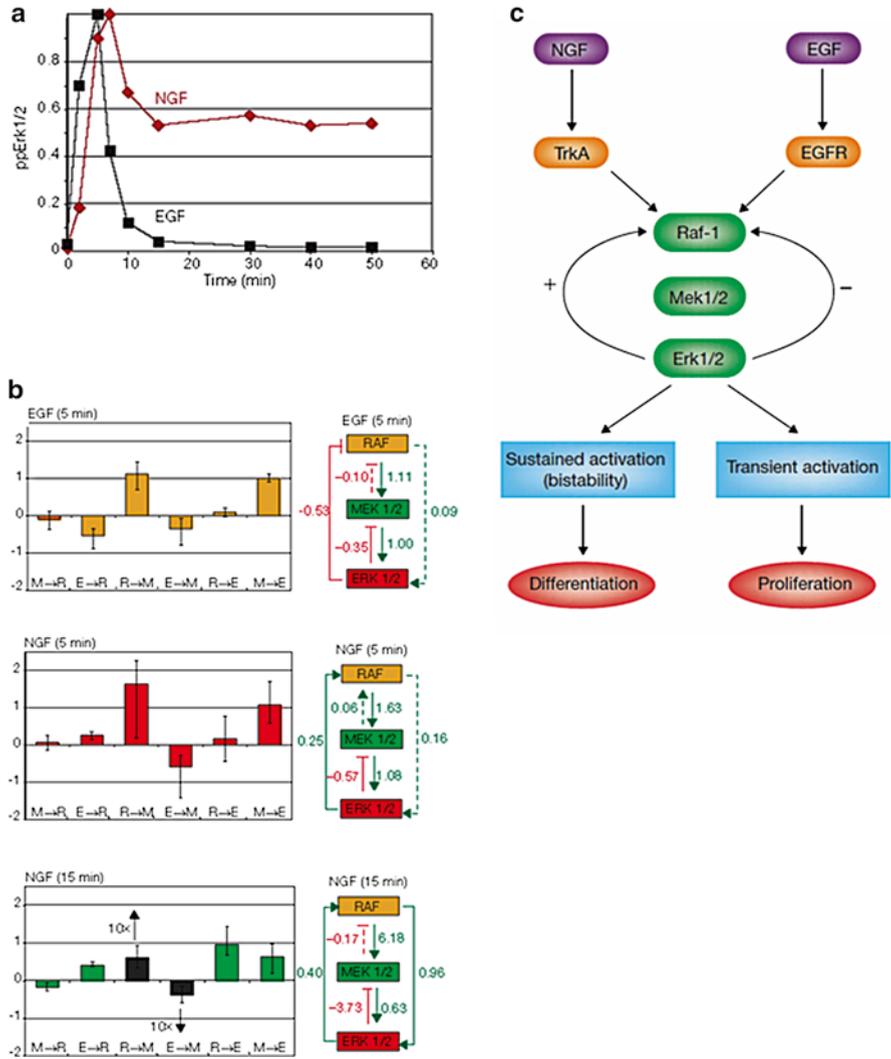
Fig. 1.7 *Distinct dynamic Erk1/2 activation in epidermal growth factor (EGF) and nerve growth factor (NGF) stimulation.* (**a**) Normalized phosphorylated Erk1/2 (ppErk1/2) activity for EGF (*black*) and NGF (*red*) stimulation. (**b**) The modular response approach computes local response coefficients that were used to convert the connectivity of the MAPK module. (**c**) NGF requires positive feedback for sustained activation whereas EGF requires negative feedback for transient response (Adapted from Werner et al. [40])

In a similar way to the IKK–IκB–NF-κB modular approach, in another study, Santos et al. used a computational model based on the modular response approach (MRA) to reveal the distinct wiring of the conserved MAPK signaling to epidermal growth factor (EGF) and nerve growth factor (NGF) stimuli (Fig. 1.7a) [42]. The MRA is based on ordinary differential equations with steady-state assumptions

of biochemical networks over time. A matrix of (local) response coefficients is quantified to assess the nature of intermodular interactions [43].

The use of MRA interpreted the experimental profiles where EGF activates ERK transiently through negative feedback from ERK to RAF, and NGF sustains ERK activity via positive feedback using the same axis (Fig. 1.7b, c). Thus, from the systems biology studies of IKK–IκB–NF-κB and MAPK signaling modules, it is clearly evident that a simple predictable response can be obtained despite the vast complexity of biological networks within self-organizing living systems. That is, although large numbers of molecules are packed within cells, suggesting a vast possibility of combinatorial outcome, biological responses for a given stimulus occur through specific functional modules obeying simple rules (see the following chapter).

In summary, the consideration of functional modules in biology has led to the simplification of cellular response and has provided useful network causality or behavior. This development may not be surprising as several other fields such as physics, chemistry, and engineering also display modular characteristics in which, without knowing most details of system architecture or parameter values, very useful knowledge about system dynamics is revealed. Here, the law of nature has been shown to constrain the system so that even with limited information useful hidden properties can be revealed.

For example, without knowing the details of wind dynamics, the behavior of an aircraft in diverse atmospheric conditions can be predicted combining the laws of mass, momentum, and energy conservation. Although such macroscopic laws will break down in certain conditions, such as in turbulent flow, or high speeds (greater than the speed of sound) when secondary effects such as kinetic heating complicate matter, nevertheless, the success of air and space travel is primarily the result of the discovery of physical laws. Do such laws of nature also operate in biology [44], and can biologists take advantage of the resultant simplicity to develop formalized theory? This book aims to shed light on the simplicities found within biological responses, providing a simple method to analyze their dynamics using the law of information (mass flux) conservation.

References

1. Fuqua C, Greenberg EP (2002) Listening in on bacteria: acyl-homoserine lactone signalling. Nat Rev Mol Cell Biol 3:685–695
2. Smith PA, Romesberg FE (2007) Combating bacteria and drug resistance by inhibiting mechanisms of persistence and adaptation. Nat Chem Biol 3:549–556
3. Kawai T, Adachi O, Ogawa T, Takeda K, Akira S (1999) Unresponsiveness of MyD88-deficient mice to endotoxin. Immunity 11:115–122
4. Pollack JR, Perou CM, Alizadeh AA, Eisen MB, Pergamenschikov A, Williams CF, Jeffrey SS, Botstein D, Brown PO (1999) Genome-wide analysis of DNA copy-number changes using cDNA microarrays. Nat Genet 23:41–46
5. Anderson NL, Anderson NG (1998) Proteome and proteomics: new technologies, new concepts, and new words. Electrophoresis 19:1853–1861
6. Weckwerth W (2003) Metabolomics in systems biology. Annu Rev Plant Biol 54:669–689

7. Nilsson R, Bajic VB, Suzuki H, di Bernardo D, Björkegren J, Katayama S, Reid JF, Sweet MJ, Gariboldi M, Carninci P, Hayashizaki Y, Hume DA, Tegner J, Ravasi T (2006) Transcriptional network dynamics in macrophage activation. Genomics 88:133–142

8. Ishii N, Nakahigashi K, Baba T, Robert M, Soga T, Kanai A, Hirasawa T, Naba M, Hirai K, Hoque A, Ho PY, Kakazu Y, Sugawara K, Igarashi S, Harada S, Masuda T, Sugiyama N, Togashi T, Hasegawa M, Takai Y, Yugi K, Arakawa K, Iwata N, Toya Y, Nakayama Y, Nishioka T, Shimizu K, Mori H, Tomita M (2007) Multiple high-throughput analyses monitor the response of *E. coli* to perturbations. Science 316:593–597

9. Kitano H (2004) Biological robustness. Nat Rev Genet 5:826–837

10. Barabasi AL, Oltvai ZN (2004) Network biology: understanding the cell's functional organization. Nat Rev Genet 5:101–113

11. Bennett MR, Hasty J (2008) Systems biology: genome rewired. Nature 452:824–825

12. Barkai N, Leibler S (1997) Robustness in simple biochemical networks. Nature 387:913–917

13. Alon U, Surette MG, Barkai N, Leibler S (1999) Robustness in bacterial chemotaxis. Nature 397:168–171

14. Rao CV, Arkin AP (2001) Control motifs for intracellular regulatory networks. Annu Rev Biomed Eng 3:391–419

15. Stromberg SP, Carlson J (2006) Robustness and fragility in immunosenescence. PLoS Comput Biol 2:e160

16. Lemoine FJ, Degtyareva NP, Lobachev K, Petes TD (2005) Chromosomal translocations in yeast induced by low levels of DNA polymerase: a model for chromosome fragile sites. Cell 120:587–598

17. Carlson JM, Doyle J (2002) Complexity and robustness. Proc Natl Acad Sci USA 99: 2538–2545

18. Albert R, Jeong H, Barabasi AL (2000) Error and attack tolerance of complex networks. Nature 406:378–382

19. Uetz P, Giot L, Cagney G, Mansfield TA, Judson RS, Knight JR, Lockshon D, Narayan V, Srinivasan M, Pochart P, Qureshi-Emili A, Li Y, Godwin B, Conover D, Kalbfleisch T, Vijayadamodar G, Yang M, Johnston M, Fields S, Rothberg JM (2000) A comprehensive analysis of protein–protein interactions in *Saccharomyces cerevisiae*. Nature 403:623–627

20. Jeong H, Mason SP, Barabási AL, Oltvai ZN (2001) Lethality and centrality in protein networks. Nature 411:41–42

21. Vidal M, Cusick ME, Barabási AL (2011) Interactome networks and human disease. Cell 144:986–998

22. van Kesteren RE, Mason MR, Macgillavry HD, Smit AB, Verhaagen J (2011) A gene network perspective on axonal regeneration. Front Mol Neurosci 4:46

23. Naito A, Azuma S, Tanaka S, Miyazaki T, Takaki S, Takatsu K, Nakao K, Nakamura K, Katsuki M, Yamamoto T, Inoue J (1999) Severe osteopetrosis, defective interleukin-1 signalling and lymph node organogenesis in TRAF6-deficient mice. Genes Cells 4:353–362

24. Kobayashi T, Walsh MC, Choi Y (2004) The role of TRAF6 in signal transduction and the immune response. Microbes Infect 6:1333–1338

25. Dartnell L, Simeonidis E, Hubank M, Tsoka S, Bogle ID, Papageorgiou LG (2005) Robustness of the p53 network and biological hackers. FEBS Lett 579:3037–3042

26. Hartwell LH, Hopfield JJ, Leibler S, Murray AW (1999) From molecular to modular cell biology. Nature 402:C47–C52

27. Purnick PE, Weiss R (2009) The second wave of synthetic biology: from modules to systems. Nat Rev Mol Cell Biol 10:410–422

28. Blair RH, Trichler DL, Gaille DP (2012) Mathematical and statistical modeling in cancer systems biology. Front Physiol 3:227

29. Selvarajoo K, Tomita M, Tsuchiya M (2009) Can complex cellular processes be governed by simple linear rules? J Bioinform Comput Biol 7:243–268

30. Voss-Böhme A (2012) Multi-scale modeling in morphogenesis: a critical analysis of the cellular Potts model. PLoS One 7:e42852

31. Yamada Y, Forger D (2010) Multiscale complexity in the mammalian circadian clock. Curr Opin Genet Dev 20:626–633
32. Strasser M, Theis FJ, Marr C (2012) Stability and multiattractor dynamics of a toggle switch based on a two-stage model of stochastic gene expression. Biophys J 102:19–29
33. Stockholm D, Edom-Vovard F, Coutant S, Sanatine P, Yamagata Y, Corre G, Le Guillou L, Neildez-Nguyen TM, Pàldi A (2010) Bistable cell fate specification as a result of stochastic fluctuations and collective spatial cell behaviour. PLoS One 5:e14441
34. Baart GJ, Martens DE (2012) Genome-scale metabolic models: reconstruction and analysis. Methods Mol Biol 799:107–126
35. Schilling CH, Palsson BO (1998) The underlying pathway structure of biochemical reaction networks. Proc Natl Acad Sci USA 95:4193–4198
36. Yeung MKS, Tegner J, Collins JJ (2002) Reverse engineering gene networks using singular value decomposition and robust regression. Proc Natl Acad Sci USA 99:6163–6168
37. Alter O, Brown PO, Botstein D (2000) Singular value decomposition for genome-wide expression data processing and modeling. Proc Natl Acad Sci USA 97:10101–10106
38. Friedman N, Linial M, Nachman I, Pe'er D (2000) Using Bayesian networks to analyze expression data. J Comput Biol 7:601–620
39. Friedman N (2004) Inferring cellular networks using probabilistic graphical models. Science 303:799–805
40. Werner SL, Barken D, Hoffmann A (2005) Stimulus specificity of gene expression programs determined by temporal control of IKK activity. Science 309:1857–1861
41. Cheong R, Hoffmann A, Levchenko A (2008) Understanding NF-kappa-B signaling via mathematical modeling. Mol Syst Biol 4:192
42. Santos SD, Verveer PJ, Bastiaens PI (2007) Growth factor-induced MAPK network topology shapes Erk response determining PC-12 cell fate. Nat Cell Biol 9:324–330
43. Bruggeman FJ, Westerhoff HV, Hoek JB, Kholodenko BN (2002) Modular response analysis of cellular regulatory networks. J Theor Biol 218:507–520
44. Selvarajoo K, Tomita M (2013) Physical laws shape biology. Science 339:646

Chapter 2
Perturbation-Response Approach for Biological Network Analysis

A cell contains thousands of genes/proteins/metabolites in a highly inhomogeneous intracellular environment with spatiotemporal effects of molecular crowding and diffusion. The molecules are highly interconnected, leading to complex networks. Hence, there is precedence that all molecular interactions with their detailed reaction kinetics and spatial organization are required to be known for the proper understanding of biological responses. In fact, the goal of the human genome project is to first generate a complete parts list of genetic materials within cells and, second, from it construct the detailed regulatory features that connect them [1, 2]. However, even in such perceived complexity involving myriad interacting components, simple mass-action models using a limited set of crucial molecules, constituting functional biological modules, were successfully used to interpret dynamic responses (see Chap. 1). How can such simplicity be held within a complex system?

For a long time, biological networks have been investigated on a much smaller scale through in vitro experiments (e.g., the 10-step reaction analysis of glycolysis; see Fig. 1.5b). This approach was mainly in the hope to understand and control all reaction kinetics within the entire known connectivity in detail. In most circumstances, the investigations considered a 'closed' system, where there was no exchange of material between the internal and external environments. Hence, chemical and thermal equilibrium can be assumed, and as a result, the law of mass action is expected to work within the system. In other words, the approach describes a well-mixed, homogeneous, and isothermal environment where each reaction in the network is connected through first-order, higher-order mass-action or enzyme kinetic equations, depending on the knowledge gained for an individual reaction (Box 2.1).

Most, if not all, studies adopting in vitro experiments determine the parameter values of reaction species for computational modeling from an artificial environment where the species are deliberately purified from its physiological neighbors. This approach is because, until now, in vivo kinetic parameters could be reliably measured using current experimental technologies. Notably, there have been various reports that claim the kinetic parameters determined through in vitro and in vivo experiments can differ by several orders of magnitude [3]. As a result, when

Box 2.1 Mass-Action Kinetics

A chemical system is perturbed from a stable steady state. When the system subsequently returns to its original state, the system is said to be in equilibrium. For example, heating water at room temperature and subsequently removing the heat source results in the decay of the water temperature to its original reading. This event happens in a 'closed' system where external conditions, such as pressure, energy, or mass, do not enter or leave the system that is in cooling.

Let us consider a simple case involving only the decay process, that is, the point onward when a heat source is removed. The temperature (T) changes over time following Newton's law of cooling:

$$\frac{dT}{dt} = -k[T - T_0]$$

where T_0 is the room temperature and k is the rate of cooling. The minus sign indicates temperature drop in time.

Now consider a closed chemical reaction of molecular species A into B:

$$A \rightarrow B$$

The arrow indicates the equilibrium state lies far to the right, that is, the reverse reaction ($B \rightarrow A$) proceeds only at an infinitesimal extent. For every species B formed (concentration units in moles), an A species disappears:

$$\frac{d[B]}{dt} = \frac{-d[A]}{dt} = k_1[A]$$

The constant k_1 is called the rate constant and has the unit of per second. The rate constant provides a direct measure of how fast this reaction is occurring. The higher the k_1 value, the faster the reaction. This type of reaction is called a first-order reaction, as its rate depends on the first power of the reactant concentration. A second-order reaction occurs typically when two species react to form another species. An example:

$$2A \xrightarrow{k_2} A_2$$
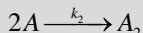
The rate of such a reaction is proportional to the second power of the concentration of reactant, for the reaction can occur only when two molecules collide:

$$\frac{-d[A]}{dt} = k_2[A]^2$$

where k_2 is the second-order rate constant. It has dimensions of $(\text{mol/L})^{-1}\,\text{s}^{-1}$.

Box 2.1 (continued)

It follows that for any system in chemical equilibrium, the rate of an elementary reaction is proportional to the product of the concentrations of the reacting species.

Enzyme Kinetics

For reactions that require the aid of other species, such as enzymes that enhance catalytic reactions, the mechanism to account for such reactions assumes that the species A combines with the species E in a reversible manner to give complex EA, which then dissociates reversibly or reacts irreversibly to produce B while leaving E unchanged.

$$E + A \underset{k_{-1}}{\overset{k_1}{\longleftrightarrow}} EA \xrightarrow{k_{cat}} E + B$$

In this case, the rate of B formation can be shown to be [9]:

$$\frac{dB}{dt} = \frac{V_{max}[A]}{[A] + K_M}$$

where $V_{max} = k_{cat}[E]_t$ and $K_M = \dfrac{k_{cat} + k_{-1}}{k_1}$

The reaction rate increases with increasing $[A]$, approaching an asymptote at V_{max}, when all enzyme is bound to A. $[E]_t$ is the total enzyme concentration and k_{cat} is the maximum number of enzymatic reactions catalyzed per second.

There are various forms of enzyme kinetics, depending on the types of intermediates or cofactors affecting the overall reactions [9].

combining these errors into the model, the final predictions could differ by several orders of magnitude. For example, the steady-state concentration of the glycolytic metabolite 3-phosphoglycerate in *Trypanosoma brucei* was underpredicted by an order of seven [4]. Hence, despite modularizing a small functional network in biology, the computational prediction of steady-state glycolytic metabolite concentrations may not reflect realistic in vivo values because of the lack of accuracy in determining kinetic reaction parameter values using an in vitro system.

Moreover, the kinetic approach requires (i) a priori knowledge of all detailed connectivities of reacting species and (ii) the assumption of steady-state conditions. This requirement highly limits their applicability for analyzing a cellular system where the knowledge of network topology is sparse, for example, in signal transduction and gene regulatory networks, and for interpreting non-steady-state or

complex dynamic response to external perturbation. Therefore, there have been numerous efforts to find alternative theoretical and computational methodologies that would analyze complex dynamics and overcome the difficulty of not having enough in vivo biological data.

One popular method that overcomes the issue of parameter reliability is the flux-balance analysis (FBA) [5]. Here, only the reaction topologies or stoichiometry of the network need be known. Constraints are introduced by the stoichiometric coefficients in the system for the optimization of certain biological function, such as growth or production of certain compounds. Although the FBA requires the assumption that metabolite concentrations remain at the steady state for analysis, it has been successfully used to interpret important physiological functions of a living cell. For example, Palsson and colleagues experimentally verified their prediction for the primary carbon source and oxygen uptake rates for maximal cellular growth in *Escherichia coli* [6]. Nevertheless, the FBA requires steady-state response and connectivity of all species in a biological network to be known, which highly limits its applicability for signaling or gene network analysis.

On the other hand, as mentioned in Chap. 1, the use of a simple mass-action model in a highly limited module of tumor necrosis factor (TNF), lipopolysaccharide (LPS), epidermal growth factor (EGF), and nerve growth factor (NGF) signaling has produced very useful insights into the regulation of key transcription factors and their gene expressions. These achievements may seem to contradict studies that aim to understand the details of the entire biological part list before interpreting complex dynamics. The truth, obviously, depends on the type of biological questions that one seeks to find solution. In the case of the signaling studies mentioned, the goal was to understand how the IKK and MAPK module responded to different stimuli. The investigations demonstrated that it was not necessary to know the detailed dynamics of each signaling species activated for each stimulus to understand their core regulatory features. So, why is it that not all details are required to understand IKK and MAPK modular response or to understand the physiological growth rate of *E. coli*?

The answer may lie within the organizing principles observed for biological networks. Chapter 1 highlighted that biological networks are organized in a scale-free manner, where controlling the 'nodes' would not overtly change the stable response of the network, while removing the 'hubs' is likely to produce an unstable or deleterious response. In a pioneering work on understanding *E. coli* chemotactic behavior, Leibler and colleagues showed that the adaptation precision of bacterial chemotaxis was insensitive to the large variation of its network parameter values [7, 8]. This mechanism, therefore, allows *E. coli* to display robust behavior to a wide range of attractant and repellent concentrations. However, at the same time, other properties, such as adaptation time and steady-state tumbling frequency, were variable with stimulant concentration. Overall, the work concludes that the core network structure does not depend on the precision of its parameter values. This important finding is fundamental to the success of the numerous simple models, such as those for IKK and MAPK modules or for carbon metabolism, where it is the network structure rather than reaction kinetics that is crucial for the robust and repeatable behavior of the system.

In this chapter, and for most of this book, we focus on the "perturbation-response" approach, where instead of trying to understand the microscopic details of the detailed kinetics of each reaction, a macroscopic or 'top-down' view of the biological network behavior is used to understand the system structure and behavior. More technically, instead of measuring each reaction kinetics to investigate biological network response, one can alternatively observe the dynamic patterns of the network species to a given perturbation, and then directly determine the response parameter values for the model.

The Perturbation-Response Approach

Let a fixed perturbation be given to one of the species in a cellular system: this will result in the propagation of response waves among those species that interact. Obviously, those species that are not connected will remain at baseline or steady-state levels. Figure 2.1 schematically illustrates a hypothetical system with five species. Here, the perturbation of X_1 results in the response of species X_3 and X_5 only, suggesting the existence of connectivity between the three species. Next, by analyzing the time to reach peaks, the actual peak levels, and the decay rates, the order of causal relationships or connectivity between the species can be determined.

For example, in a closed system, if the concentration of (i) X_1 decreases only, (ii) X_3 increases, go through a maximum, and decreases, and (iii) X_5 increases only, by the law of mass flow conservation it can be shown that the connectivity is a linear chain of reactions: $X_1 \rightarrow X_3 \rightarrow X_5$ (Fig. 2.1). That is, the temporal order of responses can yield the causal connectivity of the species in the reaction mechanism.

To illustrate this further, let us construct a linear chain of reactions for Y species ($Y_1 \rightarrow Y_2 \rightarrow Y_3 \rightarrow \ldots \rightarrow Y_{N-1} \rightarrow Y_N$) using first-order mass-action response equations. By applying a pulse perturbation to the concentration of the first species, Y_1, we observe the propagation of response waves along the pathway (Fig. 2.2). The experiments
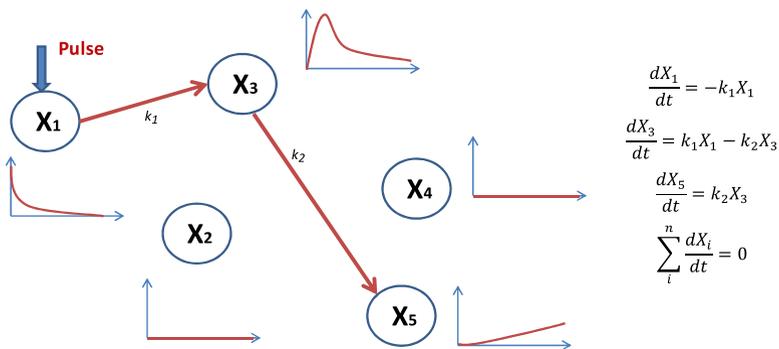
Fig. 2.1 *Essence of the perturbation-response approach.* The summation of all reaction rates will be zero in a mass-conserved closed system

Fig. 2.2 *Propagation of response waves*. Temporal profiles of species concentration in a linear chain reaction network for pulse perturbation of species Y_1 (with $N=7$; see text). The units are arbitrary, scaled by rate coefficients
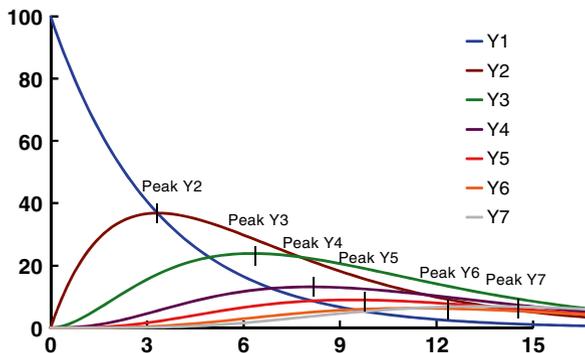
preserve the total input and output fluxes. Under such conditions, a linear super-position of propagation response waves connects the species between input and output fluxes. Thus, simple linear rules can be derived for the system, notably, (1) the time to reach peak values (*Peak Y2*, *Peak Y3*, etc., in Fig. 2.2) increases and its amplitude decreases as one moves down the reaction network, unless there are other features such as feedback reactions; (2) the initial response gradient can be used to determine the location of a reactant species in a network, that is, the steepest gradient is the closest to the perturbed reactant species and the lowest gradient is the farthest; (3) reactant species that are not connected to the system do not show any response profile; and (4) as the law of mass conservation is used for pulse propagation, the sum of all species deviations from the steady state (weighted by stoichiometric coefficients) is constant. Therefore, it can help to determine the correct stoichiometric coefficients [10].

Despite the simplicity of the approach, linear response is visually apparent in the dynamic response profiles of several intracellular molecules activated in glycolysis, EGF- and TLR3/4 signaling to their respective perturbations (Fig. 2.3a–d). In other words, the perturbation-response analysis clearly provides evidence that complex biological networks could be governed by simple mass-action response equations, resulting in the linear superposition of propagation response waves.

To understand why biological network dynamics can follow linear response, let us reconsider pulse perturbation, $(\alpha, 0)$ at $t=0$, given to a simple two-species chain governed by first-order mass-action equations; $\mathbf{X}=(X_1, X_2)$: $X_1 \xrightarrow{k_1} X_2 \xrightarrow{k_2}$. The perturbation wave $\delta\mathbf{X}=(\delta X_1, \delta X_2)$, applied to the system with rate constants k_1 and k_2 for X_1 and X_2, where X_1 has k_1 as depletion and X_2 has k_1 as formation and k_2 as depletion, can be represented by

$$\frac{d\delta\mathbf{X}}{dt} = \begin{pmatrix} -k_1 & 0 \\ k_1 & -k_2 \end{pmatrix} \delta\mathbf{X} \tag{2.1}$$
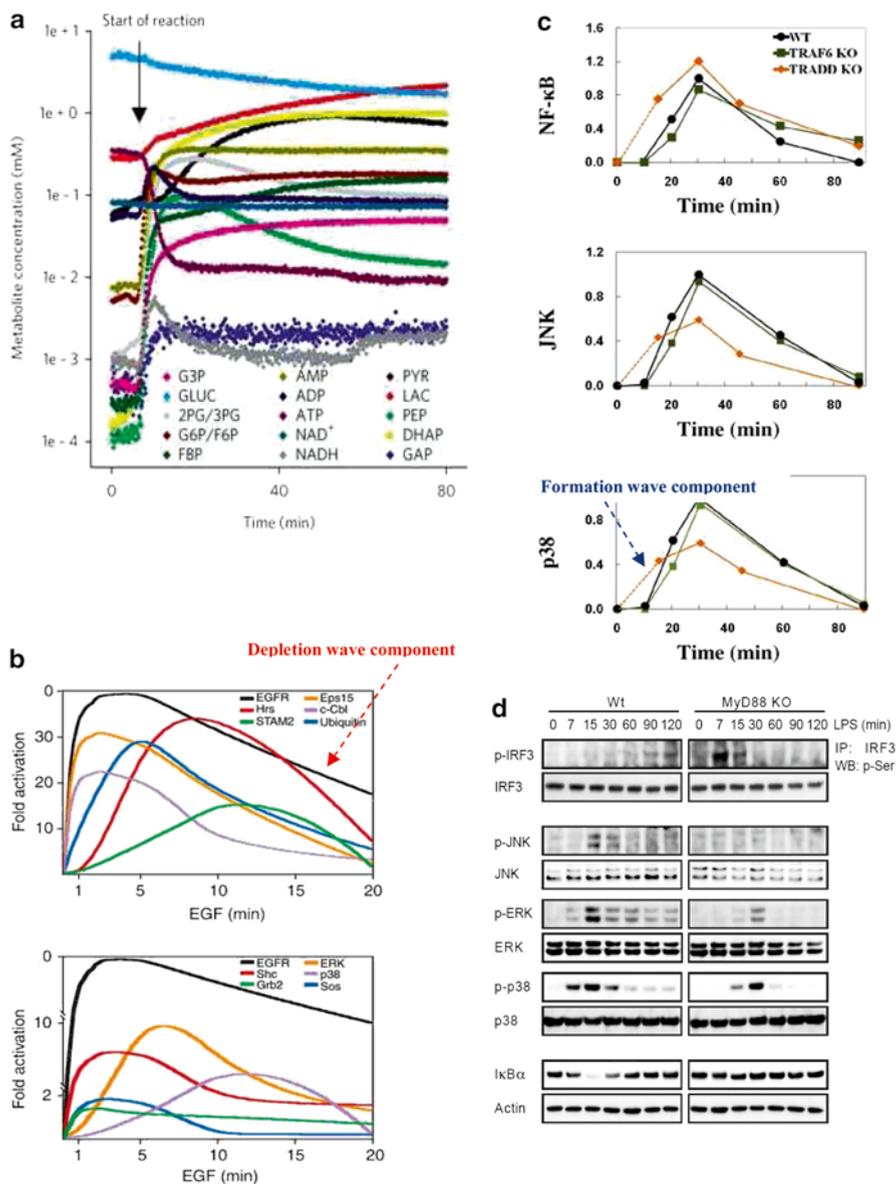
Fig. 2.3 *The response of biological pathways to upstream perturbation shows deterministic downstream formation and depletion waves.* Glycolysis (**a**), epidermal growth factor (EGF)-signaling (**b**), TLR3-signaling (**c**), and TLR4-signaling (**d**) dynamics show activation and deactivation following formation and depletion waves ((**a**) Adapted from Bujara et al. [11]; (**b**) adapted from Blagoev et al. [12]; (**c**) adapted from Helmy et al. 13]; (**d**) adapted from Selvarajoo et al. [14])

With initial conditions, $\mathbf{X}_0$, solving Eq. 2.4 yields the sum-of-exponentials:

$$\delta X_1 = \alpha e^{-k_1 t} \tag{2.2}$$

$$\delta X_2 = \frac{k_1}{k_2 - k_1}(e^{-k_1 t} - e^{-k_2 t}) \tag{2.3}$$

Factorize Eq. 2.3 with respect to $e^{-k_1 t}$ if $k_2 > k_1$ (or $e^{-k_2 t}$ if $k_1 > k_2$) and obtain:

$$\delta X_2 = \frac{k_1}{k_2 - k_1}(1 - e^{-(k_2 - k_1)t})e^{-k_1 t} \tag{2.4}$$

Equation 2.4 can be rewritten to constitute both the *formation* and *depletion wave terms*:

$$\delta X = \alpha \times \left(1 - e^{-p_1 t}\right) \times e^{-p_2 t}$$

Perturbation   Formation wave   Depletion wave   (2.5)

where α represents the amount of perturbation and p_1 and p_2 represent the measure of formation and depletion response propagation waves, respectively. In general, p_1 and p_2 are not equal to k_1 and k_2, respectively, and are determined by fitting with experimental data. Thus, the formation and depletion terms observed for several biological network responses (Fig. 2.3) are likely to have their origins from first-order or linear response equations.

The Origins of Linear Response

To investigate the origins of formation and depletion waves in the response of various complex biological networks outlined so far, let a stable network consisting of n species be perturbed from the reference steady state. In general, the resultant changes in the concentration of species are governed by the kinetic evolution equation:

$$\frac{\partial X_i}{\partial t} = F_i\left(X_1, X_2, .., X_n\right), i = 1, .., n \tag{2.6}$$

where the corresponding vector form of Eq. 2.1 is $\frac{\partial \mathbf{X}}{\partial t} = \mathbf{F}(\mathbf{X})$. $\mathbf{F}$ is a vector of any nonlinear function including diffusion and reaction of the species vector $\mathbf{X} = (X_1, X_2, .., X_n)$, which represents activated concentration levels of the reaction species (hence the partial derivative used). The response to perturbation can be written by $\mathbf{X} = \mathbf{X}_0 + \delta \mathbf{X}$, where $\mathbf{X}_0$ is the reference steady-state vector and $\delta \mathbf{X}$ is the relative response from steady states ($\delta \mathbf{X}_{t=0} = \mathbf{0}$).

The generally nonlinear kinetic evolution equation (Eq. 2.6) can be approximated or linearized by using the Taylor series:

$$\frac{\partial \delta \mathbf{X}}{\partial t} = \frac{\partial F(\mathbf{X})}{\partial \mathbf{X}}\bigg| \delta \mathbf{X} + \frac{\partial F^2(\mathbf{X})}{\partial \mathbf{X}^2}\bigg| \delta \mathbf{X}^2 + \ldots \qquad (2.7)$$

As the general volume of perturbing substance is usually very small (order of 1 %) compared to the total volume of cells that are perturbed, now consider a small perturbation around the steady state in Eq. 2.7, in which higher-order terms become negligible, and resulting in the approximation of the first-order term. In vector form $\frac{d\delta \mathbf{X}}{dt} \cong \frac{\partial F(\mathbf{X})}{\partial \mathbf{X}}\bigg|_{X=X_0} \delta X$ (note the change from partial derivative to total derivative of time), where the zero-order term $F(X_0)=0$ at the steady-state X_0 and the *Jacobian* matrix, or linear stability matrix, is $J = \frac{\partial F(\mathbf{X})}{\partial \mathbf{X}}\bigg|_{X=X_0}$. The elements of J, based on the initial activation topology, are chosen by fitting δX with corresponding experimental profiles. Hence, the amount of response (flux propagated) along a biological pathway can be approximated using *first-order mass-action response*, i.e., $\frac{d\delta \mathbf{X}}{dt} = \mathbf{J}\delta \mathbf{X}$. That is, the basic principle so far suggests that the response rate of species in a mass-conserved system at an initial steady state can be approximated by the first-order mass-action response equation, given a small perturbation to one or more species.

Note that Jacobian matrix elements (or response coefficients) can represent not only reaction information but also spatial information such as diffusion and transport mechanisms. Thus, each species in the perturbation-response model can represent a molecule, a different modified state of a molecule (e.g., ubiquitinated state), or a molecular process such as diffusion or endocytosis. That is, each species in the biological network does not necessarily represent a specific molecular species. For illustration, in a pathway $q1 \rightarrow q2 \rightarrow q3 \rightarrow q4 \rightarrow q5$, $q1$ to $q5$ can each be a different protein or the same protein at different stages in signaling, for example, $q1$ being internalized ($q2$), transported to a different organelle ($q3$), ubiquitinated ($q4$), and become part of a protein complex ($q5$).

Thus, in contrast to bottom-up kinetic models, which use fixed network topology, the perturbation-response approach considers the network as a sequence of events rather than just molecular species. As molecular networks are largely not fully understood, this difference is crucial as it prevents rigidly fixing the network topology, and allows it to be modified according to experimental data so as to prevent overfitting problems and, as a consequence, identify novel features of biological networks.

In addition, as cellular processes involve a large number (thousands) of intracellular molecular interactions, it is currently not plausible to model the dynamics of all possible reactions with the generally limited data. To overcome such difficulties, this approach permits the lumping of several molecules into a species, and the

resultant averaging nature of the response equations does not require detailed kinetics. This postulation will become clearer in later chapters where the lumping of several molecules in signaling networks does not distort the overall properties of the system response.

Limitations of Linear Response Approach

As with all modeling approaches, there are certain limitations that require mentioning. First, the linear response approach does not comprehensively model the details of the kinetics of an individual signaling reaction. Second, the small perturbation assumption leading to the deterministic first-order mass-action equations represents an average cell response in a well-mixed homogeneous environment. Hence, the approach cannot be used to study single-cell stochastic behavior or oscillatory dynamics in a heterogeneous environment (see Chap. 9). Third, the model predictions show relative, and not absolute, activation levels. Fourth, the first-order response may be used only for a relatively short primary response period (up to 2 h), where secondary effects such as autocrine or paracrine feedback regulations are usually not significant. Fifth, the first-order response is best suited for a fixed perturbation strategy; that is, the model cannot be tested with the same parameter values across a variable range (volume) of perturbing stimuli. In that situation, a different set of parameters or network features (e.g., feedback loop) could suffice for different levels of perturbation. Although linear response is observed for numerous cellular responses, their application may not necessarily be applicable in several other cellular processes, such as in interpreting cell fate decision or neural signaling, where nonlinear approaches are required [15, 16].

Nevertheless, the linear response approach is not restricted to specific pathways. It can be applied to model any pathways that experimentally display formation and depletion waves (Fig. 2.3). Although the position of a particular species in a reaction network requires all related species be identified and measured, simple models using linear response that lump several molecular species can still provide useful information in revealing overt novel network features, for example, the identification of distinct IKK–IκB–NF-κB network wirings in LPS, TNF, EGF, and NGF stimulation (see Chap. 1). More examples with better details are shown in the following chapters through the investigations of various innate immune signaling networks, where several missing components from the current knowledge of their network species are revealed.

In the following chapter, Chap. 3, we introduce some basic aspects in immunology and Toll-like receptor (TLR) signaling. Chapters 4, 5, 6, and 7 consider the use of the linear response approach to analyze the dynamics of TLR4 (Chaps. 4 and 5), TLR3 (Chap. 6), TNF (Chap. 7), and TRAIL (Chap. 8) signaling. Chapter 9 onwards introduce the issue of nonlinearities observed in biology and set the tone for future systems biology research.

References

1. Venter JC et al (2001) The sequence of the human genome. Science 291:1304–1351
2. Venter JC (2011) Genome-sequencing anniversary. The human genome at 10: successes and challenges. Science 331:546–547
3. Gutenkunst RN, Waterfall JJ, Casey FP, Brown KS, Myers CR, Sethna JP (2007) Universally sloppy parameter sensitivities in systems biology models. PLoS Comput Biol 3:1871–1878
4. Bakker BM, Michels PA, Opperdoes FR, Westerhoff HV (1997) Glycolysis in bloodstream-form *Trypanosoma brucei* can be understood in terms of the kinetics of the glycolytic enzymes. J Biol Chem 272:3207–3215
5. Edwards JS, Palsson BO (1998) How will bioinformatics influence metabolic engineering? Biotechnol Bioeng 58:162–169
6. Edwards JS, Ibarra RU, Palsson BO (2001) In silico predictions of *Escherichia coli* metabolic capabilities are consistent with experimental data. Nat Biotechnol 19:125–130
7. Barkai N, Leibler S (1997) Robustness in simple biochemical networks. Nature 387:913–917
8. Alon U, Surette MG, Barkai N, Leibler S (1999) Robustness in bacterial chemotaxis. Nature 397:168–171
9. Segel IH (1993) Enzyme kinetics: behavior and analysis of rapid equilibrium and steady state enzyme systems. Wiley, New York
10. Vance W, Arkin A, Ross J (2002) Determination of causal connectivities of species in reaction networks. Proc Natl Acad Sci USA 99:5816–5821
11. Bujara M, Schümperli M, Pellaux R, Heinemann M, Panke S (2011) Optimization of a blueprint for in vitro glycolysis by metabolic real-time analysis. Nat Chem Biol 7:271–277
12. Blagoev B, Ong SE, Kratchmarova I, Mann M (2004) Temporal analysis of phosphotyrosine-dependent signaling networks by quantitative proteomics. Nat Biotechnol 22:1139–1145
13. Helmy M, Gohda J, Inoue J, Tomita M, Tsuchiya M, Selvarajoo K (2009) Predicting novel features of toll-like receptor 3 signaling in macrophages. PLoS One 4:e4661
14. Selvarajoo K, Takada Y, Gohda J, Helmy M, Akira S, Tomita M, Tsuchiya M, Inoue J, Matsuo K (2008) Signaling flux redistribution at toll-like receptor pathway junctions. PLoS One 3:e3430
15. Maamar H, Raj A, Dubnau D (2007) Noise in gene expression determines cell fate in *Bacillus subtilis*. Science 317:526–529
16. Longtin A (1993) Stochastic resonance in neuron models. J Stat Phys 70:309–327

Chapter 3
Basics of the Mammalian Immune System

The immune system of living organisms is a highly complex and sophisticated response machinery that protects the host from a diverse range of invading pathogens. It also helps to neutralize any toxic or allergenic substances that enter the host. Today, the creation of a new scientific and therapeutic field, tumor or cancer immunology [1], to combat malignant cancers through the use of immune cell response demonstrates the crucial importance of the immune system in the survival, adaption, and existence of living organisms.

In vertebrates, the immune system consists broadly of two interconnected components: innate and adaptive [2]. The innate immune system, the first line of the host defense mechanism, consists of specialized cell types such as macrophages, neutrophils, and dendritic cells (Fig. 3.1). These cells carry pattern recognition receptors and cell-surface molecules enabling the detection of microbial intruders and invoke the release of proinflammatory cytokines. The induced cytokines, which are cell-signaling proteins or peptides, enhance the immune response by triggering intracellular cascades in other cell types to collectively fight against the infection. The innate immune response occurs within minutes and lasts for a few days.

The adaptive immune response, on the other hand, produces a stronger effect as well as creating immunological memory, where the signature antigen of each pathogen is stored in specific lymphocytes: B- and T cells (Fig. 3.1). Thus, in contrast to the innate immune cells that produce a more general response, the adaptive immune cells contain antigen-specific receptors, which allows for the generation of tailored responses precisely targeting 'memorized' pathogens. As adaptive immunity occurs over weeks to years, the immunological memory invokes rapid eradication of subsequent infections, which otherwise require longer periods of time, making it crucial for the overall survival of vertebrates. This is the basis for immunization and vaccination in humans.

Although the innate and adaptive components are often discussed independently, they actually work together in sequential order to complete the entire neutralization process of infectious pathogens. However, when the balance with the immune system is compromised, as through genetic mutations, the net effect could lead to
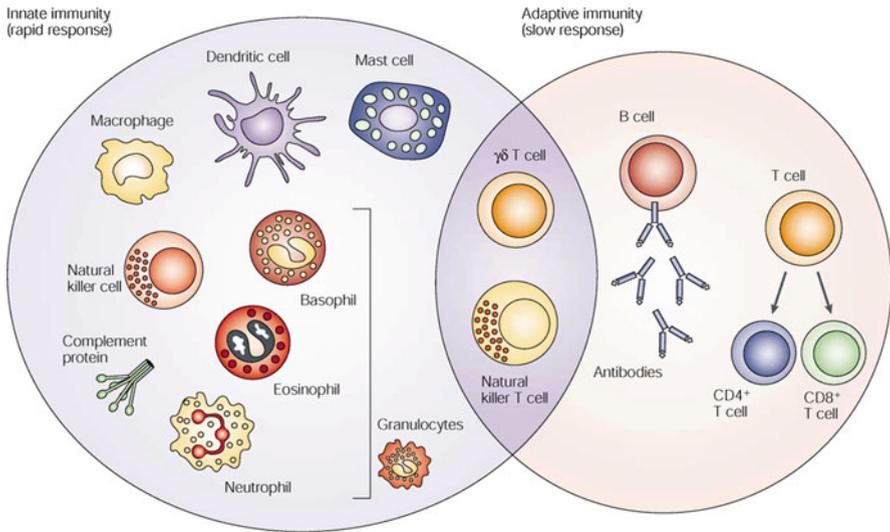
Fig. 3.1 *The cell types and components that represent the innate and adaptive immune systems* (Adapted from Dranoff [3])

immune-related disorders such as rheumatoid arthritis, inflammatory bowel disease, Crohn's disease, diabetes mellitus type 1, and cancer [4]. Thus, the proper functioning of the immune system not only protects the host from pathogenic infection, it also prevents chronic illnesses from occurring.

Types of Innate and Adaptive Immune Cells and Their Roles

The immune system has its origin from the hematopoietic stem cells. The multipotent hematopoietic stem cells differentiate into common myeloid and lymphoid progenitors. The common myeloid progenitors, subsequently, generate megakaryotes, erythrocytes, mast cells, macrophages, dendritic cells, neutrophils, basophils, and eosinophils, whereas the common lymphoid progenitors give rise to small lymphocytes (B- and T cells) and large granular lymphocytes (natural killer or NK cells) (Fig. 3.2).

The innate system consists of complement proteins, mast cells, macrophages, dendritic cells, neutrophils, basophils, eosinophils, and NK cells (Table 3.1). These proteins or cells generally identify foreign agents that enter the host and generate two major functions: (i) the elimination of pathogens or toxic materials through direct contact or engulfing (endocytosis) and neutralizing them (phagocytosis), and (ii) the production of cytokines and antigen (a unique component of the intruder) presentation, which act as mediators to trigger adaptive immunity.
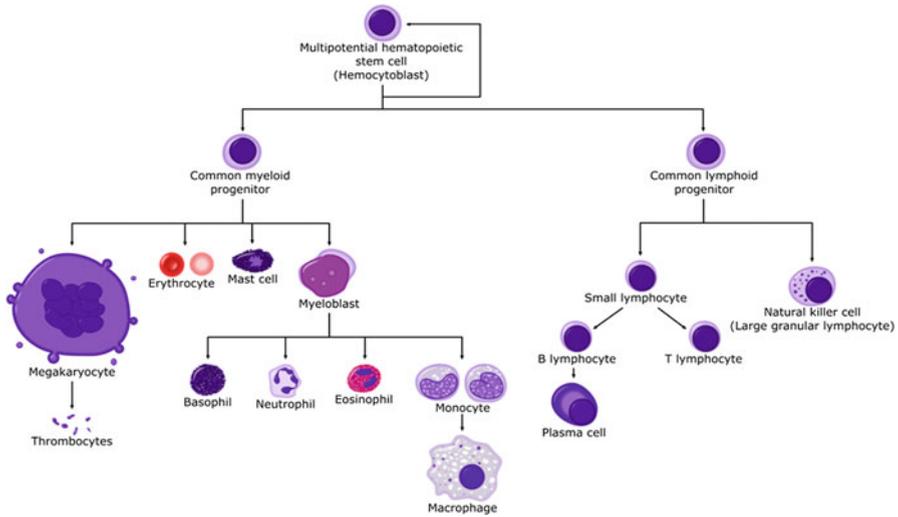
Fig. 3.2 *Cell differentiation lineage of multipotent hematopoietic stem cells into innate and adaptive immune cells* (Adapted from Wikipedia)

The adaptive system comprises mainly B cells and T cells. The B cell expresses antibodies, also known as an immunoglobulin, on its surface. The antibodies recognize antigens presented by the antigen-presenting cells, resulting in the engulfment and digestion of the antibody–antigen complex within the B cell. Subsequently, fragments or peptide antigens are displayed on major histocompatibility complex (MHC) class II surface molecules that attract specific matching T cells. B cells are activated on interaction with T cells, and this leads to their maturation and differentiation into antibody-producing plasma cells.

There are several types of T cells: helper, killer, memory, NK, and γδ (Table 3.1). Among these, the best studied cells are helper and killer T cells. The helper T cells, sometimes referred as CD4+ T cells, by recognizing the antigen fragments bound on MHC class II molecules produce autocrines, which subsequently multiply and mature B cells into plasma cells and memory B cells. The killer T cells, as the name implies, kill virus-infected or damaged cells. These cells are also known as CD8+ T cells and are specific to MHC class I molecules found on almost every cell type in the host.

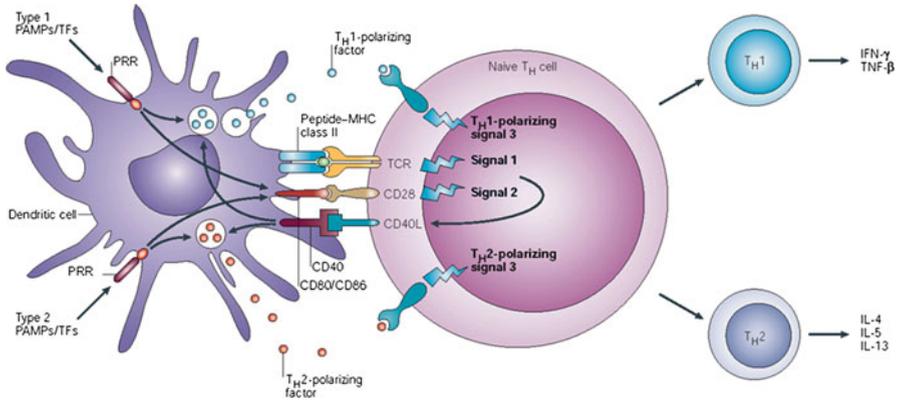## The Link Between Innate and Adaptive Immunity

Innate and adaptive immunity, although these functions have been classified distinctly, are, in fact, well connected and require highly organized orchestration for completing the recognition to elimination process of host infection. The innate immune cells possess microbial sensors that detect invariant molecular patterns,

Table 3.1 Main functions of innate and adaptive immune cells

Cell type	Designation/subtype	Main function
Mast cell	Innate	Releases heparin and other hormonal mediators that play protective and wound-healing roles
Basophil	Innate	Plays similar role to mast cell
Neutrophil	Innate	Rapid responders that migrate toward the site of inflammation and "nonspecifically" destroy the invaders
Eosinophil	Innate	Possesses functions similar to both basophils and neutrophils
Macrophage	Innate	Phagocytosizes necrotic materials, regenerates cell repair, and induces cytokine production for adaptive immunity
Dendritic cell	Innate	Act as antigen-presenting cells for adaptive immunity and also induce cytokine production
Natural killer	Innate	Surveys and fights infected and cancer cells; also produces cytokines for triggering adaptive immunity
B lymphocytes	Adaptive/plasma B cells	Produce antibodies required for destruction through phagocytes such as T cells
	Adaptive/memory B cells	Memory cells for quick response following a second exposure to the same antigen
T lymphocytes	Adaptive/helper (CD4+)	Assist and control other cells for the transition between innate and adaptive response
	Adaptive/killer (CD8+)	Kill pathogen-infected or damaged/dysfunctional cells
	Intermediate/NKT	Share the property of NK and T cells
	Intermediate/γδ	Largely unknown but believed to have a key role in recognition of lipid antigens

also referred to as pathogen-associated molecular patterns (PAMPs), of microorganisms through the pattern-recognition receptors (PRRs) to trigger its response. There are several types of PRRs, such as the secreted, cytosolic, and transmembrane classes. Among these, the Toll-like receptors (TLRs) are the best characterized and studied [5].

The PRRs, upon detecting PAMPs, trigger intracellular molecular signaling cascades that induce the production of costimulatory molecules (such as tumor necrosis factor) and cytokines crucial for the activation of adaptive immune system, mainly through T cells (Fig. 3.3). Usually the PAMPs attached to the PRRs internalize into the cytosol-forming phagosome or endosome, where the pathogenic materials or antigens are processed. Consequently, these are presented back at the cell surface by MHC class I or II. The T-cell receptor (TCR) on the immature T cells connects with the antigens from the innate immune or antigen-presenting cells and matures them to become helper or killer T cells (Fig. 3.3).

Fig. 3.3 *Link between innate immune response and adaptive immunity in a dendritic cell* (Adapted from Kapsenberg [6])

As the vertebrate immune system is broad and complex, this book focuses only on the innate immune response, with main emphasis on the intracellular signal transduction pathways of the TLRs 3 and 4, tumor necrosis factor (TNF), and TNF-related apoptosis-inducing ligand (TRAIL).

Toll-Like Receptors and Their Signaling Networks

The TLR signaling pathways form an integral part of innate immunity. The TLRs are transmembrane proteins that function to recognize conserved PAMPs related to microorganisms, such as lipopolysaccharide (LPS) from gram-negative bacteria and double-stranded RNA (dsRNA) from viruses. Upon their recognition, the TLRs trigger microbial clearance and induce the production of immunoregulatory chemokines, cytokines, and cell-surface and costimulatory molecules [5]. The TLRs also increase effector functions such as phagocytosis and present antigen to T cells. Thus, the activation of TLRs is a first line of the mammalian immune defense system.

There are 13 known members of the TLRs in mammals. TLRs 1, 2, 4, 5, and 6 are located at the cell surface, whereas TLRs 3, 7, 8, 9, 11, and 13 are bound to the intracellular endosomes. The details of TLR 12, found in mice, remain poorly understood. The superfamily of TLRs each carries a specialized sequence to bind to a wide variety of PAMPs. TLR1 recognizes peptidoglycan and (triacyl) lipoproteins by heterodimerization with TLR2 and has specificity for gram-positive bacteria. TLR2 has the ability to form heteromers with TLR1 or TLR6 to attain specificity for
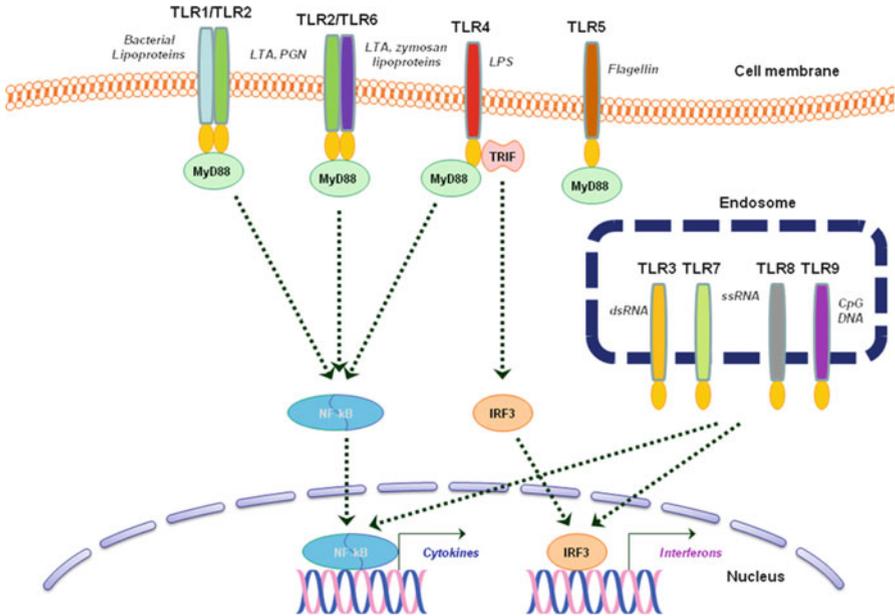
Fig. 3.4 *Main types and location of Toll-like receptors* (*TLRs*). *LTA* lipoteichoic acid, *PGN* peptidoglycan, *LPS* lipopolysaccharide, *dsRNA* double-stranded RNA, *ssRNA* single-stranded RNA

diverse lipopeptides and hence is capable of recognizing a variety of pathogens. TLR3 mostly recognizes virus strands such as dsRNA, viral RNA, and poly (I:C). The best characterized TLR, TLR4, mainly detects lipopolysaccharide (LPS) found in gram-negative bacteria. Figure 3.4 shows the known ligands of the remaining major TLRs.

All TLRs possess the conserved Toll/IL-1 receptor (TIR) region, approximately 160 amino acids long in their cytoplasmic domain, essential for cellular signaling (Fig. 3.5). The TIR mediates the association of adaptor molecules with the myeloid differentiation primary response gene 88 (MyD88), TIR domain-containing adaptor including interferon-β (TRIF), TRIF-related adaptor molecule (TRAM), and TIR domain-containing adaptor protein (TIRAP), all of which contain complement TIR-binding domains.

Upon ligand binding, all TLRs, except TLR3, trigger the MyD88-dependent pathways. TLR3 solely, and TLR4 additionally, activate the MyD88-independent or TRIF/TRAM-dependent pathways (Fig. 3.6). The TIR domain allows the recruitment of MyD88 to the intracellular TLRs, resulting in the binding of IRAK-4 to MyD88 at the receptor, which induces the association of IL-1R-associated kinase 1 (IRAK-1). IRAK-1 becomes phosphorylated and recruits tumor necrosis factor receptor-associated factor 6 (TRAF-6). Phosphorylated IRAK-1 and TRAF-6 dissociate from the receptor and form a complex with transforming growth factor-β-activated kinase (TAK)1, TAK-binding protein (TAB)1, and TAB2; this results in

Fig. 3.5 *Schematic structure of Toll-like receptor (TLR) showing the Toll/IL-1 receptor (TIR) domain. LRR* leucine-rich repeats

Fig. 3.6 *Signaling networks of major TLRs* (Adapted from Romagne [7])

(i) the activation of AP-1 through mitogen-activated protein (MAP) kinases and (ii) the activation of NF-κB (p65/p50) through IκB kinases (IKK α, β, and γ). The activated AP-1 and NF-κB bind to the promoter region of many proinflammatory genes in the nucleus and induce their messenger RNA expression. The MyD88-dependent pathway mainly induces proinflammatory cytokines such as TNF, IL-6, and SOCS3.

The TRIF/TRAM-dependent pathway, on the other hand, recruits TRIF/TRAM at the TIR and activates IKKε and TBK1. This pathway results in the triggering of NF-κB (cRel/p50) and interferon (IFN) regulatory factor 3 or 7 (IRF-3/7) for the induction of type I interferons (IFNs) and chemokines such as IP-10 (encoded by *Cxcl10*) and IFN-induced proteins. Thus, the MyD88- and TRIF/TRAM-dependent pathways complement each other in the production of a wide range of proinflammatory mediators.

There are, however, checkpoints in the TLR signaling that limit the amount and duration of the overall proinflammatory response: this check is performed through negative regulators that are active across various positions along the signaling pathways. Decoy receptors at the membrane surface, such as SIGIRR, or crosstalk with other pathways, such as transforming growth factor (TGF)-β, suppress TLR signaling by competing for ligands or intracellular molecules, respectively [8]. Others include IRAK-M, SOCS1, NOD2, PI3K, TOLLIP, and A20, which principally target the intracellular MyD88-dependent pathway. Caspases are also known to compete for intracellular TLR signaling by channeling the fluxes to the apoptosis pathways [9].

The TLRs also play major roles in numerous chronic diseases [10]. The expression of TLRs has been reported to be elevated in the immune cells of subjects suffering from diabetes mellitus, atherosclerosis, rheumatoid arthritis, etc. In addition, elevated expression of TLRs has also been discovered in many cancer cell types, and mounting evidence indicates TLR-associated infection causes tumorigenic inflammatory responses that lead to cancer development. Thus, suppression of the TLR pathways seems a viable option to control complex proinflammatory diseases. Investigation of the dynamic response of TLRs is important as it will allow a better understanding of the complex signaling mechanism and will eventually lead to strategies that could specifically modulate the signaling network at appropriate locations for the development of novel and effective therapeutic candidates.

The TLR research has gained rapid momentum over the last two decades, primarily because of its significance in controlling the major response of the innate immunity. Experiments at various levels and scales, from the single molecule at a single cell to cell populations, with time-course and high-throughput data acquisition, have been performed to understand these pathways and the regulatory roles of different adaptors and signaling molecules [11–14]. Despite this, the detailed mechanism of signal propagation through both the MyD88-dependent and the TRAM/TRIF-dependent pathway remains poorly understood. Furthermore, as more information and details regarding these pathways are obtained, it becomes increasingly daunting to analyze the data without the aid of appropriate analytical and systemic tools.

The next chapter investigates TLR4 signaling dynamics through a dynamic computational modeling approach utilizing the perturbation-response methodology described in Chap. 2. The subsequent chapters are devoted to the systemic investigation of TLR3 and other innate immune-related networks (TNF and TRAIL signaling).

References

1. Finn OJ (2008) Cancer immunology. N Engl J Med 358:2704–2715
2. Elgert KD (2009) Immunology: understanding the immune system, 2nd edn. Wiley-Blackwell, New York
3. Dranoff G (2004) Cytokines in cancer pathogenesis and cancer therapy. Nat Rev Cancer 4:11–22
4. Rose NR, Mackay IR (eds) (2006) The autoimmune diseases, 4th edn. Elsevier-Academic Press, New York
5. Krishnan J, Selvarajoo K, Tsuchiya M, Lee G, Choi S (2007) Toll-like receptor signal transduction. Exp Mol Med 39:421–438
6. Kapsenberg ML (2003) Dendritic-cell control of pathogen-driven T-cell polarization. Nat Rev Immunol 3:984–993
7. Romagne F (2007) Current and future drugs targeting one class of innate immunity receptors: the Toll-like receptors. Drug Discov Today 12:80–87
8. Liew FY, Xu D, Brint EK, O'Neill LA (2005) Negative regulation of Toll-like receptor-mediated immune responses. Nat Rev Immunol 5:446–458
9. Salaun B, Romero P, Lebecque S (2007) Toll-like receptors' two-edged sword: when immunity meets apoptosis. Eur J Immunol 37:3311–3318
10. O'Neill LA, Bryant CE, Doyle SL (2009) Therapeutic targeting of Toll-like receptors for infectious and inflammatory diseases and cancer. Pharmacol Rev 61:177–197
11. Nilsson R, Bajic VB, Suzuki H, di Bernardo D, Björkegren J, Katayama S, Reid JF, Sweet MJ, Gariboldi M, Carninci P, Hayashizaki Y, Hume DA, Tegner J, Ravasi T (2006) Transcriptional network dynamics in macrophage activation. Genomics 88:133–142
12. Selvarajoo K (2006) Discovering differential activation machinery of the Toll-like receptor 4 signaling pathways in MyD88 knockouts. FEBS Lett 580:1457–1464
13. Hoffmann A, Levchenko A, Scott ML, Baltimore D (2002) The IkappaB-NF-kappaB signaling module: temporal control and selective gene activation. Science 298:1241–1245
14. Chen J, Nag S, Vidi PA, Irudayaraj J (2011) Single molecule in vivo analysis of Toll-like receptor 9 and CpG DNA interaction. PLoS One 6:e17991

Chapter 4
Inferring Novel Features
of the TLR4 Pathways

The TLR4 signaling pathway consists of the MyD88-dependent and TRIF/
TRAM-dependent pathways. Initial experimental studies involving signaling mol-
ecules mediated through the pathways have been predominantly performed in a
nonconstitutive manner. That is, the two pathways have been studied independently
of each other. However, later studies indicated that the two pathways interacted
downstream of TRIF and, therefore, may be dependent on each other in the activa-
tion of proinflammatory transcription factors NF-κB and AP-1. For example, LPS-
induced activation of TLR4 in murine macrophages deficient in MyD88 demonstrated
impaired and delayed kinetics of NF-κB activity (Fig. 4.1a) [1]. This result has been
reproduced on several occasions [2, 3]. However, it was also shown that NF-κB-
dependent cytokines such as tumor necrosis factor (TNF) and interleukin (IL)-1β
were abolished in MyD88-deficient cells (Fig. 4.1b) [1]. If NF-κB is not completely
abolished in MyD88-deficient cells, why are the corresponding cytokines abolished?

Other work has demonstrated the interaction of Toll/IL-1 receptor (TIR) domain-
containing adaptor (TRIF) with TNF-receptor-associated factor 6 (TRAF6) [4],
leading to the question whether TRAF6 binding to TRIF could lead to the activation
of NF-κB in a MyD88-independent manner. However, LPS-stimulated TRAF6-
deficient mice have also shown the induction of NF-κB [2, 5]. Collectively, these
studies indicate a possible link between the MyD88-dependent and TRIF/TRAM-
dependent pathways in the activation of NF-κB, in both MyD88- and TRAF6-
deficient mice. However, the suggestion of signaling crosstalk occurring by the
binding of TRAF6 to TRIF remains controversial [4, 5].

To address the mechanistic properties related to the crosstalk, and to understand
the differential kinetics of signaling molecules in mutant conditions, such as the
delay mechanism for NF-κB activation in MyD88-deficient cells, a systems biology
approach that analyzes the available TLR4 network with experimental dynamics in
multiple conditions (wild-type and mutant data) is required. Here, the perturbation-
response approach is used for the investigation.
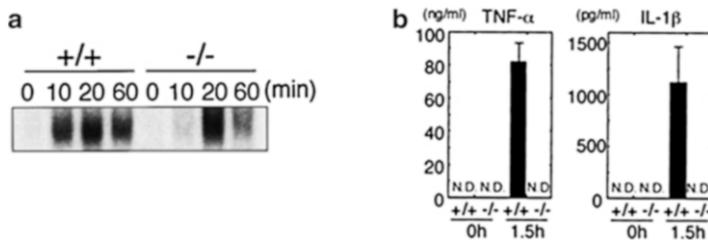
Fig. 4.1 *Experimental profiles of key molecules in wild-type and MyD88-deficient conditions to Toll-like receptor 4 (TLR4) lipopolysaccharide (LPS) stimulation.* NF-κB activation (**a**) and NF-κB-inducible tumor necrosis factor (TNF)-α and in interleukin (IL)-1β expression (**b**) in wild-type (+/+) and MyD88 KO (−/−) murine macrophages (Obtained from Kawai et al. [1])

Computational Response Model of the TLR4 Pathways

When we first developed the original computational model of TLR4 signaling in 2005 [6], the then-known topology of TLR4 signaling was as represented in Fig. 4.2. To interpret the intracellular signaling dynamics using this knowledge, a dynamic model was developed using first-order mass-action equations or the linear response approach (Chap. 2).

The initial model begins with the perturbation of the TLR4 receptor representing the binding of LPS/CD14/MD2; this triggers both the MyD88-dependent and TRIF/TRAM-dependent pathways (Fig. 4.2). For the MyD88-dependent pathway, the signaling reactions are (i) MyD88/MAL associates to the intracellular TIR domain of TLR4 receptor (TIRAP can be lumped with MyD88), (ii) IRAK1 and IRAK4 associate to MyD88 at the receptor, (iii) IRAK-MyD88 complex activates TRAF6, (iv) TRAF6 stimulates the formation of the TAB1/TAB2/TAK1 complex, (v) TAB1/TAB2/TAK1 complex triggers MKK3/6, MKK4/7, and IKK complex (IKKα, IKKβ, and IKKγ), (vi) MKK4/7 activates JNK, (vii) MKK3/6 activates p38, (viii) IKKs phosphorylate IκBα and release NF-κB, (ix) p38 and JNK translocate to the nucleus, (x) NF-κB translocates to the nucleus, (xi) JNK and p38 activate AP-1, and (xii) NF-κB and AP-1 bind to the relevant gene promoters and induce transcription of *Tnf*, *Socs3*, *il6*, etc.

The following constitutes the TRIF/TRAM-dependent pathway: (a) TLR4 stimulates recruitment of TRAM and TRIF to the TIR domain of TLR4 together, (b) TRIF binds with IKKε and TBK1 to activate IFN regulatory factor (IRF)-3, (c) IKKε/TBK1 complex activates cRel of NF-κB, and (d) IRF-3 and NF-κB translocate to the nucleus, inducing the gene transcription of *Cxcl 10*, *ifit 1*, *ifnb1*, etc. Note that a formation (activation) term in the model refers to a binding, phosphorylation, or induction process, whereas a depletion (deactivation) term refers to an unbinding, dephosphorylation, translocation, or decay process.

The computational modeling approach consists of two broad procedures: model creation and model testing (Fig. 4.3). An initial signaling topology is obtained from well-known pathway databases, such as the Kyoto Encyclopedia of Genes and Genomes (KEGG) database [8], or is manually created (step 1). Using the topology, a computational model is developed where each reaction is represented by a
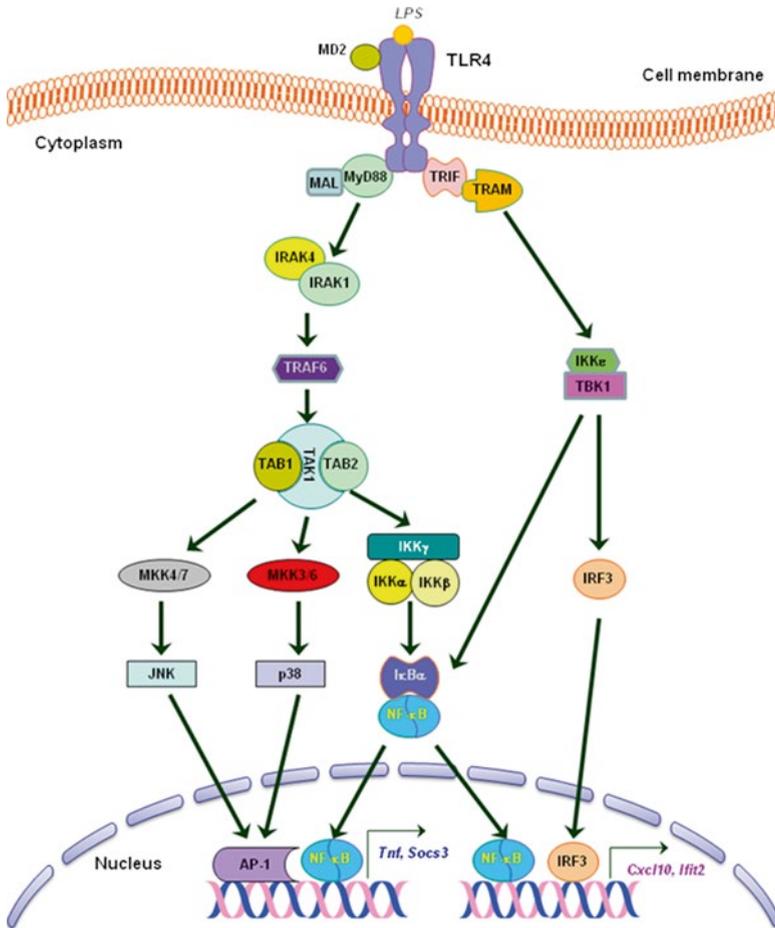
Fig. 4.2 *Schematic of TLR4 pathway* (Redrawn from the KEGG database in 2005)

first-order mass-action response equation with pulse perturbation given to the receptor species (step 2). The parameters of the model (elements of *J* or response coefficients; see Chap. 2) are estimated by fitting the simulation profiles of available downstream molecules such as NF-κB and MAP kinases with corresponding activation profiles of wild-type cells for a specified period, usually up to 1 or 2 h, representing the primary signaling process (step 3). Note that during this period, secondary effects caused by autocrine signaling and feedback mechanisms are usually minimal. (Note that we ignore the feedback loop of NF-κB for simplicity as it occurs on average after 100 min) Provided the network topology is reasonably small, the model parameters can be chosen manually. Otherwise, semiautomatic selection methods, such as the genetic algorithm [9], can be utilized (Box 4.1). However, caution is required when using a fully automated system (with no human intervention) as it may lead to local or overfitting problems.
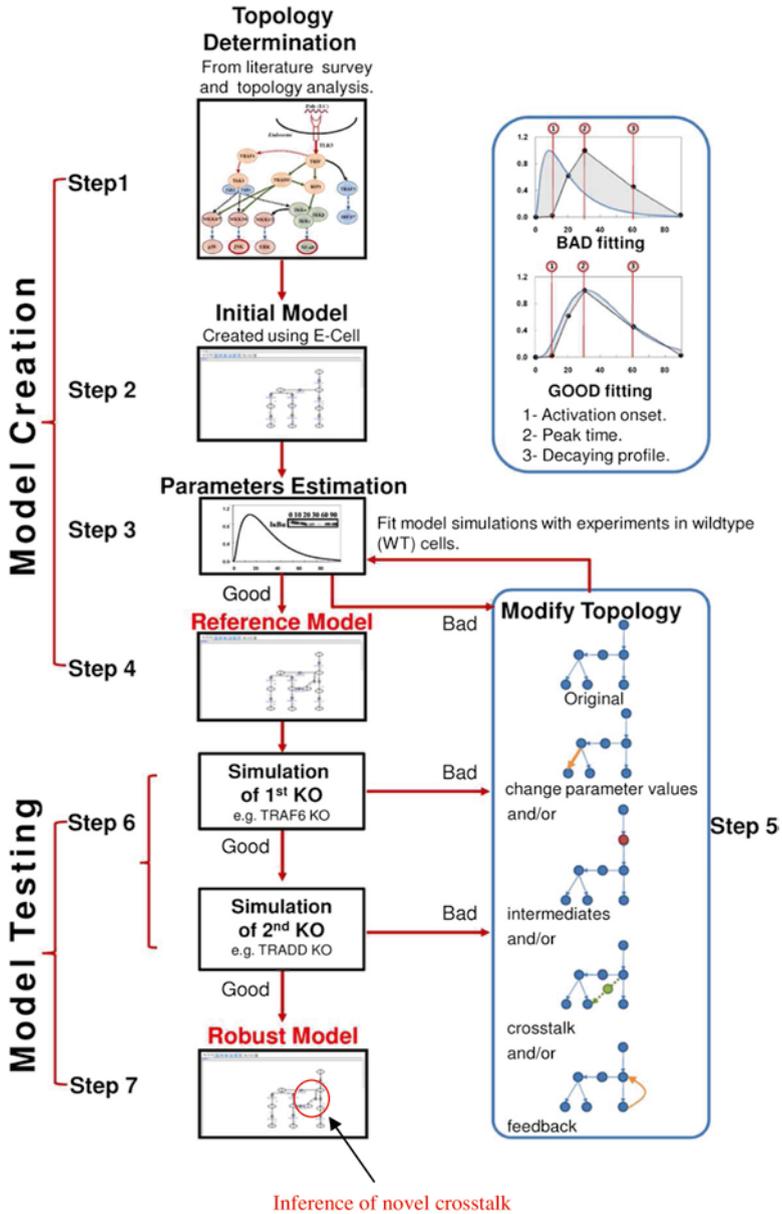
Fig. 4.3 *Computational modeling approach for TLR signaling* (Adapted from Helmy et al. [7])

Box 4.1 Parameter Fitting and Fitness of Simulations

The parameter fitting of the reactions of a given topology is obtained by mini-mizing the error between experimental and simulation profiles of all investi-gated molecules. A genetic algorithm can be used with a fitness function f (example) given by

$$f = \sum_i^n \sum_k^m \varepsilon_{i,k} = \frac{\int_0^{t_{max}} \left[SIM_{i,k} - EXP_{i,k} \right] dt}{\int_0^{t_{max}} EXP_{i,k} dt}$$

where $\varepsilon_{i,k}$ is the error between the experimental and simulation curves of the ith molecule in the kth condition represented by the normalized area between the experimental and simulation curves for a period t to t_{max}. The algorithm evolves the parameter sets from one generation to the next by the operations of selection, crossover, and mutations [9]. The model is considered acceptable when the tolerance is set, for example, as $\max(\varepsilon_{i,k}) \leq Tol$. To avoid local min-ima, the algorithm is performed multiple times and in multiple experimental (e.g., KO) conditions.

Presently, most of the experimental datasets available for cell signaling dynamics are semiquantitative by nature (e.g., Western blots, ELISA; Fig. 4.1a). To analyze a dynamic model simulation with such data, the experimental data can be quantified using imaging tools such as ImageJ [10]. This step allows the model simulations to be compared with relative semiquantitative experimental profiles, and the fitting process minimizes the gap between simulated and experimental profiles by varying each reaction parameter value randomly (Fig. 4.3, top right insert).

When the model is able to successfully fit the wild-type profiles of all tested molecules, the model is referred to as the reference model (step 4). Otherwise, the model topology or parameter values (response coefficients) are further adjusted until the model is able to simulate the experimental profiles reasonably well (step 5). There can be several Js that could fit wild-type activation profiles of reaction spe-cies, thereby reducing the confidence of the model. To overcome the issue, so as to reduce the parameter space for J, temporal experimental profiles of other mutant conditions where data are available, such as MyD88 knockout (KO) and/or TRAF6 KO, are utilized.

Each in silico KO is performed by setting the response coefficient(s) involving the KO molecule null and comparing the simulations with the relevant KO experi-mental data. If the KO simulations do not go well with experimental profiles, the response coefficients are retuned until the model simulations are able to fit the acti-vation profiles of both wild-type and KO conditions (step 6). Alternatively, if tuning all parameters does not improve the model simulations, the network topology of the model is modified, according to the *response rules* derived from the law of mass flow (signaling flux) conservation (Box 4.2). For example, adding novel signaling

intermediates to obtain delay in the activation or crosstalk mechanism to provide an alternative source of activation in a KO condition (Box 4.2; and see later section). The procedure of modifying parameter values and topology is repeated until reasonable predictions for all conditions are obtained. Consequently, the comparison of our initial model topology with the final 'robust' model will result in the inference of novel network features (step 7).

Box 4.2 Response Rules

Here, 10 response rules, from the law of signaling flux conservation and first-order response to pulse perturbation are developed, to modify the initial signaling topology for the inference of novel network features (A–C). Analyzing time to activation: *Rule 1*, *Time Delay*: By comparing the time to reach peak activation, any time delay in target signaling molecule's activation represents 'missing' cellular features such as directed transport machinery, protein complex formation, and novel molecular interactions. *Rule 2*, *Rapid Flux*: When the activation of a downstream molecule is noticeably quicker than the experimental activation, a novel rapid bypass pathway is inferred. Analyzing peak activation levels: *Rule 3*, *Missing Flux*: When the removal of a molecule along a pathway does not completely abolish its downstream intermediates, the presence of a novel bypass is indicated. *Rule 4*, *Signaling Flux Redistribution* (*SFR*): At pathway junctions, the removal of a molecule enhances the entire alternative pathways because signaling flux is rechanneled to available routes by the law of mass conservation (see Chap. 5 for details). *Rule 5*, *Lack of SFR*: At pathway junctions, the removal of a molecule does not enhance the alternative pathway, suggesting novel (i) intermediate(s) between the removed molecule and the pathway junction or (ii) a pathway link between the removed molecule and the alternative pathway is/are present. *Rule 6*, *Dominant and Recessive Flux*: Quantifies each pathway branch by comparing activation levels between wild-type and mutant data. Analyzing activation patterns: *Rule 7*, *Reversible Flux*: When a response profile shows limiting decay that cannot be modeled by first-order decay, the presence of a reversible step is expected to produce limiting decay. *Rule 8*, *Superposing Flux*: When a response profile show multiple peaks, the superposition principle indicates the presence of (i) a novel bypass pathway from the same source or (ii) an alternative pathway with delayed response. *Rule 9*, *Continuous Flux*: When a response profile shows a continuous increase of activation not following pulse perturbation response, this indicates additional continuous flux from feedback mechanisms such as posttranslational effect or secondary signaling. *Rule 10*, *Oscillations*: When oscillatory response is observed, (i) a continuous feedback loop is suggested for regular dynamics and (ii) nonlinear effects such as chaotic biochemical dynamics are inferred for irregular dynamics.

(continued)
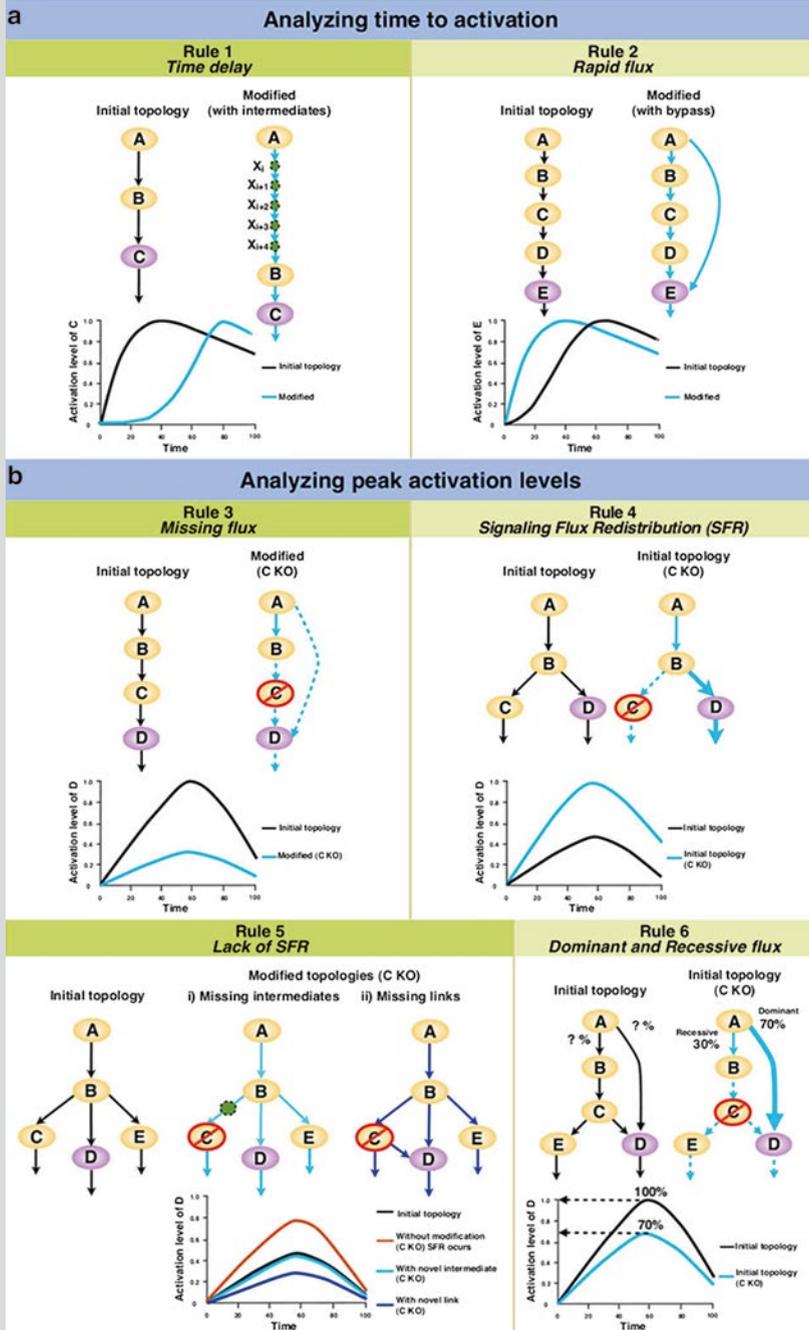
Box 4.2 (continued)

Box 4.2 (continued)
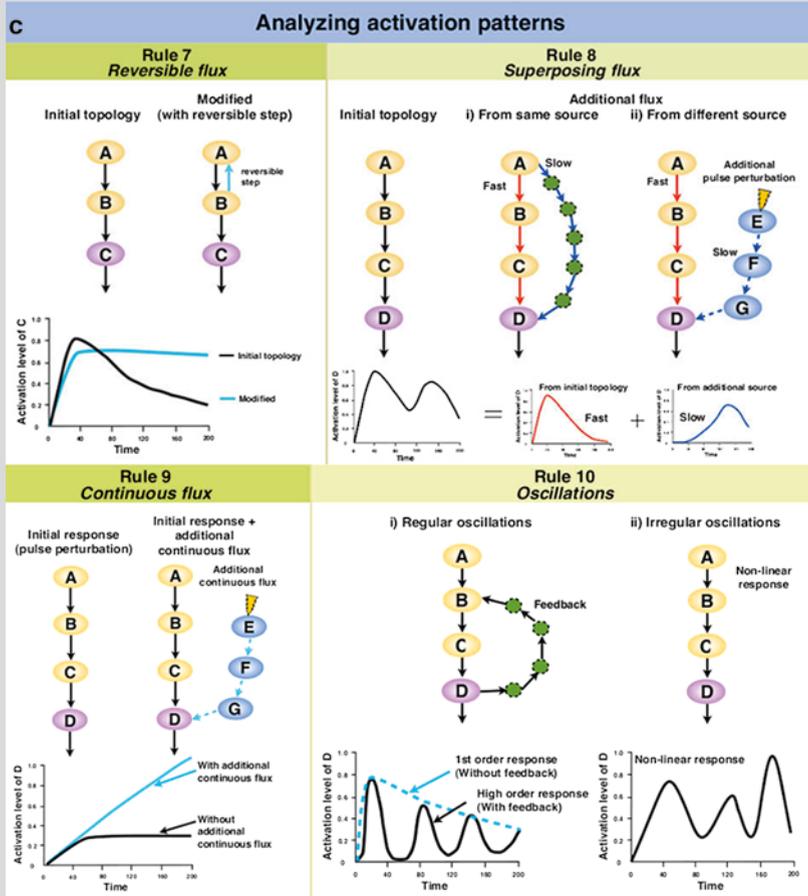
Simulations of NF-κB and MAP Kinases Activity in TLR4 Signaling

The initial conditions for the TLR4 computational model are such that apart from the first signaling steps, from TLR4 to MyD88/MAL and TRIF/TRAM representing the LPS perturbed condition, all other signaling processes begin with null activation (at $t=0$). Note that the model describes the response waves generated by the perturbation and, hence, the simulations will show relative activation levels rather than absolute concentration levels of all the downstream signaling molecules (see Chap. 2).
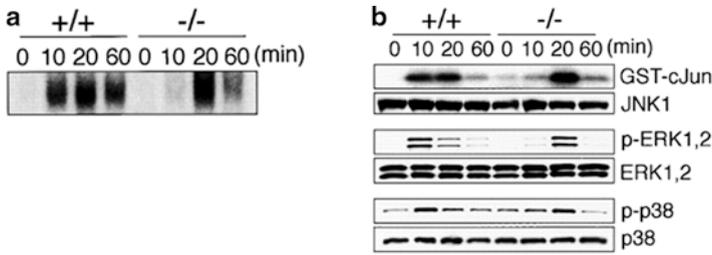
Fig. 4.4 *Experimental profiles of NF-κB and MAP kinases in wild-type and MyD88-deficient condition to TLR4 stimulation*: NF-κB activation (**a**) and MAP kinases (cJun or AP-1, ERK, and p38) activation (**b**) in wild-type (+/+) and MyD88 KO (−/−) murine macrophages. Note that Western blots do not show the maximun peak accurately as the intensity saturates at undetermined concentration (From Kawai et al. [1])

As the TLR field is relatively new, the activation dynamics for most signaling molecules are largely unknown or unmeasured. In fact, data have been measured mainly for NF-κB and MAP kinases activity in a semiquantitative manner (Fig. 4.4).

The initial reference TLR4 model A (Fig. 4.3, steps 1–4) was developed using the pathway available from the KEGG database (Fig. 4.2). To increase the confidence of the model's overall predictability, it is essential to test the simulations for NF-κB and MAP kinase activity in other conditions, such as in genetic knockout (KO) conditions. We tested the TLR4 model in total of six other experimental conditions, namely, MyD88 KO, TRIF KO, TRAM KO, TRAF6 KO, RIP1KO, and TAK1 KO, where data are available for comparison.

Simulating Wild-Type and MyD88 KO Conditions

The initial wild-type simulations were able to fit the experimental semiquantitative profiles of relative NF-κB, AP-1 (cJun) activity reasonably well: zero activity at 0 min, peak activity around 10–20 min, and decaying activity at 60 min (Fig. 4.5, blue solid lines; and Fig. 4.4).

Next, the model A is tested in MyD88 KO. For generating the in silico MyD88 KO condition, the parameter(s) of reaction(s) involving MyD88 in the model is set to null. In contrast to experiments, the in silico MyD88 KO simulations (i) do not show noticeable delay in NF-κB activation and (ii) do show complete abolition of MAP kinase activity (Fig. 4.5, pink dotted line; and Fig. 4.4). In the model, when the activity of the MyD88-dependent pathway is suppressed (i.e., in silico MyD88 KO), there is no alternative MAP kinase activation and the NF-κB activation is purely the result of the TRIF/TRAM-dependent pathway, through the IKKε/TBK1 route. Hence, we observe impaired NF-κB and abolished MAP kinase activity.
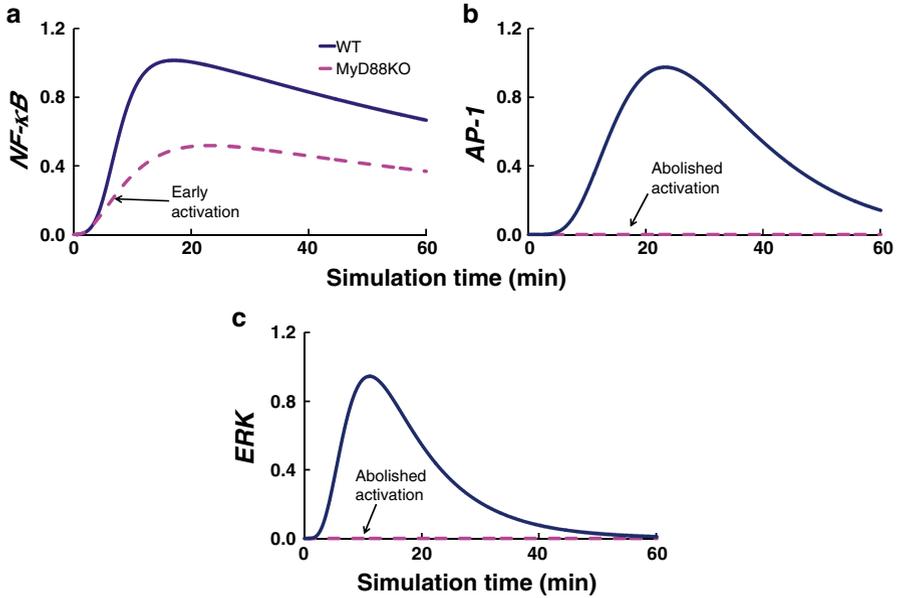
**Fig. 4.5** *Simulation* (*model A*) *of NF-κB and MAP kinases profiles*. NF-κB (**a**), AP-1 (**b**), and ERK activity (**c**) (in arbitrary units) is normalized to wild-type peak values: wild-type (*blue solid lines*) and MyD88 KO (*pink dashed lines*). p38 and ERK possess similar simulation profiles. Note that ERK pathway was added to the original model A of Selvarajoo [6] (see Fig. 4.6a)

Determination of Time Delay Process and Crosstalk Mechanisms

For NF-κB, it is possible to obtain a certain degree of in silico delayed activation by lowering the parameter values along the TRIF/TRAM-dependent pathway. However, this step significantly affects the relative peak levels and the rate (shape) of depletion waves, resulting in still poor simulation profiles [6]. Changing the first-order response equations to other types of expressions, for example, Michaelis–Menten kinetics, higher-order kinetics at TRIF/TRAM or IKKε/TBK1, did not produce effective delay (data not shown). This result may not be surprising given the fact that there are already several studies that suggest biological networks are not sensitive to reaction kinetics, but rather are sensitive to reaction topology [11–14]. As noted earlier, because the TLR field is relatively new, there are possibilities for novel features missing from the original topology (Fig. 4.2). Therefore, the TLR4 network in the model is allowed to be modified for the investigation of novel features that could result in improved model simulations (step 5, Fig. 4.3).

One possible way to provide time delay and still maintain the peak levels is to add novel intermediates between the TLR4 and IKKε/TBK1 via TRIF/TRAM
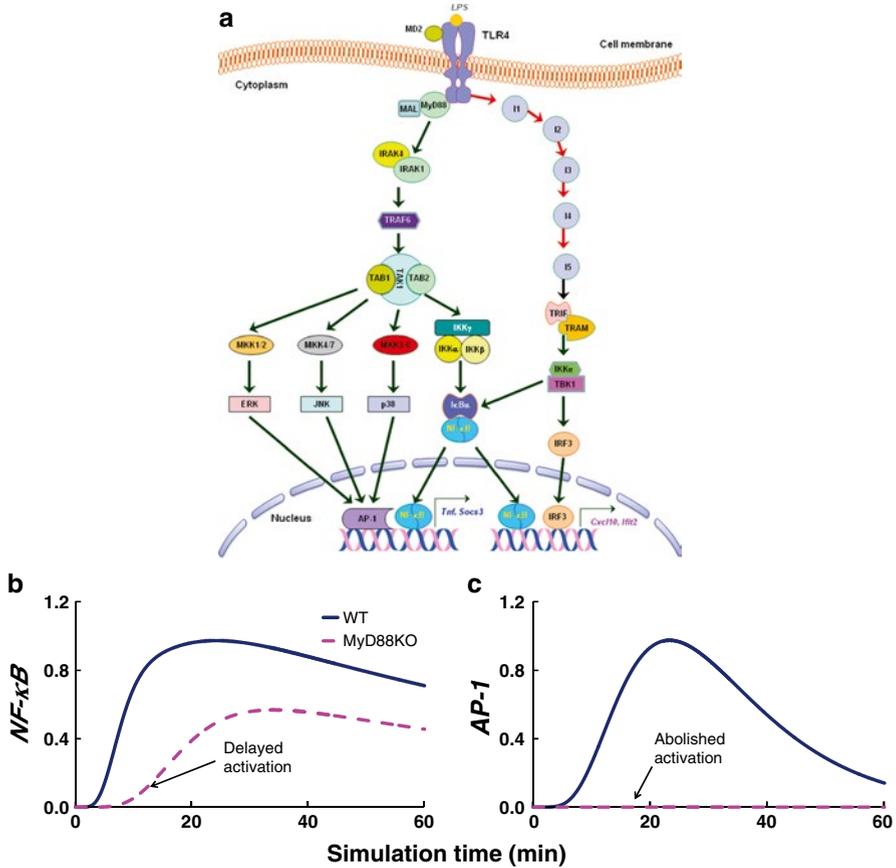
Fig. 4.6 *Updated TLR4 signaling*. (**a**) Modified TLR4 signaling topology including five novel intermediates along TRIF/TRAM pathways. Model B simulation profiles for NF-κB (**b**) and AP-1 (**c**) activation in wild-type and MyD88 KO

activation (*response rule 1*; Box 4.2). Using this rule, several intermediates and reaction kinetics are tested. Consequently, the incorporation of about five theoretical intermediates leads to the desired delayed activation profile of NF-κB (Fig. 4.6a, b; model B). This result suggests that in the TRIF/TRAM-dependent pathway there likely exist 'unaccounted' biological intermediates representing unknown proteins, protein complexes, or molecular processes such as sequestration or transport mechanisms that delay the activation of NF-κB (see Chap. 2, "The origins for linear response") [6].

Although the model is unable to accurately pinpoint the exact number or roles of the novel intermediates upstream of TRIF, nevertheless and remarkably, this overt prediction has been substantiated by recent experimental works: (i) the sequential activation CD14, ITAM-mediated process of tyrosine kinase Syk and its downstream effector PLCγ2 required for the endocytosis of TLR4 before TRIF/TRAM
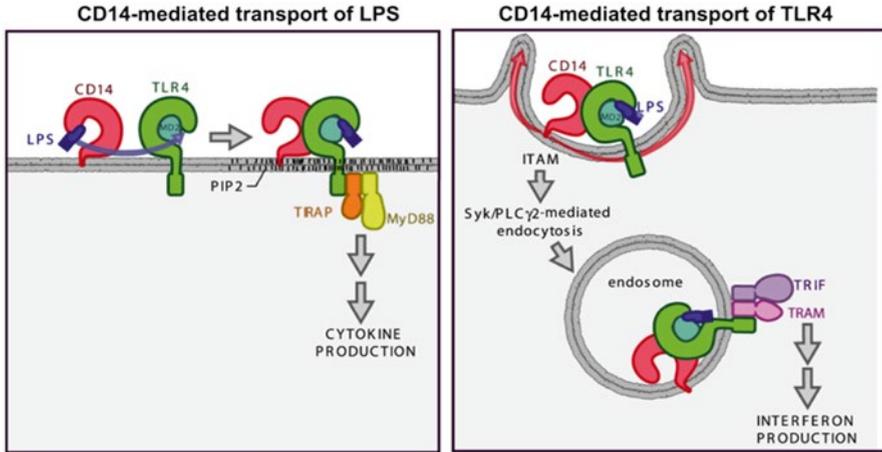
Fig. 4.7 *Recent characterization of upstream intermediates that delay NF-κB and MAP kinase activation in TRIF/TRAM-dependent manner* (From Zanoni et al. [15])

activation (Fig. 4.7) [15, 16], and (ii) the phosphorylation of TRAM by PKCε required for IRF-3 activation and RANTES expression [17]. Note that these studies appeared later than the original TLR4 model predictions [6].

Next, focusing on MAP kinases, the in silico MyD88 KO still shows abolished activation in the updated model B (Fig. 4.6c). This finding, obviously, suggests that an alternative pathway, independent of MyD88, is present and is illustrated by *response rule* 3 (*missing flux*; Box 4.2). Therefore, it is likely that a crosstalk exists between the TRIF/TRAM-dependent pathway and the MyD88-dependent pathway. Alternatively, there could be a novel pathway independent of both MyD88 and TRIF/TRAM molecules.

Several studies have provided evidence for the interaction of MyD88-dependent and TRIF/TRAM-dependent pathways. However, there have also been controversies regarding the issue. As mentioned earlier, Sato et al. [4] have demonstrated the interaction of TRIF with TRAF6, leading to the question whether TRAF6 binding to TRIF could lead to the activation of MAP kinase in a TRIF/TRAM-dependent manner. However, other studies using TRAF6-deficient mice in LPS-induced activation of TLR4 have shown, although impaired, the induction of NF-κB and MAP kinases [2, 5].

To test whether the interaction between TRAF6 and TRIF will improve MAP kinase simulations in MyD88 KO condition, an in silico signaling reaction between TRIF and TRAF6 for model B is added. Note that in model B, the precise location of the five novel intermediates cannot be determined by the perturbation-response model, unless detailed measurement of each molecule is available. Thus, the position of the TRIF/TRAM complex can be adjusted. However, it is likely that the TRIF/TRAM complex is downstream of the novel intermediates (Fig. 4.7). Moreover, it is known that TRAM acts upstream of TRIF [7, 17], and hence in the model, the lumped TRIF/TRAM species and the upstream novel I5 were renamed to TRIF and TRAM, respectively (Fig. 4.8a, model C).
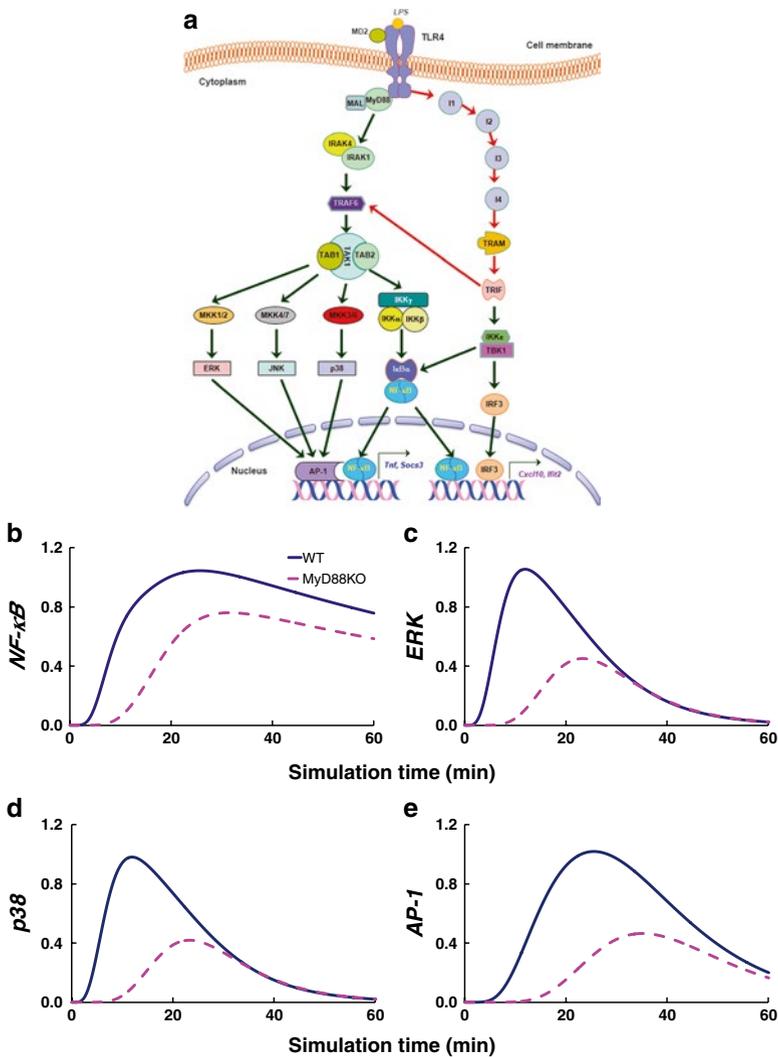
Fig. 4.8 *Model C simulations*. (**a**) Revised TLR4 signaling with TRIF-TRAF6 crosstalk. NF-κB (**b**), ERK (**c**), p38 (**d**), and AP-1 (**e**) activation in wild-type (*blue solid lines*) and MyD88 KO (*pink dashed lines*)

The simulations of NF-κB and MAP kinase activity for model C recapitulate the experimental dynamics in both wild-type and MyD88 KO (Fig. 4.8b, c). Thus, model C also supports (i) novel intermediates (such as Syk, and PLCγ2) between TLR4 and TRIF/TRAM and (ii) crosstalk between TRIF/TRAM and TRAF6. Nevertheless, will this modified model also be able to successfully simulate other KO conditions?
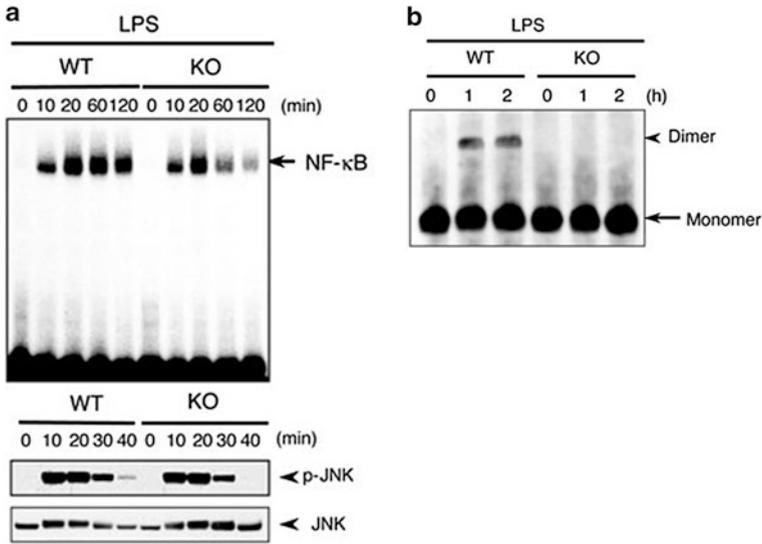
Fig. 4.9 *Experimental NF-κB, IRF-3 and JNK activity in wild-type and TRAM-deficient cells*. Murine macrophages were stimulated with LPS for the indicated periods. (**a**) *Top panel*: Nuclear extracts were prepared, and NF-κB DNA-binding activity was determined by electrophoretic mobility shift assay (EMSA) using an NF-κB-specific probe. *Bottom panel*: JNK activation by Western blotting using anti-phospho-JNK-specific antibody. (**b**) Monomeric (*arrow*) and dimeric (*arrowhead*) forms of IRF-3 from Western blot (From McGettrick et al. [18])

Simulating TRIF KO and TRAM KO Conditions

Next, model C is tested in TRIF KO and TRAM KO conditions. Experimentally, both TRIF and TRAM KOs completely abolish transcription factor IRF-3 activation; however, both NF-κB and MAP kinase JNK activity showed only slight changes compared to the wild-type [3, 18]. Here, only the TRAM KO data source is displayed for the experimental profiles (Fig. 4.9).

By selectively setting the parameter values of TRIF and TRAM to null for their respective in silico KOs, model C was tested with relevant experimental data (Fig. 4.9). Notably, the simulations for NF-κB, JNK, and IRF3 all qualitatively agree with experimental outcome: TRIF and TRAM KOs show (i) almost unchanged NF-κB and JNK activity compared with the wild-type, and (ii) complete abolishment of IRF3 activity (Fig. 4.10). Note that the IRF3 simulation in MyD88 KO shows enhancement compared with wild-type activity. This enhancement occurs as a consequence of *Signaling Flux Redistribution* (*response rule* 4, *SFR*; Box 4.2) and is discussed in more detail in Chap. 5.
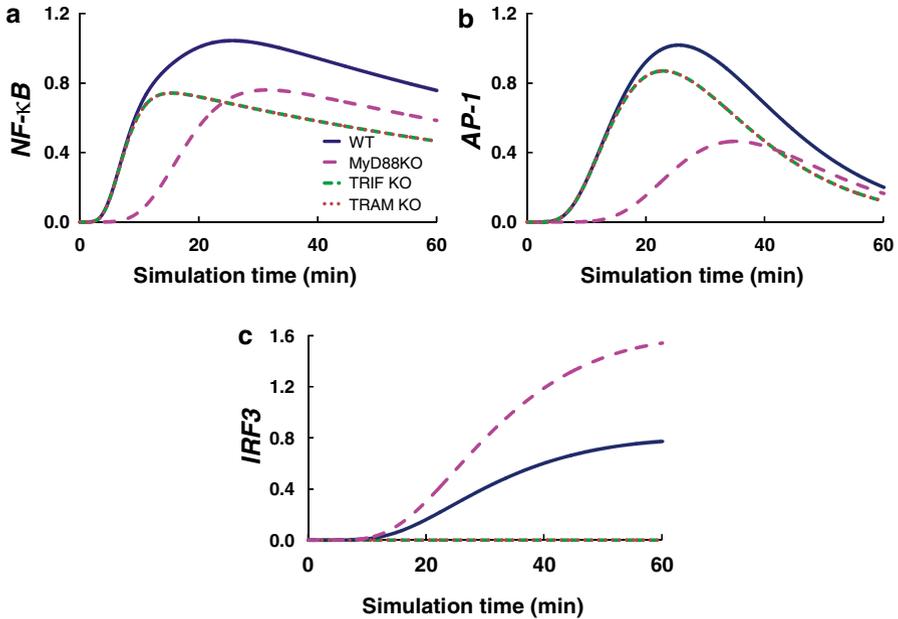
Fig. 4.10 *Model C simulations*: NF-κB (**a**), JNK (**b**), and IRF3 (**c**) activation in wild-type (*blue solid lines*), MyD88 KO (*pink dashed lines*), TRIF KO (*green short-dashed lines*), and TRAM KO (*brown dotted lines*). TRIF and TRAM KOs show identical downstream response

Simulating TRAF 6 KO, TAK1 KO, and RIP1 KO Conditions

TRAF6-deficient mice showed delayed and significantly impaired activation of NF-κB and MAP kinases [5]. From the updated topology (model C), it is conceivable that the removal of TRAF6 will abolish MAP kinase activity. This information alone suggests that, in addition to TRIF to TRAF6 crosstalk, there exist(s) other interaction(s) between the MyD88-dependent and TRIF/TRAM-dependent pathway downstream of TRAF6 for activating MAP kinases (missing flux; *response rule 3*, Box 4.2). This result brings the possibility of a crosstalk anywhere between TRIF and the TAK1/TAB complex or TRIF and MKK3/6 and MKK4/7.

TAK1 has been shown to play a vital role in multiple signaling pathways. A recent TAK1 KO study has revealed pronounced impairment of NF-κB and JNK activity in LPS stimulation [19]. However, from the topology analysis alone, adding crosstalk from the TRIF/TRAM-dependent pathway to TAK1/TAB complex bypassing TRAF6 will completely abolish MAP kinase activation in TAK1 KO. Thus, crosstalk between TRIF and the MyD88-dependent pathway should occur downstream of the TAK1/TAB complex.

Notably, there are reports that RIP1 mediates TRIF-dependent activation of NF-κB and phosphorylates ASK1-interacting protein (AIP)1 for MAP kinase activation [20, 21]. These features were incorporated into a revised model D (Fig. 4.11a).
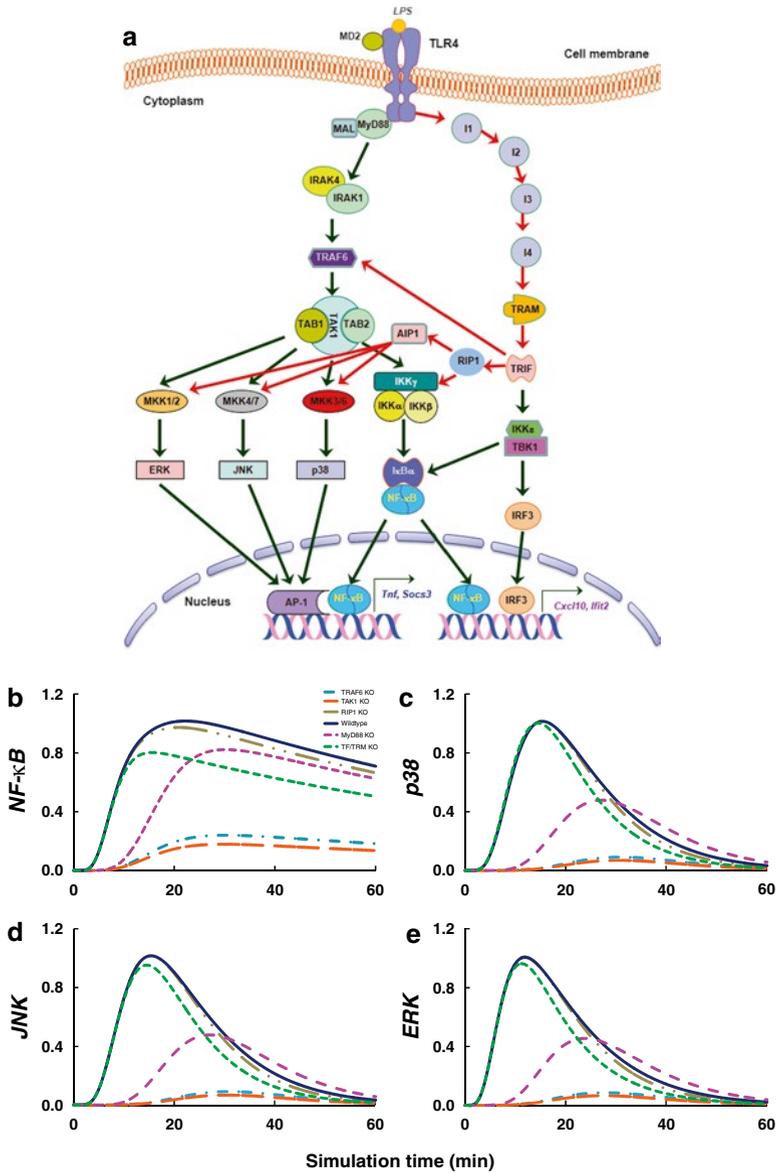
Fig. 4.11 *Finalized TLR4 topology and simulations* (*model D*). (**a**) Updated schematic of TLR pathways. NF-kB (**b**), p38 (**c**), JNK (**d**), and ERK (**e**) simulations in wild-type (*dark blue lines*), TRAF6 KO (*light blue lines*), TAK1 KO (*orange lines*), RIP1 KO (*gold lines*), MyD88 KO (*pink lines*), and TRIF/TRAM KO (*green lines*). Note that TRIF and TRAM KOs simulations are combined into a single *green dotted dashed line* (TF/TRM) because they possess identical profiles. The complete model D reactions and parameter values can be found in Chap. 5 (Table 5.1)

The in silico TRAF6 KO, TAK1 KO, and RIP1 KO simulations are compared with experimental findings. The simulations of NF-κB and MAP kinases in all three conditions are consistent with the relevant experimental data (Fig. 4.11b–e) [5, 19–21]. Next, the final revised model D is tested for NF-κB and MAP kinases dynamics once again in MyD88 KO, TRIF KO, and TRAM KO. As observed from Fig. 4.11b–e, overall, model D is able to recapitulate the experimental data for a total of seven experimental conditions.

In summary, in this chapter, a computational model of TLR4 signaling was developed using the perturbation-response approach and the law of signaling flux conservation (Chap. 2). Starting from an initial known topology, the computational model is analyzed across the wild-type and six mutant (MyD88 KO, TRIF KO, TRAM KO, TRAF6 KO, RIP1KO, and TAK1 KO) conditions. For the computational model to match temporal experimental measurement of key signaling molecules (NF-κB, p38, JNK, and ERK), the response rules (Box 4.2) were used to carefully modify the novel missing features of the original TLR4 topology. In particular, (i) several intermediates along the TRIF/TRAM pathways and (ii) a crosstalk between TRIF and MAP kinases are required for the final model to simulate multiple experimental conditions. From the simulations of the TLR4 pathways, it is evident that the topology or network structure is more crucial than parameter values for robustness of the model to predict multiple experimental conditions.

References

1. Kawai T, Adachi O, Ogawa T, Takeda K, Akira S (1999) Unresponsiveness of MyD88-deficient mice to endotoxin. Immunity 11:115–122
2. Kawai T, Takeuchi O, Fujita T, Inoue J, Mühlradt PF, Sato S, Hoshino K, Akira S (2001) Lipopolysaccharide stimulates the MyD88-independent pathway and results in activation of IFN-regulatory factor 3 and the expression of a subset of lipopolysaccharide-inducible genes. J Immunol 167:5887–5894
3. Yamamoto M, Sato S, Hemmi H, Hoshino K, Kaisho T, Sanjo H, Takeuchi O, Sugiyama M, Okabe M, Takeda K, Akira S (2003) Role of adaptor TRIF in the MyD88-independent Toll-like receptor signaling pathway. Science 301:640–643
4. Sato S, Sugiyama M, Yamamoto M, Watanabe Y, Kawai T, Takeda K, Akira S (2003) Toll/IL-1 receptor domain-containing adaptor inducing IFN-β (TRIF) associates with TNF receptor-associated factor 6 and TANK-binding kinase 1, and activates two distinct transcription factors, NF-κB and IFN-regulatory factor-3, in the Toll-like receptor signaling. J Immunol 171:4304–4310
5. Gohda J, Matsumura T, Inoue J (2004) Cutting edge: TNFR-associated factor (TRAF) 6 is essential for MyD88-dependent pathway but not Toll/IL-1 receptor domain-containing adaptor-inducing IFN-β (TRIF)-dependent pathway in TLR signaling. J Immunol 173: 2913–2917
6. Selvarajoo K (2006) Discovering differential activation machinery of the Toll-like receptor 4 signaling pathways in MyD88 knockouts. FEBS Lett 580:1457–1464
7. Helmy M, Gohda J, Inoue J, Tomita M, Tsuchiya M, Selvarajoo K (2009) Predicting novel features of Toll-like receptor 3 signaling in macrophages. PLoS One 4:e4661
8. Kanehisa M (2002) The KEGG database. Novartis Found Symp 247:91–101
9. Carroll DA (1996) Chemical laser modelling with genetic algorithms. AIAA 34:338–346

10. Collins TJ (2007) ImageJ for microscopy. Biotechniques 43:25–30
11. Barkai N, Leibler S (1997) Robustness in simple biochemical networks. Nature 387:913–917
12. Alon U, Surette MG, Barkai N, Leibler S (1999) Robustness in bacterial chemotaxis. Nature 397:168–171
13. Bailey JE (2001) Complex biology with no parameters. Nat Biotechnol 19:503–504
14. Hartwell LH, Hopfield JJ, Leibler S, Murray AW (1999) From molecular to modular cell biology. Nature 402:C47–C52
15. Zanoni I, Ostuni R, Marek LR, Barresi S, Barbalat R, Barton GM, Granucci F, Kagan JC (2011) CD14 controls the LPS-induced endocytosis of Toll-like receptor 4. Cell 147:868–880
16. Kagan JC, Su T, Horng T, Chow A, Akira S, Medzhitov R (2008) TRAM couples endocytosis of Toll-like receptor 4 to the induction of interferon-beta. Nat Immunol 9:361–368
17. McGettrick AF, Brint EK, Palsson-McDermott EM, Rowe DC, Golenbock DT, Gay NJ, Fitzgerald KA, O'Neill LA (2006) TRIF-related adapter molecule is phosphorylated by PKC epsilon during Toll-like receptor 4 signaling. Proc Natl Acad Sci USA 103:9196–9201
18. Yamamoto M, Sato S, Hemmi H, Uematsu S, Hoshino K, Kaisho T, Takeuchi O, Takeda K, Akira S (2003) TRAM is specifically involved in the Toll-like receptor 4-mediated MyD88-independent signaling pathway. Nat Immunol 4:1144–1150
19. Eftychi C, Karagianni N, Alexiou M, Apostolaki M, Kollias G (2012) Myeloid TAK1 acts as a negative regulator of the LPS response and mediates resistance to endotoxemia. PLoS One 7:e3155
20. Cusson-Hermance N, Khurana S, Lee TH, Fitzgerald KA, Kelliher MA (2005) Rip1 mediates the Trif-dependent toll-like receptor 3- and 4-induced NF-{kappa}B activation but does not contribute to interferon regulatory factor 3 activation. J Biol Chem 280:36560–36566
21. Zhang H, Zhang H, Lin Y, Li J, Pober JS, Min W (2007) RIP1-mediated AIP1 phosphorylation at a 14-3-3-binding site is critical for tumor necrosis factor-induced ASK1-JNK/p38 activation. J Biol Chem 282:14788–14796

Chapter 5
Signaling Flux Redistribution

In the previous chapter, we developed a computational model of the TLR4 pathways and used response rules, derived from the law of mass flow (signaling flux) conservation, to reveal novel features such as missing intermediates and crosstalk mechanisms. This approach was achieved by comparing model simulations with wild-type and multiple mutant conditions. The investigations involved were solely based on protein activation dynamics. Here, we extend the prediction capacity to include downstream dynamic gene expression profiles. In particular, we are interested understanding the possible mechanisms for gain- or loss-of-function mutations in regulating gene expression. In other words, is it possible to understand why certain genes are regulated in genetic mutants not known to affect those genes? For example, will the regulation of MyD88 affect TRAM-dependent genes?

Simulating TLR4-Induced Gene Transcription

The TLR4 model was extended to simulate four key proinflammatory genes, namely, the so-called MyD88-dependent *Tnf* and *Socs3*, and the TRAM-dependent *Cxcl10* and *Ifit2*. We measured the time-course mRNA profiles of these genes in wild-type macrophages following lipopolysaccharide (LPS) stimulation (Fig. 5.1a, blue).

For the computational model, to simulate gene transcription, several intermediary reactions between activation of transcription factors and targeted mRNA transcriptions are included (*response rule 1*; Box 4.2), to represent delay mechanisms potentially caused by chromatin remodeling and initiation complex formation. The parameter values of the additional first-order response equations of each gene are fitted to its respective experimental time-course mRNA profiles (Fig. 5.1b, blue). As is seen, the TLR4 model fits very well with wild-type dynamic experimental expression for all four investigated genes.
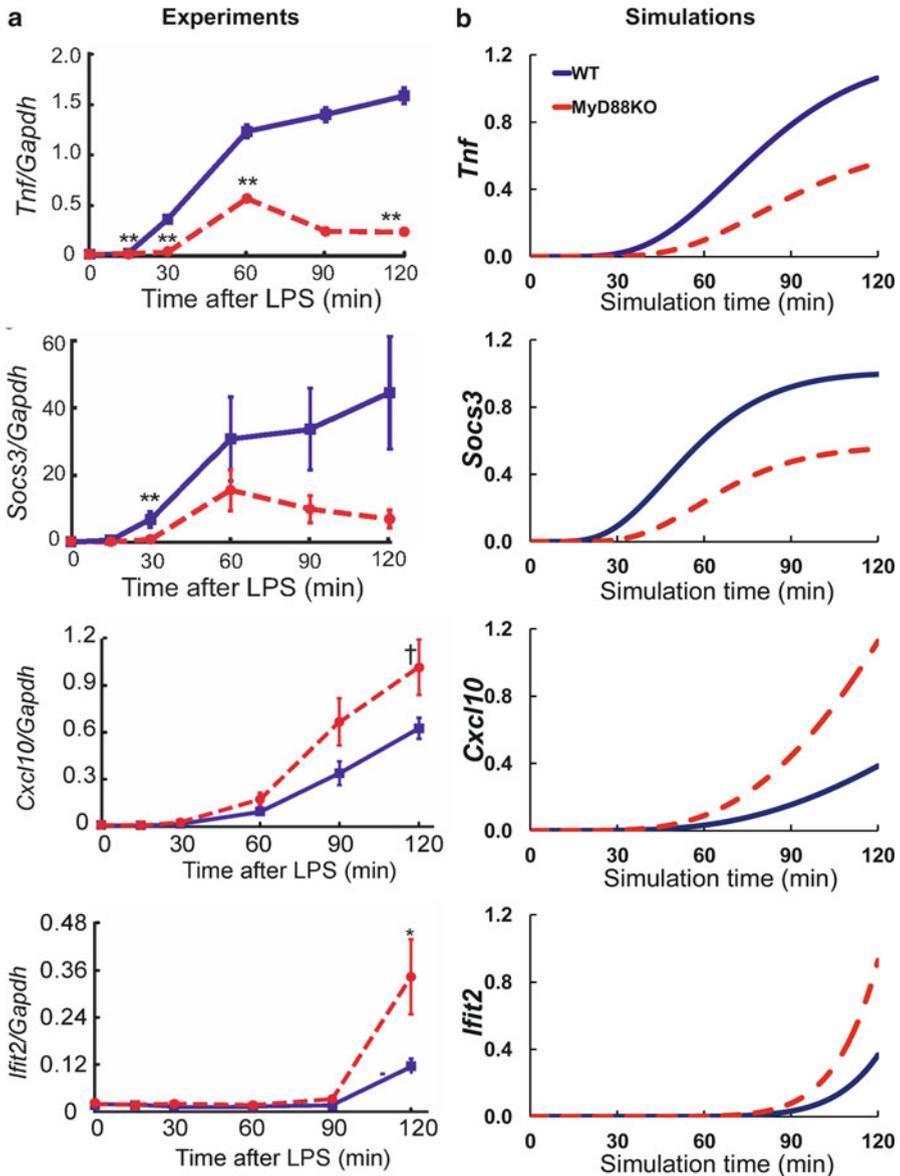
Fig. 5.1 *Temporal experimental and simulation dynamics of TLR4-induced gene expressions.*
(**a**) Experimental *Tnf*, *Socs3*, *Cxcl10*, and *Ifit2* mRNA levels (normalized over *Gapdh*) after lipo-
polysaccharide (LPS) treatment in wild-type (*blue lines*) and MyD88 knockout (KO) (*red dotted
lines*) macrophages measured by qRT-PCR. Values are average of six independent cultures
(means±SEM). **$p<0.01$ versus wild-type. (**b**) Computational simulations (arbitrary units) of
Tnf, *Socs3*, *Cxcl10*, and *Ifit2* in the presence (*blue lines*) and absence (*red dotted lines*) of MyD88
upon TLR4 activation. Note that beyond 60 min, *Tnf* and *Socs3* expression for MyD88-deficient
macrophages was downregulated, presumably because of posttranscriptional complexities or auto-
crine negative feedback mechanisms, such as the role of A20, which are not considered in the
model (Modified from Selvarajoo et al. [1])

To observe the effects of the mutant, the expression levels of the four genes are next investigated in MyD88 knockout (KO). Notably, LPS stimulation on MyD88-deficient macrophages showed increased activation of *Cxcl10* and *Ifit2* compared to the wild-type (Fig. 5.1a, red, Table 5.1). According to our computational model (Fig. 5.1b, red), which also shows similar dynamics, the enhancement of TRAM-dependent genes in MyD88 KO is caused by an increased flux along the TRIF/TRAM-dependent pathway through *SFR* (*response rule 4*; Box 4.2) (Fig. 5.2).

According to the law of signaling flux (mass flow) conservation, targeting molecules at a pathway junction, in general, will affect the fluxes of the alternative pathways. That is, if the molecules at the pathway junction are now increased, activation of the alternative pathways will be reduced. To illustrate this, MyD88 reaction kinetics (TLR4 → MyD88) in the model was increased by twofold (to represent overexpression), and the consequent results show increased MyD88, NF-κB, and *Tnf* and reduced TRAM, IRF3, and *Cxcl10* activities (Fig. 5.2, green). This result demonstrates the balancing or compensatory nature of signaling pathways. Thus, when MyD88 at a pathway junction is removed or overexpressed, the activation of the entire alternative TRAM pathway is enhanced or reduced, respectively.

Experimental Demonstration of *SFR*

To examine whether *SFR* occurs in actual cells, macrophages from wild-type and MyD88-deficient mice were measured for TRAM-dependent IRF3 phosphorylation, as well as activation of MAP kinases JNK, ERK, p38, and NF-κB (IκBα degradation) after LPS stimulation. MAP kinases and NF-κB activation were impaired and delayed in MyD88-deficient macrophages compared to wild-type macrophages and notably, as predicted by the computational model, increased IRF3 phosphorylation was observed for MyD88-deficient macrophages (Fig. 5.3). These data support the model prediction of increased activation of the TRAM-dependent pathway in MyD88-deficient macrophages, verifying the occurrence of *SFR*.

To experimentally identify the biological mechanism for *SFR*, a competition assay in cultured cells by overexpressing the TLR4 cytoplasmic tail, MyD88, and TRAM was performed. The TLR4 (TIR domain) carries a multifunctional docking site where MyD88, Mal, TRAM, and TRIF adaptor molecules bind with common specificity. Figure 5.4 shows that TRAM interacted with the TLR4 cytoplasmic tail in HEK293T cells. When the concentration of MyD88 was increased, MyD88 preferentially competed TRAM from TLR4 in a dose-dependent manner, indicating that MyD88 and TRAM bind to TLR4 competitively. This finding suggests that increased TRAM binding with TLR4 in the absence of MyD88 is the result of loss of competition between MyD88-dependent and TRAM-dependent pathways. These data provide the biological mechanism for *SFR*.

Table 5.1 Toll-like receptor (TLR)4 model reactions and parameter values

| Number	Reaction	Formula	Parameter value (1/s)	Description
MyD88-dependent pathway				
1	TLR4 → MyD88/MAL	k1* TLR4	k1 = 0.02, k1 = 0.0 (MyD88 KO), k1 = 0.04 (MyD88 overexpressed twice)	MyD88 and MAL are recruited to TLR4
2	MyD88 → IRAK4/IRAK1	k2* MyD88	k2 = 0.0017 (wild-type)	IRAK4 and IRAK1 bind to TLR-MyD88/MAL complex
3	IRAK4/IRAK1 → TRAF6	k3* IRAK	k3 = 0.0167	Phosphorylated IRAKs bind to TRAF6 and are released from MyD88
4	TRAF6 → TAB/TAK	k4* TRAF6	k4 = 0.0167	TRAF6 binds to TAB/TAK complex
5	TAB/TAK → IKKc	k5* TABTAK	k5 = 0.0035	Activation of MAP kinase and IKK complex via TAB/TAK complex
6	TAB/TAK → MKK1	k6* TABTAK	k6 = 0.00167	
7	TAB/TAK → MKK3	k7* TABTAK	k7 = 0.001	
8	TAB/TAK → MKK4	k8* TABTAK	k8 = 0.00167	
9	IKKc → IκBα/NF-κB	k9* IKKc	k9 = 0.0167	Phosphorylation of IκBα/NF-κB via IKK complex
10	MKK3/6 → p38	k10* MKK3/6	k10 = 0.0167	Activation of p38 via MKK3/6
11	MKK4/7 → JNK	k11* MKK4/7	k11 = 0.0167	Activation of JNK via MKK4/7
12	MKK1/2 → ERK	k12* MKK1/2	k12 = 0.0167	Activation of ERK via MKK1/2
13	IκBα/NF-κB → p65/p50	k13* IκBα/NF-κB	k13 = 0.0333	Release of p65/p50 (NF-κB) after IκB phosphorylation
14	p38 → p38n	k14* p38	k14 = 0.0067	p38 translocates to the nucleus
15	JNK → JNKn	k15* JNK	k15 = 0.0067	JNK translocates to the nucleus
16	ERK → ERKn	k16* ERK	k16 = 0.0067	ERK translocates to the nucleus
17	p65/p50 → NF-κBn	k17* p65/p50	k17 = 0.0167	p65/p50 (NF-κB) translocates to the nucleus
18	p38n → AP1	k18* p38n	k18 = 0.00567	MAP kinases activate AP-1
19	JNKn → AP1	k19* JNKn	k19 = 0.00567	
20	ERKn → AP1	k20* ERKn	k20 = 0.00567	
21	AP1 → AP1deg	k21* AP1	k21 = 0.000667	AP-1 degradation
22	AP1 → TNFag1	k22* AP1	k22 = 0.0007	AP-1-DNA binding to activate *Tnf* transcription
23	NF-κBn → TNFag1	k23* NF-κB	k23 = 0.0001	NF-κB-DNA binding to activate *Tnf* transcription

24	TNFag1 → TNFag2	k24=0.01	k24* TNFag2	Delay reactions from nuclear processes leading to the transcription of *Tnf*, e.g., chromatin remodeling, transcription factor initiation, and complex formation
25	TNFag2 → TNFag3	k25=0.001	k25* TNFag2	
26	TNFag3 → TNFa	k26=0.001	k26* TNFag3	*Tnf* transcription
27	TNFa → TNFadeg	k27=0.00001	k27* TNFα	*Tnf* conversion to TNF-α and *Tnf* degradation (combined)
28	AP1 → Socg1	k28=0.000167	k28* AP1	AP1-DNA binding to activate *Socs3* transcription
29	NF-κBn → Socg1	k29=0.000167	k29* NF-κBn	NF-κB-DNA binding to activate *Socs3* transcription
30	Socg1 → Socg2	k30=0.002	k30* Socg1	Delay reactions from nuclear processes leading to the transcription of *Socs3*, e.g., chromatin remodeling, transcription factor initiation, and complex formation
31	Socg2 → Socs3	k31=0.001	k31* Socg2	
32	Socs3 → Socsdeg	k32=0.00001	k32* Socs3	*Socs3* conversion to Socs-3 and *Socs3* degradation (combined)
TRAM-dependent pathway				
33	TLR4 → I1	k33=0.01	k33* TLR4	Additional intermediates acting along TRAM-dependent pathways
34	I1 → I2	k34=0.01	k34* I1	
35	I2 → I3	k35=0.01	k35* I2	
36	I3 → I4	k36=0.01	k36* I3	
37	I4 → TRAM	k37=0.01	k37* I4	
38	TRAM → TRIF	k38=0.0067	k38* TRAM	TRIF binds to TLR–TRAM complex
39	TRIF → TBK1	k39=0.01	k39* TRIF	TBK1 binds to TRIF at the complex (Note that TBK1 is lumped with IKKepsilon)
40	TRIF → TRAF6	k40=0.005	k40* TRIF	TRIF binds to TRAF6 from the MyD88-dependent pathway
41	TRIF → RIP1	k41=0.005	k41* TRIF	TRIF binds to RIP1, which activates AIP1
42	RIP1 → AIP1	k42=0.00167	k42* RIP1	
43	RIP1 → IKKc	k43=0.00167	k43* RIP1	RIP1 activates IKK complex
44	AIP1 → MKK1/2	k44=0.001	k44* AIP1	Activation of MAP kinase kinase by AIP1
45	AIP1 → MKK3/6	k45=0.001	k45* AIP1	
46	AIP1 → MKK4/6	k46=0. 001	k46* AIP1	

(continued)

Table 5.1 (continued)

Number	Reaction	Formula	Parameter value (1/s)	Description
47	TBK1 → IRF3c	k47* TBK1	k47 = 0.00333	IRF3 binds TBK1 at the complex
48	IRF3c → IRF3n	k48* IRF3c	k48 = 0.000167	IRF3 phosphorylation, release, and translocation to the nucleus
49	IRF3n → IF1	k49* IRF3n	k49 = 0.0003	IRF3-DNA binding to activate transcription of *Ifit2*
50	IRF3n → IPG2	k50* IRF3n	k50 = 0.000567	IRF3-DNA binding to activate *Cxcl10* transcription
51	TBK1 → cRel/p50c	k51* TBK1	k51 = 0.0006	Phosphorylation of cRel/p50 via TBK1
52	cRel/p50c → cRel/p50n	k52* cRel/p50c	k52 = 0.1	cRel/p50 (NF-κB) translocates to the nucleus toward *Cxcl10* transcription
53	cRel/p50n → NF-κBn	k53* cRel/p50n	k53 = 0.6	cRel/p50 (NF-κB) translocates to the nucleus towards *Tnf*, *Socs3* transcription
54	IRF3n → IPG1	k54* IRF3n	k54 = 0.0003	IRF3-DNA binding to activate *Cxcl10* transcription
55	NF-κBn → IPG1	k55* NF-κBn	k55 = 1.67e-012	NF-κB -DNA binding to activate *Cxcl10* transcription
56	IPG1 → IPG2	k56* IPG1	k56 = 0.000167	Delay reaction from nuclear processes leading to the transcription of *Cxcl10*
57	IPG2 → Cxcl10	k57* IPG2	k57 = 0.000167	*Cxcl10* formation
58	Cxcl10 → IPdeg	k58* Cxcl10	k58 = 0.000167	*Cxcl10* conversion to CXCL10 and *Cxcl10* degradation (combined)
59	IF1 → IF2	k59* IF1	k59 = 0.0001	*Delay reactions from nuclear processes leading to the*
60	IF2 → IF3	k60* IF2	k60 = 0.00001	*transcription of Ifit2*
61	IF3 → IF4	k61* IF3	k61 = 0.00001	
62	IF4 → Ifit2	k62* IF4	k62 = 0.0001	*Ifit2 formation*
63	Ifit2 → Ifit2deg	k63* Ifit2	k63 = 1.0e-08	*Ifit2 conversion to IFIT2 and Ifit2 degradation (combined)*

Note that 1 mol or 6.023*10²³ molecules of LPS pulse is used to stimulate the model. The simulation plot of each molecule is finally normalized to wild-type condition peak value
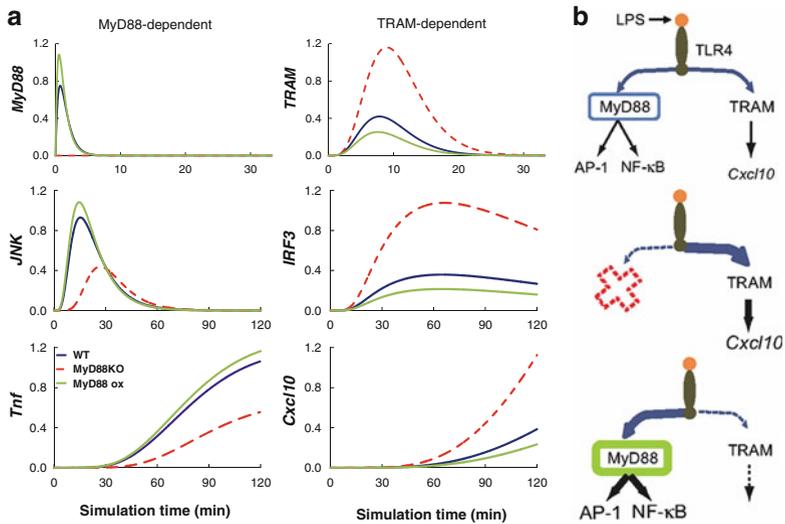
Fig. 5.2 *Illustration of signaling flux redistribution* (*SFR*) *in TLR4 activation*. (**a**) Simulation profiles (arbitrary units) of *MyD88*-dependent (*MyD88*, *JNK*, *Tnf*) and TRAM-dependent (*TRAM*, *IRF3*, and *Cxcl10*) in wild-type (*blue lines*), MyD88 KO (*red dotted lines*), and twofold overexpression (*green lines*) of MyD88. (**b**) Schematic of *SFR*. *Top*: Wild-type. Fluxes propagate through both the MyD88-dependent and TRAM-dependent pathways. *Middle*: MyD88 KO. More fluxes propagate or overflow through the TRAM-dependent pathway, resulting in increased *Cxcl10*. *Bottom:* MyD88 overexpression by twofold reduces *Cxcl10*
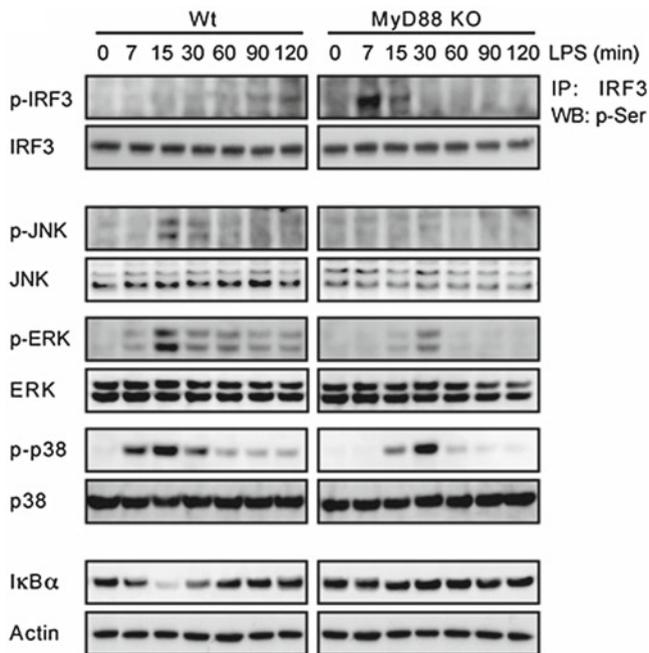
Fig. 5.3 *Enhanced TRAM-dependent pathway in the absence of MyD88*. Macrophages were treated with LPS (100 ng/ml) for indicated periods. Cell lysates were analyzed for IRF3, JNK, ERK, p38 phosphorylation, and NF-κB (degradation of IκBα) using Western blot analysis with actin as a loading control. *Wt*, wild-type. Note that as living cells show variability between cultures or times, the model simulations are compared in qualitative or semiquantitative manner (Adapted from Selvarajoo et al. [1])

Fig. 5.4 *Competing TRAM and MyD88 at TLR4*. MyD88 and TRAM compete for TLR4 in GST pull-down assay. GST or the GST-tagged TLR4 were expressed in HEK293T cells with Myc-tagged MyD88 or Flag-tagged TRAM. After GST pull-down, Western blotting was performed (Obtained from Selvarajoo et al. [1])
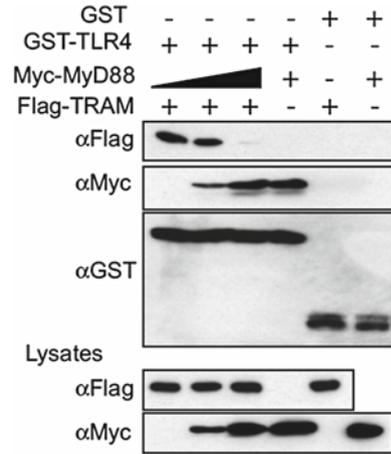

SFR at Other Pathway Junctions

To check whether *SFR* is a general property of signal transduction at pathway junctions, another branch point of the TRAM-dependent component of the TLR4 pathway is next analyzed: TRIF to TBK1, TRAF6, and RIP1. Because TBK1 and TRAF6 compete to bind to the N-terminal domain of TRIF, the consequence of removing TRAF6 molecules on the TRAM-dependent pathway is investigated. In silico TRAF6 KO simulations show lower induction of *Tnf*, but greater induction of *Cxcl10*, because of the increased propagation of signaling flux through the TRIF-TBK1-IRF3 route (Fig. 5.5a). Parallel bench experiments were performed in generating macrophages from wild-type and TRAF6-deficient mice and treating them with LPS. Although *Tnf* expression was lower, as expected, *Cxcl10*, *Ifit1*, and *Ifit2* induction were higher in TRAF6-deficient macrophages than in wild-type macrophages (Fig. 5.5b, c).

Because cells are able to execute numerous processes using only a limited set of interaction domains that have flexible binding properties, we believe *SFR* at these domains can enhance or impair alternative pathways when a competing molecule such as MyD88 or TRAF6 is removed or increased (Fig. 5.6). In addition to TRAF6 and TBK1, RIP1 and RIP3 also compete for TRIF, and binding of RIP3 to TRIF has been shown to be increased in the absence of RIP1 [2]. Moreover, it was shown that the suppression of a newly discovered TRIF-interacting partner, a disintegrin and metalloprotease (ADAM)15, showed enhanced LPS-mediated proinflammatory cytokine MMP mRNA expression, rhinovirus 16, and vesicular stomatitis virus-mediated proinflammatory cytokine production [3].

The observation of enhanced alternative pathways when molecules at a pathway junction are removed is not restricted to TLR4 signaling. One study on HELA and H460 cells focusing on TRADD and RIP, which binds to intracellular TNFR1, demonstrated that deletion of either molecule results in enhancement of alternative
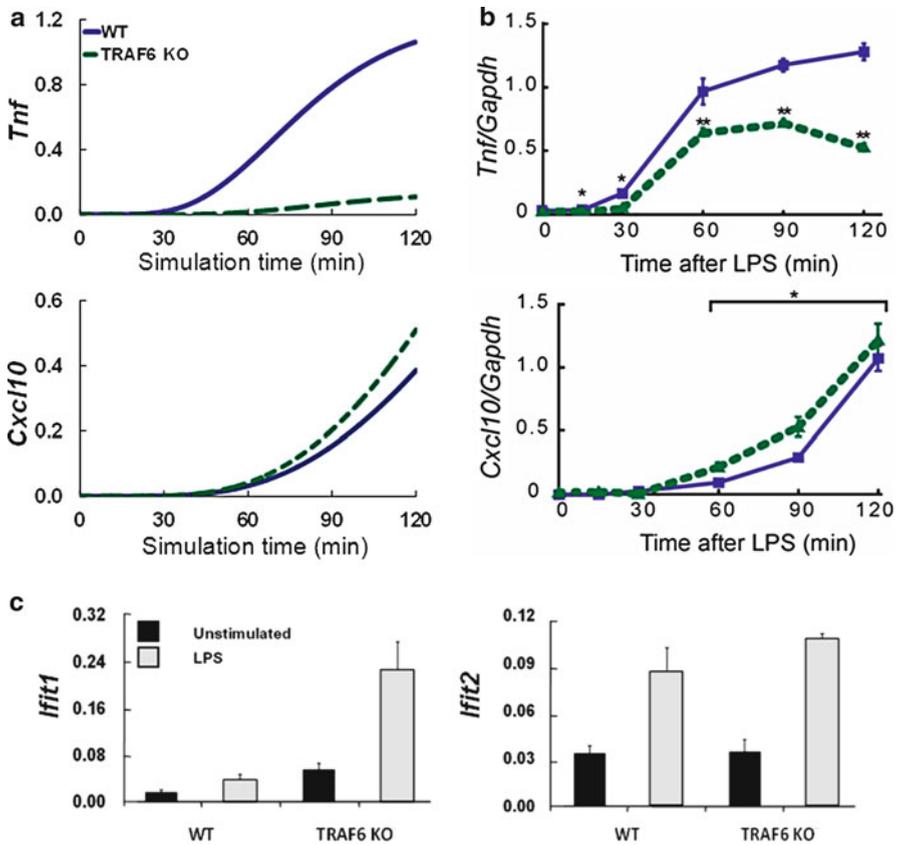
Fig. 5.5 *Enhancement of TRAM-dependent pathway in TRAF6 KO*. Simulations (**a**) and mRNA expressions of *Tnf* and *Cxcl10* (**b**), in wild-type (*blue lines*) and TRAF6 KO (*green dotted lines*). In (**b**), four independent macrophage cultures were analyzed. Means ± SEM. *$p < 0.05$, **$p < 0.01$ versus wild-type. (**c**) *Ifit1* and *Ifit2* transcripts in wild-type (Traf6+/+) and Traf6−/− macrophages, unstimulated (*filled bars*) or lipopolysaccharide (LPS) (*gray bars*) for 60 min were analyzed by qRT-PCR and normalized to GAPDH. Values represent average of six independent cultures (means ± SEM)

pathways in tumor necrosis factor (TNF) stimulation [4]. In another study, markedly elevating Ser/Thr phosphorylation in rat hepatoma Fao cells reduced alternative insulin-induced Tyr phosphorylation of IRS-1 and IRS-2, which significantly reduced their ability to interact with the juxtamembrane region of the insulin receptor, resulting in an impaired downstream signal [5]. Reversing these effects by incubating cell extracts with alkaline phosphatase strongly indicated that insulin resistance is associated with enhanced Ser/Thr phosphorylation of IRS-1 and IRS-2. Thus, *SFR* is a general property occurring at signaling pathway junctions. Although there may be several biological mechanisms for *SFR*, we propose three possibilities of action: competition, physical blocking, or conformational change (Fig. 5.7).
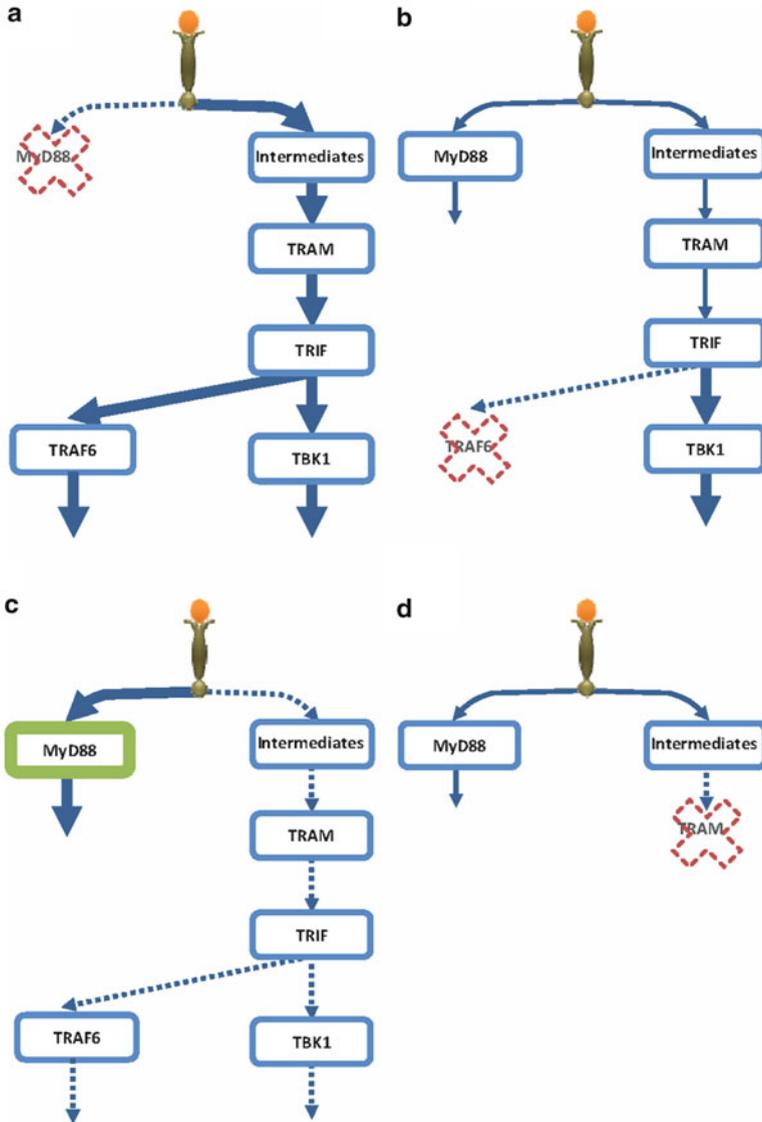
Fig. 5.6 *Schematic representation of signaling flux redistribution* (*SFR*). (**a**) Removal of MyD88 results in enhancement of TRAM-dependent pathway. (**b**) Removal of TRAF6 results in enhancement of TRAM-dependent pathway downstream of TRIF. (**c**) Overexpression of MyD88 downregulates the TRAM-dependent pathway. (**d**) Removal of TRAM does not enhance the MyD88-dependent pathway because of upstream intermediates

Fig. 5.7 *Proposed mechanisms of action for SFR*. (**a**) Competition: Molecules X and Y compete to bind with molecule Z. X and Y share binding sites at Z. (**b**) Steric hindrance: When X binds to Z, the complex prevents the binding of Y to another binding site at Z. (**c**) Conformational change: When X binds to Z, structural changes to Z lowers the affinity of Y binding to Z
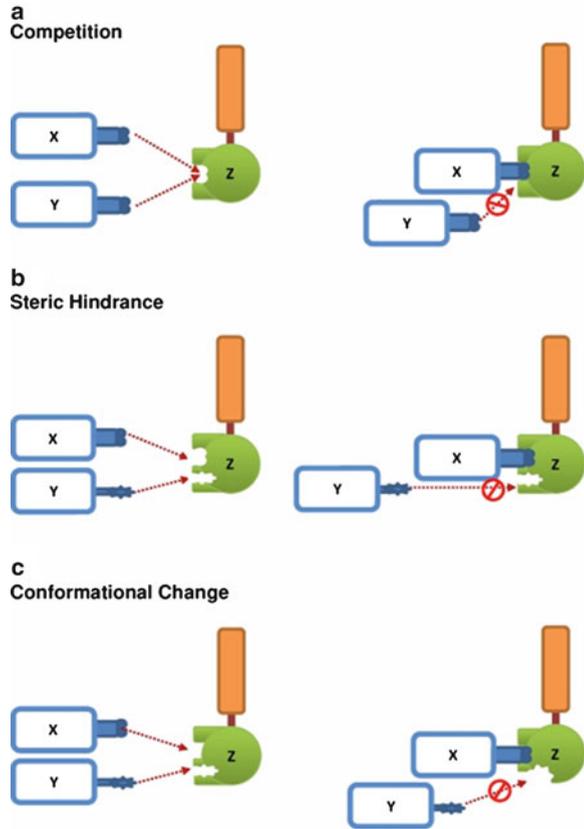
In summary, the gain- or loss-of-function mutation of MyD88 was investigated in this chapter. The TLR4 computational model built on the perturbation-response approach and the law of mass flow (signaling flux) conservation shows that the removal and addition of MyD88 enhances and impairs, respectively, the alternative TRAM-dependent pathway through *signaling flux redistribution* (*SFR*) at pathway branches. *SFR* was experimentally verified where MyD88-deficient macrophages stimulated with LPS showed enhancement of TRAM-dependent pathway based on increased induction of *Cxcl10* and *Ifit2*. Furthermore, increasing the amount of MyD88 in cultured cells showed decreased TRAM binding to TLR4. The enhancement of entire TRAM-dependent pathways in MyD88 KO through *SFR* provides an alternative mechanism that does not require any physical negative crosstalk interaction between the MyD88 and TRAM molecules.

Investigating another TLR4 pathway junction, from TRIF to TRAF6, RIP1, and TBK1, the removal of MyD88-dependent TRAF6 increased expression of TRAM-dependent *Cxcl10*, *Ifit1*, and *Ifit2*. *SFR*, therefore, is a novel mechanism for regulating the balance between alternative pathways and can be successfully used to predict

the molecular dynamics of entire signaling pathways. Here, although *SFR* have been demonstrated for molecules with a common binding domain, *SFR* might also occur between molecules with different binding domains at pathway junctions from the law of mass flow conservation. Thus, *SFR* may be used to understand the enhancement or repression of alternative pathways in diseases where gain- or loss-of-function mutations occur. In a subsequent chapter on TRAIL signaling in cancer, the utility of *SFR* is investigated for enhancing apoptosis in resistant cancer cells.

References

1. Selvarajoo K, Takada Y, Gohda J, Helmy M, Akira S, Tomita M, Tsuchiya M, Inoue J, Matsuo K (2008) Signaling flux redistribution at Toll-like receptor pathway junctions. PLoS One 3:e3430
2. Meylan E, Burns K, Hofmann K, Blancheteau V, Martinon F, Kelliher M, Tschopp J (2004) RIP1 is an essential mediator of Toll-like receptor 3-induced NF-κB activation. Nat Immunol 5:503–507
3. Ahmed S, Maratha A, Butt AQ, Shevlin E, Miggin SM (2013) TRIF-mediated TLR3 and TLR4 signaling is negatively regulated by ADAM15. J Immunol 190:2217–2228
4. Jin Z, El-Deiry WS (2006) Distinct signaling pathways in TRAIL- versus tumor necrosis factor-induced apoptosis. Mol Cell Biol 26:8136–8148
5. Paz K, Hemi R, LeRoith D, Karasik A, Elhanany E, Kanety H, Zick Y (1997) A molecular basis for insulin resistance. Elevated serine/threonine phosphorylation of IRS-1 and IRS-2 inhibits their binding to the juxtamembrane region of the insulin receptor and impairs their ability to undergo insulin-induced tyrosine phosphorylation. J Biol Chem 272:29911–29918

Chapter 6
Investigating the TLR3 Signaling Dynamics

Along with Toll-like receptor (TLR)-7, -8, and -9, TLR3 is an intracellular member of the TLR superfamily (see Chap. 3). It plays a crucial role in the mammalian innate immune response against viral attacks by recognizing double-stranded RNA (dsRNA) or its synthetic analogue polyinosinic-polycytidylic acid (poly (I:C)). TLR3 is expressed in several cell types including macrophages, murine embryonic fibroblasts (MEFs), and dendritic cells; however, it has not been detected in B cells, T cells, and NK cells. In contrast to all other TLRs, the TLR3 response is independent of the adaptor protein MyD88. The specificity of the TLR3 response possibly results from the occurrence of an alanine residue in a critical region of its cytoplasmic domain, in contrast to the proline residue utilized by MyD88 found in other TLRs [1]. Thus, TLR3 initiates its response depending only on the adaptor protein TRIF and does not involve TRAM [2].

The recruitment of TRIF mediates the signaling process through the activation of key transcription factors IRF-3, -7, NF-κB, and AP-1, leading to the production of interferon (IFN)-β and other proinflammatory cytokines such as tumor necrosis factor (TNF) and interleukin (IL)-6. The N-terminal of TRIF recruits the TRAF3 and TBK1 complex and leads to IRF3 phosphorylation, dimerization, and translocation to the nucleus for inducing IFN-β expression. TRIF binds with RIP1 at C-terminal (RHIM domain) and subsequently activates the IKK complex and NF-κB. TNFR type 1-associated DD protein (TRADD) has also been shown to be involved in TLR3 signaling [3, 4].

Although the signaling molecules and their cascades have been broadly investigated, the dynamic outcome of signal transduction between wild-type and genetic mutations remains poorly understood. Moreover, the experimental observations of TLR3 signaling under various genetic mutants have shown controversial roles of certain molecules between different cell types. For instance, although TRAF6 has been shown to be dispensable for TLR3-induced NF-κB in poly (I:C) stimulated macrophages [3], it is crucial for NF-κB activation in MEFs [5]. Such data indicate that different cell types may possess different variant of signaling mechanisms and, therefore, one cannot combine data obtained from different cell types to create a unified TLR3 signaling topology. Instead, independent cell type analysis should be performed.

Characterizing TLR3 Signaling Topology in Macrophages

Here, the signaling topology in murine macrophages is investigated. Similar to the TLR4 study, the investigation of the TLR3 pathway begins by literature/database creation of the signaling topology (Fig. 6.1). dsRNA- or poly (I:C)-stimulated TLR3 triggers TRIF-dependent response by the recruitment of TRIF to the cytoplasmic domain of the receptor, which then allows RIP1, TRAF6, and TRAF3 to bind with TRIF. Moreover, TRADD is also known to mediate the TRIF-dependent signaling. The sequences of events result in the activation of MAP kinases (MKK1/2, MKK3/6, and MKK4/7) and IκB kinase complex; MKK1/2, MKK3/6, and MKK4/7 activate ERK, JNK, and p38, respectively, and IκBα degradation releases NF-κB. TBK1 phosphorylates IRF-3 and -7. ERK, JNK, and p38 translocate to the nucleus and activate the transcription factor AP-1, and NF-κB and IRF-3/7 translocate to the nucleus. AP-1 and NF-κB bind to the promoter regions of cytokine genes such as *Tnf* and *Il6*, whereas IRF-3/7 together with NF-κB bind to the promoter region of chemokine genes such as *Cxcl10* and *Ccl5* and induce their transcription.

The Prediction of Missing Intermediary Processes

To analyze the complex dynamic interplay of the various intracellular signaling molecules in the regulation of NF-κB, JNK, and p38 in poly (I:C) stimulation, a computational model of the TLR3 signaling is developed (see Chap. 2 for details of
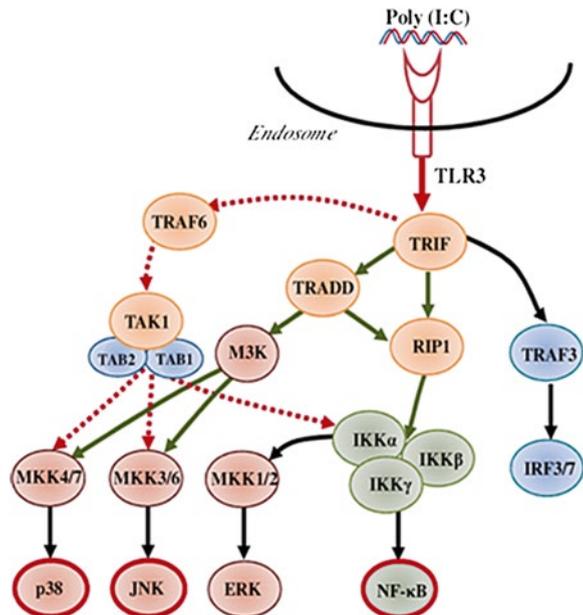
Fig. 6.1 *Schematic representation of Toll-like receptor* (*TLR*)*3 pathway topology for macrophages. Dotted lines* indicate weak activation or dispensable pathway

modeling approach). The temporal experimental data used to develop and test the model for the relevant molecules were obtained for three conditions [wild-type, TRAF6 knockout (KO), and TRADD KO] (Fig. 6.2a) [3, 6]. The activation levels (NF-κB, JNK, and p38) were quantified from the Western blot data using ImageJ (http://rsbweb.nih.gov/ij/) and normalized with the peak intensity. That is, for X_i at time t:

$$\hat{X}_i(t) = \frac{X_i(t_{\exp}) - X_i(0)}{\max(X_i(t_{\exp})) - X_i(0)}, \quad t_{\exp} = \{0, 10, 20, 45, 60, 90\}$$

where $X_i(t_{\exp})$ is the raw experimental value obtained from quantification, and $\max(X_i(t_{\exp}))$ indicates the peak value obtained among all time points. Note that intensity values lower than 0.05 are set to zero as they are likely to possess significant signal-to-noise ratio (error).

For the computational model, each signaling response (i.e., the rate of activation of each signaling molecule) is represented by $\dfrac{d\delta X}{dt} = J\delta X$, where δX is relative activated concentration of signaling molecules and the parameters (elements of J) are chosen to fit the semiquantitative experimental profiles of NF-κB, JNK, and p38 of wild-type macrophages stimulated with poly (I:C) (Fig. 6.2a, WT; model A). The parameter values are estimated to fit with the normalized experimental profiles. The fitting of the parameter values is obtained by minimizing the error between experimental and simulation profiles of all investigated molecules by using a genetic algorithm. However, we deliberately constrained the kinetics between TRIF and TRAF6, as it was previously shown that TRAF6 is dispensable in macrophage TLR3 signaling [3].

Figure 6.2b shows the TLR3 model A simulations of NF-κB, JNK, and p38 activity for wild-type. In simulations, the time to reach peak values is between 3 and 12 min, in contrast to experiments where it is between 20 and 40 min. Clearly, this model could not explain the delayed experimental activation of NF-κB, JNK, and p38. The time delay processes of signaling events can be considered as missing molecules/complex formation or spatial movement of molecules (*response rule 1*, Box 4.2; Chap. 4). The deterministic kinetic evolution equation used in our model (Eq. 2.1; Chap. 2), can include such information by setting total derivative of time to partial derivative in time and space. In other words, Jacobian matrix J can contain temporal and spatial information of the network process. Because the perturbation-response model does not perform spatial simulation, time delay response can be lumped as missing molecules/processes in the network. For example, in the TLR4 model (Chap. 4), delayed activation of the TRIF-dependent pathways was achieved by using a number of additional response reactions representing missing signaling features (molecules/processes, spatial movements, or complex formation) in the original network (Fig. 4.6).

To investigate and locate the likely position of the necessary missing intermediary steps in the TLR3 pathways predicted by the model, further literature survey was performed. TRIF was found to directly bind to the TIR domain of TLR3 and
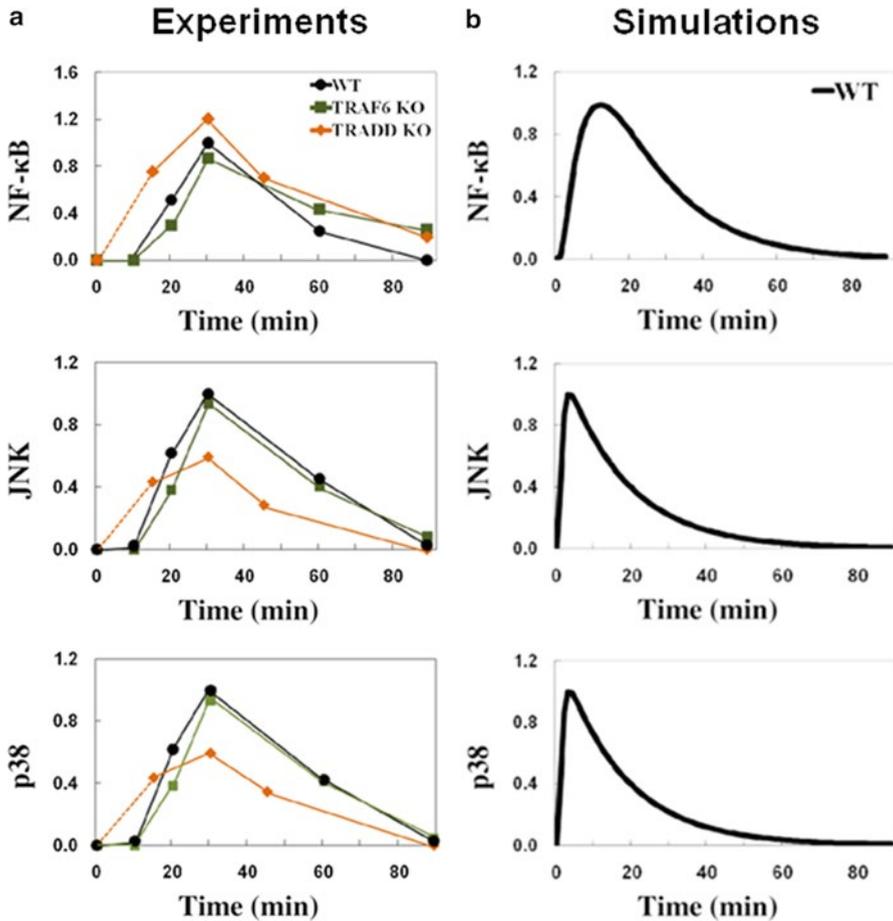
Fig. 6.2 *TLR3-induced NF-κB and MAP kinase activation dynamics.* (**a**) Experimental activation profiles of NF-κB, JNK, and p38, respectively, in wild-type (WT) (*black circles*), TRAF6 KO (*green squares*), and TRADD KO (*orange diamonds*) obtained from references [3, 6]. The activation levels were quantified from the Western blots using ImageJ. (**b**) Model A simulations of NF-κB, JNK, and p38 activation, respectively, in wild-type (WT). *x*-axis, time in minutes; *y*-axis, relative activation levels. Note: As TRADD KO data are unavailable at 10 min (earliest at 15 min), the delayed activation observed for WT and TRAF6 KO could not be confirmed. Therefore, a *dotted line* is used to connect 0- and 15-min time points

did not require TRAM for its activation [7]. Thus, it is unlikely that missing intermediary steps exist between TLR3 and TRIF. Furthermore, TLR3 KO and TRIF KO both showed a similar response, the abolished activation of NF-κB and MAP kinases [7]. These data led to the hypothesis that the missing intermediary steps (e.g., signaling molecules or processes) are upstream of TLR3, and the model is updated to begin simulation not from TLR3, but rather from poly (I:C) downward (Fig. 6.3a;
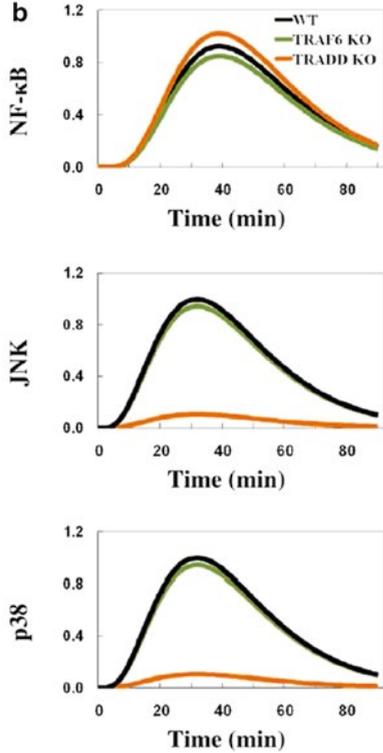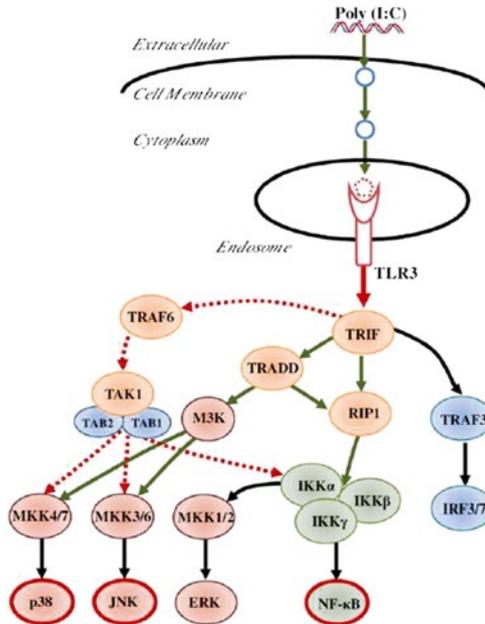
Fig. 6.3 *Prediction of missing steps before poly (I:C)/TLR3 binding* (*model B*). (**a**) Schematic representation of TLR3 model after adding three signaling intermediates upstream of TLR3 representing uncharacterized cellular processes (*blue lines*) and TLR3-ectodomain dimerization (*red dotted lines*). Note: It is not possible to equate the three intermediary steps from the model to represent exactly three actual biological events because spatial transport processes might be one of the candidates for the time delay. (**b**) Model B simulations of NF-κB, JNK, and p38 activation, respectively, in the wild-type (WT) (*black lines*), TRAF6 KO (*green lines*), and TRADD KO (*orange lines*). *x*-axis, time in minutes; *y*-axis, relative activation profile

model B). Each new uncharacterized molecule/process is also represented as a signaling intermediate in the model.

To obtain delayed activation of wild-type NF-κB and MAP kinases in accordance with experimental data, that is, null activation until about 10 min, peak values around 30 min, and reduced activation after 60 min for all molecules, three to four intermediary steps (signaling intermediates) are required (Fig. 6.3a, b; WT). Having fewer or more intermediary steps resulted in peak value being reached faster or slower than the experimental peak, respectively (data not shown) (Note that the actual number of intermediates cannot be predicted accurately by the model. Nevertheless, the predictions highlight that important missing features exists that require further experimental investigations.). Thus, the revised model B with novel signaling intermediates produces a better fit with wild-type data. However, will it sufficiently simulate TRAF6 KO and TRADD KO?

Identification of Novel Pathways for MAP Kinases Activation

We wondered whether the revised TLR3 model could successfully simulate the activation of NF-κB, JNK, and p38 in all three conditions: wild-type, TRAF6 KO, and TRADD KO. Thus, to further test the predictive capability of the model, in silico simulations of TRAF6 KO and TRADD KO are performed. To create the KO condition from the wild-type model, the reactions of the respective KO molecule are set to null, while all other model parameters retain their original wild-type values.

First, TRAF6 KO simulations matched the experimental data, that is, the removal of TRAF6 only slightly downregulated NF-κB, JNK, and p38 activation (Fig. 6.3b; TRAF6 KO). Second, for TRADD KO, NF-κB activation was slightly increased in experiments (Fig. 6.2a). This result was recapitulated by model B, which suggests the enhancement of NF-κB activation in TRADD KO is the result of signaling flux redistribution (*SFR*) (*response rule 5*, Box 4.2; Chap. 4) (Fig. 6.3b; TRADD KO). However, in contrast to experimental results, which showed only a small downregulation, simulations of JNK and p38 showed almost abolished activation. The failure of simulation profiles suggests, in actual cells, a novel pathway might exist that compensates the loss of MAP kinase activation in TRADD KO (*response rule* 3, *missing flux*, Box 4.2; Chap. 4).

Macrophages with TRIF mutation treated with poly (I:C) showed abolishment of MAP kinase ERK activation [8], and all MAP kinases showed similar kinetics in wild-type and TRAF6 KO [3]. Thus, a novel pathway from TRIF to MAP kinases independent of RIP1, TRADD, and TRAF6 was hypothesized, and added into the revised model (Fig. 6.4a). The parameter values between TRIF to RIP1, TRIF to TRADD, and TRIF to the novel pathway are readjusted to fit wild-type NF-κB, JNK, and p38 activation. Remarkably, the simple addition in the model resulted in simulations of all three molecules that matched the experimental outcome in all three conditions (Fig. 6.4b; model C, Table 6.1).

In summary, the analysis of the poly (I:C) stimulation in macrophages reveals the involvement of uncharacterized missing intermediary steps upstream of TLR3, and the existence of a key pathway from TRIF to JNK and p38, but not NF-κB activation (Fig. 6.4a). Although we have indicated three novel intermediates preceding TLR3 activation, in reality these can represent several actual missing molecules and signaling processes (Chap. 4). Around the time when we first built the original TLR3 model [9], Liu et al. demonstrated that TLR3-ectodomains dimerize before signal propagation [10]. These data indicate that TLR3-ectodomain dimerization could be one of the missing intermediary steps upstream of TLR3. Furthermore, the cell entry of poly (I:C) was revealed through the clathrin-dependent endocytic pathway [11]. These events could possibly represent the other intermediary steps. More recently, TLR4 interactor with leucine-rich repeats (TRIL) was shown to interact with TLR3 following poly (I:C) stimulation [12], and the cleaving of TLR3 by cathepsins B and H for signaling [13].

To investigate the possible pathways for JNK and p38 activation in poly (I:C) stimulation, reports indicate two other receptors known to recognize dsRNA: the retinoic-acid-inducible protein (RIG)-I and melanoma-differentiation-associated
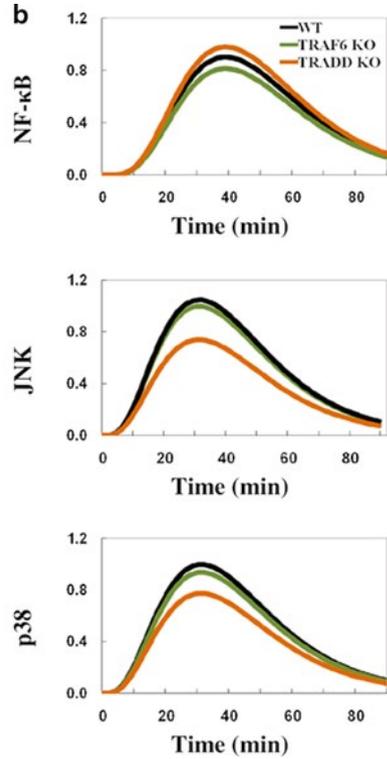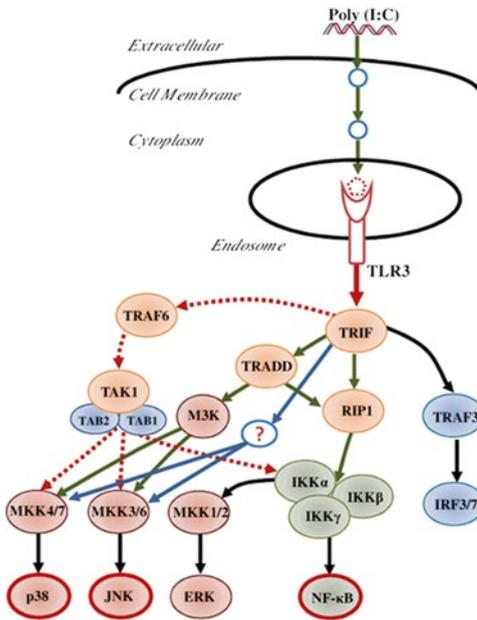
Fig. 6.4 *A novel pathway is crucial for MAP kinases activation in poly (I:C) stimulated macrophages* (*model C*). (**a**) Schematic representation of the final TLR3 model after adding novel pathway (*blue line*) from TRIF to activate MAP kinases. (**b**) Model C simulations of NF-κB, JNK, and p38 in wild-type (WT) (*black lines*), TRAF6 KO (*green lines*), and TRADD KO (*orange lines*). *x*-axis, time in minutes; *y*-axis, relative activation levels

gene (MDA)5 [14, 15]. These molecules, therefore, might be potential candidates for the novel features predicted by the model. However, RIG-I is unable to recognize poly (I:C) and the MDA5 signaling pathway is unknown to trigger MAP kinases. On the other hand, TRIF mutation showed abolishment of ERK activation [8], and all MAP kinases seem to possess similar kinetics in poly (I:C) stimulation [3]. Taken together, these data suggest the predicted pathway for JNK and p38 activation is through TRIF and not by RIG-1 or MDA5.

To find the possible candidates to be involved in the novel pathway, the literature was further surveyed. The TRAF family members, six to date, are well known to bind to the TIR domain of TRIF with their C-terminal [16–19], whereas two members of the RIP family, RIP1 and RIP3, are found to interact with TRIF through the RHIM domain found in RIP1 and RIP3 [20, 21]. RIP1, TRAF6, and TRAF3 already exist in the current TLR3 signaling, while TRAF1 was recently found to inhibit

Table 6.1 The final in silico TLR3 model reactions and parameter values

No.	Reaction	Formula	Parameter value (1/s)	Remarks
1	IM1 → IM2	k1*IM1	k1 = 0.002	Novel intermediates acting
2	IM2 → IM3	k2*IM2	k2 = 0.002	upstream of TLR3
3	IM3 → TLR3	k3*IM3	k3 = 0.002	representing uncharac-
				terized cellular events
4	TLR3 → TRIF	k4*TLR3	k4 = 0.001	TLR3 recruits TRIF
5	TRIF → TRAF6	k5* TRIF	k5 = 0.002	TRAF6 binds to TRIF
6	TRIF → IM4	k6*TRIF	k6 = 0.004	TRIF activates JNK through
				novel pathway molecule
7	TRIF → RIP1	k7*TRIF	k7 = 0.007	RIP1 binds to TRIF
8	TRIF → TRADD	k8*TRIF	k8 = 0.002	TRADD binds to TRIF
9	TRIF → TRAF3	k9* TRIF	k9 = 0. 01	TRAF3 binds to TRIF
10	TRAF6 → TAB/TAK	k10*TRAF6	k10 = 0.04	TRAF6 binds to TAB/TAK
				complex
11	RIP1 → IKK	k11*RIP1	k11 = 0.04	RIP1 activated IKK
				complex
12	TRADD → RIP1	k12*TRADD	k12 = 0.0001	RIP1 ubiquitination through
				TRADD
13	TRADD → MKKK	k13*TRADD	k13 = 0.04	TRADD activates JNK and
				p38 corresponding
				MKKK
14	MKKK → MKK3/6	k14*MKKK	k14 = 0.04	MKKK activates JNK
				through activation of
				MKK3/6
15	MKKK → MKK4/7	k15*MKKK	k15 = 0.04	MKKK activates p38
				through activation of
				MKK4/7
16	TAB/TAK → MKK4/7	k16* TAB/TAK	k16 = 0.03	Activation of MAP kinases
17	TAB/TAK → MKK3/6	k17*TAB/TAK	k17 = 0.007	and IKK via TAB/TAK
18	TAB/TAK → IKK	k18* TAB/TAK	k18 = 0.9	complex
19	IM4 → MKK3/6	k19* IM4	k19 = 0.04	The novel pathway
				molecule activates JNK
20	IM4 → MKK4/7	k20* IM4	k20 = 0.04	The novel pathway activates
				p38
21	IKK → NF-κB/IκB	k21*IKK	k21 = 0.00167	Phosphorylation of IκBα/
				NF-κB via IKK
				complex
22	IKK → p105/Tp12	k22*IKK	k22 = 0.0009	Activation of MKK1/2 via
23	p105/Tp12 → MKK1/2	k23* p105/Tp12	k23 = 0.003	IKK
24	NF-κB/IκB → NF-κBc	k24* NF-κB/IκB	k24 = 0.0333	Release of NF-κB after IκB
				phosphorylation
25	NF-κBc → NF-κBn	k25* NF-κBc	k25 = 1.0	NF-κB translocate to the
				nucleus
26	NF-κBn → NF-κBdeg	k26* NF-κBn	k26 = 0.99	NF-κB degradation
27	MKK1/2 → ERKc	k27*MKK1/2	k27 = 0.0167	Activation of ERK via
				MKK1/2
28	ERKc → ERKn	k28* ERKc	k28 = 0.99	ERK translocate to the
				nucleus

Table 6.1 (continued)

No.	Reaction	Formula	Parameter value (1/s)	Remarks
29	ERKn → AP-1	k29* ERKn	k29 = 0.99	ERK activates AP1
30	MKK3/6 → JNKc	k30*MKK3/6	k30 = 0.4	Activation of JNK via MKK3/6
31	JNKc → JNKn	k31*JNKc	k31 = 1.0	JNK translocate to the nucleus
32	JNKn → AP-1	k32* JNKn	k32 = 0.99	JNK activates AP1
33	MKK4/7 → p38c	k33*MKK4/7	k33 = 0.4	Activation of p38 via MKK4/7
34	p38c → p38n	k34* p38c	k34 = 1.0	p38 translocates to the nucleus
35	p38n → AP-1	k35* p38n	k35 = 0.99	p38 activates AP1
36	AP1 → AP-1 deg	k36* AP1	k36 = 0.085	AP1 degradation
37	TRAF3 → TBK1	k37*TRAF3	k37 = 0.0001	TRAF3-TBK1 interaction
38	TBK1 → IRF-3/7c	k38*TBK1	k38 = 0.333	IRF3/7 binds TBK1
39	IRF-3/7c → IRF-3/7n	k39*IRF-3/7c	k39 = 0.000167	IRF3/7 translocate to the nucleus
40	IRF-3/7n → IRF-3/7 deg	k40*IRF-3/7n	k40 = 0.0001	IRF3/7 degradation

Note that 1 mol or $6.023*10^{23}$ molecules of Poly I:C pulse is used to stimulate the model. The simulation plot of each molecule is finally normalized to its wild-type peak value

TRIF-mediated signaling [18, 19]. Thus, RIP3, TRAF2, TRAF4, or TRAF5 may be part of the novel pathway that activates JNK and p38.

Overall, the results suggest (i) the existence of novel intermediary steps (e.g., missing cellular processes, proteins, or phosphorylation states) between extracellular poly (I:C) stimulation and intracellular TLR3 binding, and (ii) the presence of a novel pathway that is essential for JNK and p38 activation. Although the data strongly support that the prediction of novel intermediates upstream of TLR3 by the model is correct, what still remains to be seen is the characterization of the novel TRIF to MAP kinase pathways in poly (I:C) stimulation. Nevertheless, this chapter on TLR3 dynamics provides further evidence that the response of signaling molecules can be modeled through the perturbation-response approach, which can then be utilized to decipher novel signaling features of complex immune response.

References

1. Boehme KW, Compton T (2004) Innate sensing of viruses by Toll-like receptors. J Virol 78:7867–7873
2. Krishnan J, Selvarajoo K, Tsuchiya M, Lee G, Choi S (2007) Toll-like receptor signal transduction. Exp Mol Med 39:421–438
3. Gohda J, Matsumura T, Inoue J (2004) Cutting edge: TNFR-associated factor (TRAF) 6 is essential for MyD88-dependent pathway but not Toll/IL-1 receptor domain-containing adaptor-inducing IFN-beta (TRIF)-dependent pathway in TLR signaling. J Immunol 173:2913–2917

4. Chen NJ, Chio II, Lin WJ, Duncan G, Chau H, Katz D, Huang HL, Pike KA, Hao Z, Su YW, Yamamoto K, de Pooter RF, Zúñiga-Pflücker JC, Wakeham A, Yeh WC, Mak TW (2008) Beyond tumor necrosis factor receptor: TRADD signaling in Toll-like receptors. Proc Natl Acad Sci USA 105:12429–12434

5. Jiang Z, Mak TW, Sen G, Li X (2004) Toll-like receptor 3-mediated activation of NF-kappaB and IRF3 diverges at Toll-IL-1 receptor domain-containing adapter inducing IFN-beta. Proc Natl Acad Sci USA 101:3533–3538

6. Pobezinskaya YL, Kim YS, Choksi S, Morgan MJ, Li T, Liu C, Liu Z (2008) The function of TRADD in signaling through tumor necrosis factor receptor 1 and TRIF-dependent Toll-like receptors. Nat Immunol 9:1047–1054

7. Yamamoto M, Sato S, Hemmi H, Uematsu S, Hoshino K, Kaisho T, Takeuchi O, Takeda K, Akira S (2003) TRAM is specifically involved in the Toll-like receptor 4-mediated MyD88-independent signaling pathway. Nat Immunol 4:1144–1150

8. Hoebe K, Du X, Georgel P, Janssen E, Tabeta K, Kim SO, Goode J, Lin P, Mann N, Mudd S, Crozat K, Sovath S, Han J, Beutler B (2003) Identification of Lps2 as a key transducer of MyD88-independent TIR signalling. Nature 424:743–748

9. Helmy M, Gohda J, Inoue J, Tomita M, Tsuchiya M, Selvarajoo K (2009) Predicting novel features of Toll-like receptor 3 signaling in macrophages. PLoS One 4:e4661

10. Liu L, Botos I, Wang Y, Leonard JN, Shiloach J, Segal DM, Davies DR (2008) Structural basis of Toll-like receptor 3 signaling with double-stranded RNA. Science 320:379–381

11. Itoh K, Watanabe A, Funami K, Seya T, Matsumoto M (2008) The clathrin-mediated endocytic pathway participates in dsRNA-induced IFN-beta production. J Immunol 181:5522–5529

12. Carpenter S, Wochal P, Dunne A, O'Neill LA (2011) Toll-like receptor 3 (TLR3) signaling requires TLR4 Interactor with leucine-rich repeats (TRIL). J Biol Chem 286:38795–38804

13. Garcia-Cattaneo A, Gobert FX, Müller M, Toscano F, Flores M, Lescure A, Del Nery E, Benaroch P (2012) Cleavage of Toll-like receptor 3 by cathepsins B and H is essential for signaling. Proc Natl Acad Sci USA 109:9053–9058

14. Kato H, Takeuchi O, Sato S, Yoneyama M, Yamamoto M, Matsui K, Uematsu S, Jung A, Kawai T, Ishii KJ, Yamaguchi O, Otsu K, Tsujimura T, Koh CS, Reis e Sousa C, Matsuura Y, Fujita T, Akira S (2006) Differential roles of MDA5 and RIG-I helicases in the recognition of RNA viruses. Nature 441:101–105

15. Takeuchi O, Akira S (2008) MDA5/RIG-I and virus recognition. Curr Opin Immunol 20:17–22

16. Lamkanfi M, D'hondt K, Vande Walle L, van Gurp M, Denecker G, Demeulemeester J, Kalai M, Declercq W, Saelens X, Vandenabeele P (2005) A novel caspase-2 complex containing TRAF2 and RIP1. J Biol Chem 280:6923–6932

17. Oganesyan G, Saha SK, Guo B, He JQ, Shahangian A, Zarnegar B, Perry A, Cheng G (2006) Critical role of TRAF3 in the Toll-like receptor-dependent and -independent antiviral response. Nature 439:208–211

18. Su X, Li S, Meng M, Qian W, Xie W, Chen D, Zhai Z, Shu HB (2006) TNF receptor-associated factor-1 (TRAF1) negatively regulates Toll/IL-1 receptor domain-containing adaptor inducing IFN-beta (TRIF)-mediated signaling. Eur J Immunol 36:199–206

19. Miggin SM, O'Neill LA (2006) New insights into the regulation of TLR signaling. J Leukoc Biol 80:220–226

20. Meylan E, Burns K, Hofmann K, Blancheteau V, Martinon F, Kelliher M, Tschopp J (2004) RIP1 is an essential mediator of Toll-like receptor 3-induced NF-kappa B activation. Nat Immunol 5:503–507

21. Meylan E, Tschopp J (2005) The RIP kinases: crucial integrators of cellular stress. Trends Biochem Sci 30:151–159

Chapter 7
Understanding TNFR1 Signaling Dynamics

Tumor necrosis factor (TNF) is a major proinflammatory cytokine released by several proinflammatory pathways that activate transcription factors NF-κB and AP-1, such as the Toll-like receptors (TLRs), interleukin-1, Nod-like, and Fc receptors [1]. The detection of TNF and its role in anticancer activity, hence its name, was well known decades before the TLRs were discovered [2]. Today, this cytokine is known to regulate myriad critical cellular processes such as cell proliferation, differentiation, growth, proinflammatory response, and programmed cell death or apoptosis. Particularly, chronic aberration in the levels of baseline TNF in the human circulatory system has been attributed to the pathogenesis of numerous diseases, including rheumatoid arthritis, osteoporosis, sepsis, and cancer [3, 4].

TNF is a homotrimer containing 157 amino acids that binds to two types of outer membrane-bound receptors on target cells: TNFR1 and TNFR2. TNFR1, also called TNFRSF1A, is present in almost all cell types in humans, whereas TNFR2 is restricted to a few cell types. Both receptors trigger the cell survival and proinflammatory NF-κB and MAP kinases. However, TNFR1, after internalization through endocytosis, additionally triggers the cell death pathways via caspases. Furthermore, most of TNF-related biological processes are initiated by the death domain (DD) containing TNFR1.

TNFR1 trimerizes by TNF binding, and the intracellular DD of TNFR1 recruits TRADD, which then creates a platform for RIP1 and TRAF2 to collectively form the receptor signaling complex I (Fig. 7.1). Cellular inhibitor of apoptosis proteins (cIAP)-1 and -2 bind to complex I and, consequently, together with K63-linked ubiquitin chains modify RIP1 and TRAF2. This pathway creates docking sites for an E3 ligase or linear ubiquitin chain assembly complex (LUBAC) consisting of heme-oxidized IRP2 ubiquitin ligase-1 (HOIL-1), HOIL-1-interacting protein (HOIP), and SHANK-associated RH domain interacting protein (SHARPIN). Subsequently, the activation of TAK1 and the ubiquitination of NEMO (or IKKγ), a subunit of the IKK complex, leads to cell survival or proinflammatory response through NF-κB and AP-1 activation. Other TRAF superfamily members (TRAF5 and -6) are also known to play a role in NF-κB and MAP kinase activation [5].
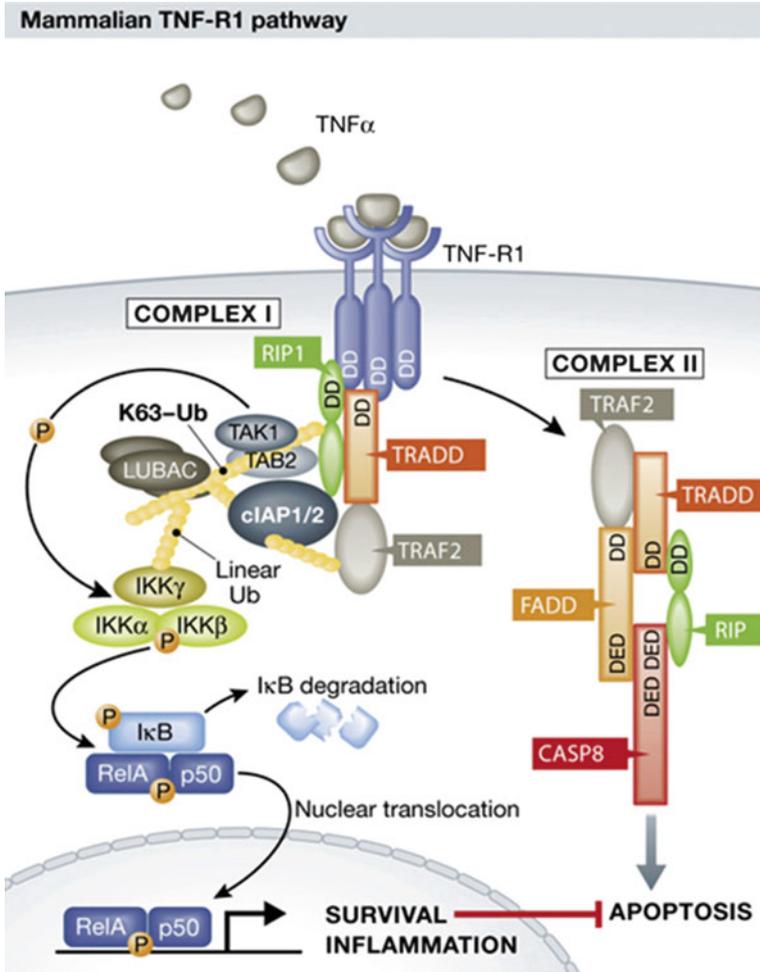
Fig. 7.1 *Schematic of tumor necrosis factor receptor (TNFR)1 signaling of cell survival/ proinflammatory and apoptosis pathways* (Adapted from Pobezinskaya et al. [6])

Consequently, clathrin, AP-2, and Dyn mediate receptor internalization. Receptor-signaling complex I becomes modified and dissociates from the TNFR1, allowing FADD and caspase-8 to form complex II. Within complex II, caspase-8 becomes activated to induce extrinsic apoptosis through caspase-3 activation. Alternatively, the TNF receptosome fuses with trans-Golgi vesicles to form multi-vesicular bodies (MVB). Caspase-8 activates caspase-7, within the MVB, which in turn induces A-SMase activation by cleavage of pro-A-SMase. Eventually, through cathepsin D, the cleavage of Bid to tBid in the mitochondria activates caspase-9, which then induces the intrinsic apoptosis through caspase-3 activation.

Because of its ability to signal numerous cellular processes via the survival and death pathways, TNFR1 signaling research has received immense attention over

recent years, especially on understanding the downstream signaling cascades to regulate and control proinflammatory diseases and cancer. Despite numerous studies, we are still at the infant stage in respect to disease treatment where TNF is overexpressed. More recent studies have generated high-throughput time-course data of intracellular signaling molecules. However, without appropriate theoretical and computational tools, it is a huge challenge to interpret the vital data. For example, what are the crucial molecular targets to downregulate proinflammatory response in rheumatoid arthritis? Although numerous genetic knockouts (KOs), such as TRAF2 KO and TRADD KO, have been generated to identify key proinflammatory mediators, the experimental outcomes are not very encouraging. For instance, in TRAF2 KO, there is compensatory activation of proinflammatory NF-κB through TRAF5 [5] or TRAF6 [7]. On the other hand, in TRADD KO, the result is almost complete abolition of NF-κB [8], which is not desirable for the general survivability of cells. Thus, we require a systemic approach where we can understand the flow of signal transduction to branching pathways during target intervention, so that an effective candidate target that overcomes and balances the deficiencies of current investigations can be elucidated.

In this chapter, TNFR1 signaling dynamics is analyzed for fibroblast cells by combining the perturbation-response modeling approach (Chap. 2) with experimental data generated for the temporal cell survival response. Starting from the current knowledge of TNFR1 signaling topology (Fig. 7.1), a computational model for the proinflammatory response leading to NF-κB and MAP kinase activations is developed. The experimental data for NF-κB (phosphorylation of IκBα) in the fibroblast cell type were obtained from a total of seven conditions (wild-type [5], TRAF2 KO [5], TRAF5 KO [5], TRAF2/TRAF5 double KO (DKO) [5], TRAF6 KO [7], TRADD KO [8], and RIP1KO [9]), and that for MAP kinase p38 in three available conditions (wild-type [7], TRAF6 KO [7], and TRADD KO [8]). Note that as the kinetics of JNK and ERK is similar to p38 in all experimental references, only p38 dynamics are shown in this chapter.

Simulations of TNFR1 Signaling Response

As with the TLRs pathways (see Chaps. 4, 5, and 6), each known reaction in TNFR1 signaling is represented by the first-order response equation, and the formation and depletion term parameter values are chosen to fit the semiquantitative experimental data of IκBα and p38 activations in wild-type condition, as a training set (Fig. 7.2a, WT). Here, only the cell survival process through complex 1 is the focus. In the next chapter on TRAIL signaling, both the cell survival and apoptosis pathways are investigated.

To finalize the TNFR1 model, the validity of the initial parameter set (elements of *J*) for wild-type is tested across various available KO conditions. In contrast to the TLR3 and TLR4 models, which required topological modifications to fit the model to experimental data, here the original topology alone is sufficient to successfully simulate IκBα phosphorylation and p38 kinase activation in all available
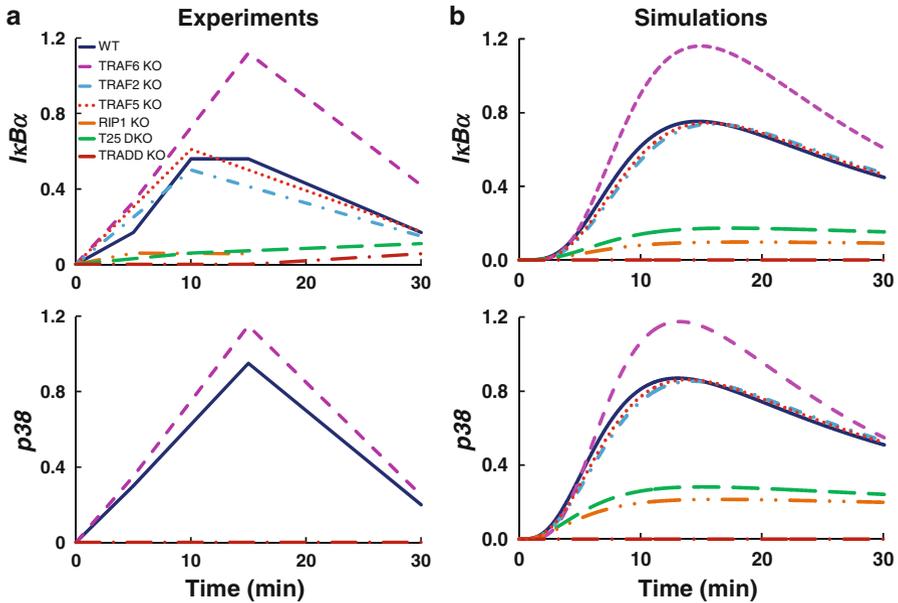
Fig. 7.2 *Temporal experimental activation and simulation profiles of IκBα and p38 in wild-type and mutant conditions.* Experimental murine embryonic fibroblasts (MEFs) generally treated with TNF (10 ng/ml) for the indicated time periods (**a**), and computational simulations (**b**), for IκBα phosphorylation (*top*) in wild-type (WT), TRAF2 knockout (KO), TRAF5 KO, TRAF2/TRAF5 double KO (T25 DKO), TRAF6 KO, TRADD KO, and RIP1 KO, and p38 activation (*bottom*) in WT, TRAF6 KO, and TRADD KO. Experimental details and actual data are found in references [5–9]. ImageJ was used to estimate relative intensities of activation dynamics for each molecule in each condition. RIP 1 KO experimental data are available only up to 15 min. The computational model equations and parameter values are given as Table 7.1

experimental conditions with reasonable accuracy (Fig. 7.2b, Table 7.1). In the wild-type, TRAF2 KO, TRAF5 KO, and TRAF6 KO, IκBα phosphorylation and p38 kinase activation reach peak around 15 min and gradually decay at 30 min. Notably, TRAF6 KO shows enhanced IκBα phosphorylation and p38 kinase activation as a consequence of signaling flux redistribution (*SFR*) (*response rule* 5, Box 4.2; Chap. 4). In the remaining conditions, the activation levels of both molecules are very weak (RIP1 KO and TRAF2/5 DKO) or absent (TRADD KO).

Analyzing TNF-Induced Gene Expression Patterns Reveals Novel Transcription Process

As shown in Fig. 7.2, the in silico TNFR1 model is able to reproduce experimental cell survival signaling dynamics over multiple (wild-type and various mutant) conditions. Next, the model is extended to investigate the proinflammatory gene expression dynamics.

Table 7.1 Tumor necrosis factor receptor (TNFR)1 model reactions and parameter values: the cell survival process

Number	Reaction	Formula	Parameter value (1/s)	Remarks
1	TNFRI → TRADD	k1* TNFRI	k1 = 0.005	TRADD is recruited to activated TNFR1
2	TRADD → cIAP	k2* TRADD	k2 = 0.02	cIAP1/2 binds to TRADD (complex 1 formation begins)
3	TRADD → TRAF6	k3*TRADD	k3 = 0.02	TRAF6 binds to TRADD
4	cIAP → TRAF2	k4*cIAP	k4 = 0.01	cIAP1/2 activates TRAF2
5	cIAP → TRAF5	k5* cIAP	k5 = 0.008	cIAP1/2 activates TRAF5
6	TRAF2 → RIP1	k6* TRAF2	k6 = 0. 001	cIAP1/2 activates RIP1 via TRAF2 with LUBAC
7	TRAF5 → RIP1	k7* TRAF5	k7 = 0.001	cIAP1/2 activates RIP1 via TRAF5 with LUBAC
8	TRAF6 → RIP1	k8*TRAF6	k8 = 0.0001	TRAF6 activates RIP1
9	TRAF6 → TAB/TAK	k9*TRAF6	k9 = 0.000125	TRAF6 activates TAB/TAK complex
10	RIP1 → LUBAC	k10*RIP1	k10 = 0.007	Ubiquitination of complex 1 by LUBAC
11	LUBAC → TAB/TAK	k11*LUBAC	k11 = 0.1	Activation of TAB/TAK complex via LUBAC
12	RIP1 → SHARPIN	k12* RIP1	k12 = 0.007	SHARPIN binds with complex 1 through RIP1
13	SHARPIN → IKKc	k13* SHARPIN	k13 = 0.1	Complex 1 through SHARPIN activates IKK complex
14	TAB/TAK → IKKc	k14* TAB/TAK	k14 = 0.1	TAB/TAK complex activates IKK complex
15	TAB/TAK → MKK1/2	k15* TAB/TAK	k15 = 0.00167	Activation of MAP kinases via TAB/TAK complex
16	TAB/TAK → MKK3/6	k16*TAB/TAK	k16 = 0.01	
17	TAB/TAK → MKK4/7	k17* TAB/TAK	k17 = 0.01	
18	MKK1/2 → ERK	k18*MKK1/2	k18 = 0.00167	Activation of ERK via MKK1/2
19	MKK3/6 → JNK	k19*MKK3/6	k19 = 0.00167	Activation of JNK via MKK3/6
20	MKK4/7 → p38	k20*MKK4/7	k20 = 0.1	Activation of p38 via MKK4/7
21	IKKc → IκBα	k21*IKKc	k21 = 0.01	Phosphorylation of IκBα by IKK complex

Table 7.1 (continued)

Number	Reaction	Formula	Parameter value (1/s)	Remarks
22	IκBα → NF-κBc	k22* IκBα	k22 = 0.008	Release of NF-κB via IκBα degradation
23	NF-κBc → NF-κBn	k23* NF-κBc	k23 = 0.0167	NF-κB translocates to the nucleus
24	p38 → p38n	k24* p38	k24 = 0.008	p38 translocates to the nucleus
25	JNK → JNKn	k25*JNK	k25 = 0.067	JNK translocate to the nucleus
26	ERKc → ERKn	k26* ERKc	k26 = 0.067	ERK translocate to the nucleus
27	ERKn → AP-1	k27* ERKn	k27 = 0.00567	ERK activates AP1
28	JNKn → AP-1	k28* JNKn	k28 = 0.00567	JNK activates AP1
29	p38n → AP-1	k29* p38n	k29 = 0.05	p38 activates AP1
30	AP1 → APNFG1	k30* AP1	k30 = 0.5	AP1 binds to G1 gene promoter
31	AP1 → APNFG2	k31* AP1	k31 = 0.007	AP1 binds to G2 gene promoter
32	AP1 → APNFG3	k32* AP1	k32 = 0.007	AP1 binds to G3 gene promoter
33	NF-κBn → APNFG1	k33* NF-κBn	k33 = 0.045	NF-κB binds to G1 gene promoter
34	NF-κBn → APNFG2	k34* NF-κBn	k34 = 0.01	NF-κB binds to G2 gene promoter
35	NF-κBn → APNFG3	k35* NF-κBn	k35 = 0.02	NF-κB binds to G3 gene promoter
36	APNFG1 → ANG1	k36* APNFG1	k36 = 0.1	Delay process 1 to G1 gene transcription
37	ANG1 → G1	k37* ANG1	k37 = 0.7	G1 gene transcription
38	G1 → G1deg	k38*G1	k38 = 0.0011	G1 decay
39	APNFG2 → ANG2	k39* APNFG2	k39 = 0.001	Delay process 1 to G2 gene transcription
40	ANG2 → ANG21	k40* ANG2	k40 = 0.003	Delay process 2 to G2 gene transcription
41	ANG21 → G2	k41* ANG21	k41 = 0.007	G2 gene transcription
42	G2 → G2deg	k42*G2	k42 = 0.00001	G2 decay
43	APNFG3 → ANG3	k43* APNFG3	k43 = 0.0003	Delay process 1 to G3gene transcription
44	ANG3 → ANG31	k44* ANG3	k44 = 0.00004	Delay process 2 to G3 gene transcription
45	ANG31 → ANG32	k45* ANG31	k45 = 0.000167	Delay process 3 to G3 gene transcription
46	ANG32 → G3	k46* ANG21	k46 = 0.00167	G3 gene transcription
47	G3 → G3deg	k47*G2	k47 = 0.00009	G3 decay
48	NF-κBn → X1	k48* NF-κBn	k48 = 0.07	NF-κB activates novel molecule X1

Table 7.1 (continued)

Number	Reaction	Formula	Parameter value (1/s)	Remarks
49	AP-1 → X1	k49* AP-1	k49 = 0.08	AP-1 activates novel molecule X1
50	X1 → *X2*	k50* X1	k50 = 0.0002	X1 activates novel molecule *X2*
51	*X2* → X3	k51* *X2*	k51 = 0.0001	*X2* activates novel molecule X3
52	X3 → X4	k52* X3	k52 = 0.001	X3 activates novel molecule X4
53	X4 → APNFG1	k53* X1	k53 = 0.00001	X4 binds on G1 promoter
54	X4 → APNFG3	k54* X1	k54 = 0.0001	X4 binds on G3 promoter

Note that 1 mol or 6.023×10^{23} molecules of TNF pulse is used to stimulate the model. The simulation plot of each molecule is finally normalized to its wild-type peak value

Recently, time-series high-throughput (microarray) and quantitative real-time polymerase chain reaction (PCR) experiments on TNF-simulated HeLa and mouse fibroblast cells revealed three distinct groups of gene expression patterns, with possibly corresponding distinct biological roles [10, 11]. The groups were labeled as "early I," "middle II," and "late III" response, peaking between 0.5–1, 2–3, and 6–12 h after TNF stimulation, respectively (Fig. 7.3a, b).

In particular, the mechanistic reasons for the distinct temporal profiles have been attributed mainly to the differential regulation of the decay process of gene (mRNA) expressions by miRNA targeting the AU rich element (ARE) region on the 3′-UTR [11]. This hypothesis corresponded with the lesser ARE regions (causing lower decay) found in actual cells for group III genes, compared with groups I and II [11]. Thus, for group I genes the decay is fast, for group II genes the decay is slow, and for group III genes the decay rate is very low compared to its transcription rate.

To test the TNFR1 model for predictive capacity of gene expression and to investigate the postulation of simple miRNA decay mechanisms for explaining distinct gene expressions, the model was extended to simulate the dynamic profiles of gene expression. In the model, the decay process is represented by a depletion or deactivation term; that is, the overall decay term collectively represents mRNA instabilities, deadenylase, and miRNA regulation. The formation term is represented by the transcription process.

From *response rule 1* (Chap. 4, Box 4.2), the time for gene activation can be controlled. That is, adding intermediates between transcription process and gene induction will increase delay for gene expression dynamics. The intermediates can represent the complexities of transcription process involving the preinitiation, initiation, promoter clearance, elongation, and termination [12].

Using this technique, the TNFR1 model simulations are able to generally fit the temporal dynamics of group I and II genes; however, they will not fit for group III
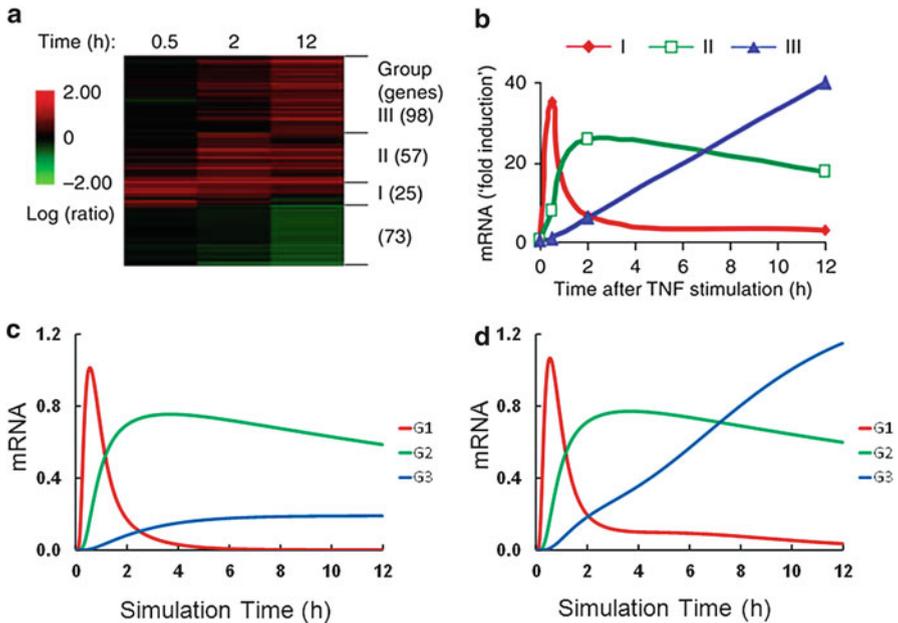
Fig. 7.3 *Three distinct groups of TNF-activated genes*. (**a**) Microarray analysis of gene expression in 3 T3 fibroblasts stimulated for 0.5, 2, or 12 h with recombinant mouse TNF. *Red*, activated genes; *green*, genes suppressed by TNF treatment. Numbers in *parentheses* (*right margin*) indicate the number of genes in each group. (**b**) Expression profiles of genes in groups I, II, and III. Curves are representative of two to six experiments [11]. Simulation profiles of the three group of genes using original TNFR1 model (**c**) and modified model B (**d**) which contains novel feedback mechanisms (see Fig. 7.4)

genes (Fig. 7.3c). According to the model, reducing the parameter value for decay term (to represent the lower miRNA regulating decay process) alone is not sufficient to produce continuous activation of group III genes; it leads to an initial increase followed by stabilization of the profile (steady state).

Additional signaling flux that provides continuous activation of group III genes can be generated by a novel pathway (transcription process) from *response rules 3 and 9* (Chap. 4, Box 4.2): this could result from secondary posttranscriptional/translational mechanisms through (i) autocrine signaling such as interleukin (IL)-6 [13] or transforming growth factor (TGF)-β [14] signaling, or (ii) cytosolic feedback mechanisms specifically for group III genes (Fig. 7.4).

Thus, to overcome the shortfall in the model simulations, novel signaling flux predominantly affecting the transcription of group III genes is next included (model B). Notably, the resultant simulations fit the three groups of gene dynamic profiles reasonably well (Fig. 7.3b, d). These data, therefore, suggest that low miRNA regulation of group III genes alone is insufficient to produce the continuous activation of group III genes and requires a novel transcription process, possibly through secondary posttranscriptional/translational autocrine signaling, such IL-6 or TGF-β signaling or feedback mechanisms.
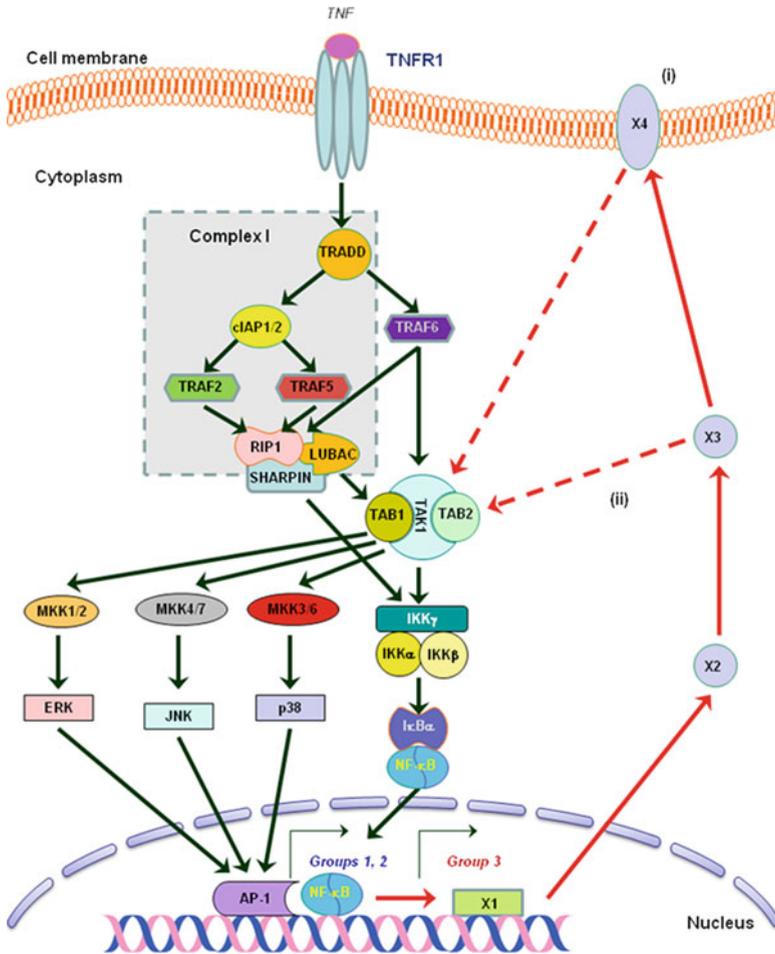
Fig. 7.4 *Schematic of predicted novel feedback mechanism.* Proposed novel pathway to provide additional signaling flux (*red arrows*). The novel mechanisms could occur as a result from the translation of gene groups I, II, and III into proteins for (i) autocrine signaling or (ii) cytosolic feedback fluxes

Predicting Novel Target for Regulating Proinflammatory Response

Now that the TNFR1 model B is able to successfully simulate the three groups of upregulated genes in the wild-type, next, the significance and effect of in silico KO of key intracellular signaling molecules is investigated. It is well known that the TNFR1 signaling is enhanced in proinflammatory diseases and cancer [1–4]. To investigate which known molecules would be a potential target to regulate the
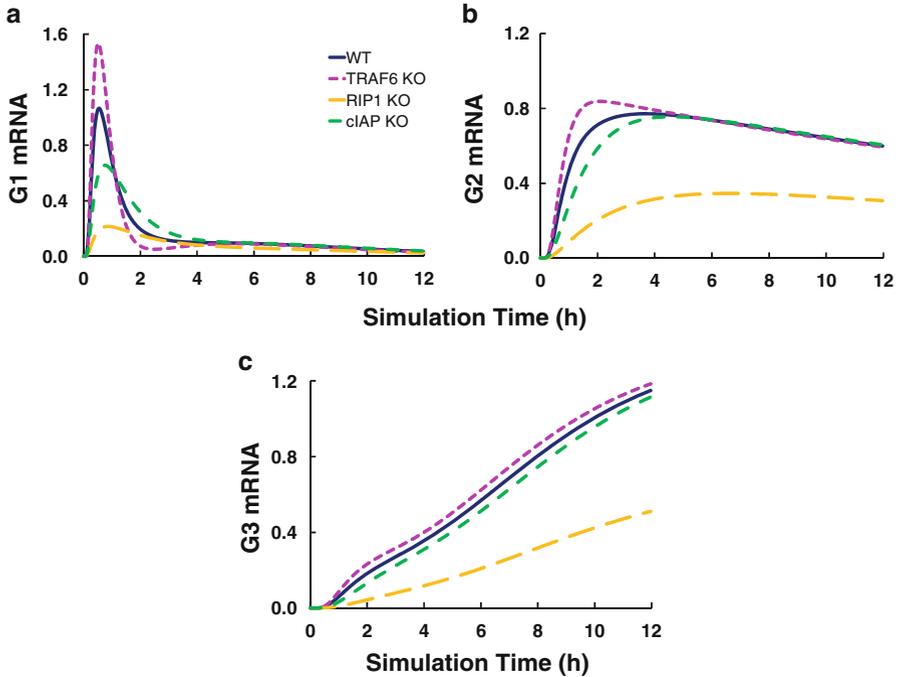
Fig. 7.5 *In silico KO effects on the three groups of genes.* Simulation profiles of modified TNFR1 model B for the three groups of genes: group I (**a**), group II (**b**), and group III (**c**), in four experimental conditions: wild-type (*blue*), TRAF6 KO (*pink*), RIP1 KO (*yellow*), and cIAP1/2 KO (*green*)

cell survival or proinflammatory activity, the TNFR1 model is tested in specific in silico mutant conditions. Because TRAF-2 and -5 KOs have little effect compared to wild-type, and TRADD KO abolishes almost all activity of IκBα and p38 (Fig. 7.2a), these molecules will not be suitable targets for regulating downstream gene expressions in a desirable manner (as their removal would either produce little effect or significantly stall cell survival activities crucial for normal functioning).

On the other hand, it will be interesting to investigate the effect of TRAF6 and RIP1 KOs, which enhances and suppresses IκBα and p38 activity, respectively. In addition, because cIAP1/2 also plays a key role in complex I and experimental data are currently lacking, the effect of removing these molecules is also tested. Hence, in silico TRAF6 KO, RIP1 KO, and cIAP KO are performed.

Figure 7.5 shows the simulations of group (G) I, II, and III genes, which are mostly well-known proinflammatory mediators. From the simulations, RIP1 KO produced the most noticeable downregulation, and yet maintained certain activity, of all three gene groups. This result, thus, suggests that RIP1 may be a crucial single molecule target for controlling enhanced proinflammatory response caused by TNFR1 signaling in disease conditions, such as in rheumatoid arthritis.

In summary, to understand the temporal activation profiles of the TNF-regulated signaling network (a cytokine produced during the innate immune response to

invading pathogens and involved in numerous fundamental cellular processes), a dynamic computational model based on perturbation-response approach and the law of information (signaling flux) conservation is developed. The temporal activation dynamics of transcription factor NF-κB, MAP kinase p38, and three groups of genes (representing 180 upregulated genes in mouse fibroblasts) to TNF stimulation were investigated. Despite the simplicity of using first-order response equations to simulate the profiles of the intracellular molecules, the computational model recapitulated the experimental response in the wild-type and several mutant conditions. This result is surprising as it is generally envisioned that the innate immune response of TNF is highly complex.

From analyzing the downstream temporal gene expression profiles, the model suggests that the presence of additional novel posttranscriptional/translational processes is required for the continuous activation of group III genes, in contrast to previous postulation, where it is believed that the continuous activation is caused by a lesser ARE region for those genes, leading to a very low decay process. A literature survey indicated that the novel posttranscriptional/translational process could be provided by secondary signaling features such as autocrine signaling through IL-6 and TGF-β, or perhaps derives from feedback mechanisms regulating the novel promoter regions of group III genes. For example, the role of the interferon transcription factor (IRF) family in inducing *Ccl5* or RANTES expression, which belongs to one of the group III genes, is reported in a previous study [15]; however, it is not currently considered in the current model. It is, therefore, necessary to perform further experimental work to confirm and elucidate the exact mechanisms for the continuous activation of group III genes.

Finally, for downregulating TNF signaling, which is enhanced in proinflammatory diseases and cancer, the in silico investigation of the gene expression dynamics of the three groups of genes suggests that RIP1 may potentially become an important therapeutic target. This chapter adds further evidence for the presence of a simple linear average response governing the early primary signaling process through immune-related cell survival pathways.

References

1. Newton K, Dixit VM (2012) Signaling in innate immunity and inflammation. Cold Spring Harbor Perspect Biol 4:1–19
2. Locksley RM, Killeen N, Lenardo MJ (2001) The TNF and TNF receptor superfamilies: integrating mammalian biology. Cell 104:487–501
3. Bradley JR (2008) TNF-mediated inflammatory disease. J Pathol 214:149–160
4. van Horssen R, Ten Hagen TL, Eggermont AM (2006) TNF-alpha in cancer treatment: molecular insights, antitumor effects, and clinical utility. Oncologist 4:397–408
5. Tada K, Okazaki T, Sakon S, Kobarai T, Kurosawa K, Yamaoka S, Hashimoto H, Mak TW, Yagita H, Okumura K, Yeh WC, Nakano H (2001) Critical roles of TRAF2 and TRAF5 in tumor necrosis factor-induced NF-κB activation protection from cell death. J Biol Chem 276:36530–36534
6. Falschlehner C, Boutros M (2012) Innate immunity: regulation of caspases by IAP-dependent ubiquitylation. EMBO J 31:2750–2752

 7. Funakoshi-Tago M, Kamada N, Shimizu T, Hashiguchi Y, Tago K, Sonoda Y, Kasahara T (2009) TRAF6 negatively regulates TNF-alpha-induced NF-kappa-B activation. Cytokine 45:72–79

 8. Ermolaeva MA, Michallet MC, Papadopoulou N, Utermöhlen O, Kranidioti K, Kollias G, Tschopp J, Pasparakis M (2008) Function of TRADD in tumor necrosis factor receptor 1 signaling and in TRIF-dependent inflammatory responses. Nat Immunol 9:1037–1046

 9. Devin A, Cook A, Lin Y, Rodriguez Y, Kelliher M, Liu Z (2000) The distinct roles of TRAF2 and RIP in IKK activation by TNF-R1: TRAF2 recruits IKK to TNF-R1 while RIP mediates IKK activation. Immunity 12:419–429

10. Tian B, Nowak DE, Brasier AR (2005) A TNF-induced gene expression program under oscillatory NF-kappa-B control. BMC Genomics 6:137

11. Hao S, Baltimore D (2009) The stability of mRNA influences the temporal order of the induction of genes encoding inflammatory molecules. Nat Immunol 10:281–288

12. Solomon EP, Berg LR, Martin DW (2011) Biology, 9th edn. Thomson Brooks/Cole, Belmont

13. Grivennikov S, Karin M (2008) Autocrine IL-6 signaling: a key event in tumorigenesis? Cancer Cell 13:7–9

14. Ihn H (2008) Autocrine TGF-beta signaling in the pathogenesis of systemic sclerosis. J Dermatol Sci 49:103–113

15. Liu J, Ma X (2006) Interferon regulatory factor 8 regulates RANTES gene transcription in cooperation with interferon regulatory factor-1, NF-kappa-B, and PU.1. J Biol Chem 281: 19188–19195

Chapter 8
TRAIL Signaling in Cancer

Cancer tissues are often found to contain immune cells in their vicinity, which naturally leads to the question of a relationship between immune cells and tumors and whether the former actually help or suppress cancer progression. Numerous studies have now shown evidence for both scenarios. Lately, however, the ability of our immune response to induce apoptosis, or programmed cell death, in cancer cells and so to fight against disease progression is gaining momentum [1, 2]. Among the many immune factors found within the tumor microenvironment, the tumor necrosis factor (TNF) family members are noted for their ability to induce cellular apoptosis, in addition to typical proinflammatory response. In particular, the TNF-related apoptosis ligand (TRAIL), also known as Apo-2 ligand and TNFSF10, has received primal attention as these are capable of recognizing and inducing apoptosis of tumors and metastases while leaving normal cells mostly unaffected.

TRAIL is prevalently found as endogenous in several types of immune cells (e.g., macrophages, natural killer cells, T cells), and its expression can be elevated in these cells by infected agents, such as through the Toll-like receptor and the interferon-γ signaling pathways. TRAIL is known to bind with TRAIL-R1 [or death receptor (DR) 4], TRAIL-R2 (or DR5), TRAIL-R3 [or decoy receptor (DcR) 1], TRAIL-R4 (or DcR2), and osteoprotegerin. Notably, TRAIL-R1 and TRAIL-R2 possess intracellular death domains and, subsequently, have the ability to mediate TRAIL-induced apoptosis. The remaining receptors are decoys that compete for TRAIL, thereby possibly negatively regulating the effects of TRAIL-R1 and TRAIL-R2 signaling.

The immune defense role of TRAIL has been shown to kill pathogen-infected or malignant cells [3]. Notably, increased expressions of TRAIL-R1 and -R2 have been found on extracellular membranes of several kinds of tumor cells with corresponding increases in apoptosis compared with normal cells. Deficiency of TRAIL-R1 and -R2 has also led to malignancy. Further investigations using TRAIL-induced apoptosis for effective control of cancer proliferation have yielded successes at preclinical settings for certain cancer cells. In the majority of cases, such as melanoma and neuroblastoma, however, TRAIL stimulation has little or no effect.

The nonsensitivity of TRAIL-stimulated cancers occurs as a result of several factors including very low expression levels of TRAIL-R1 and -R2, increased levels of DcR1 and DcR2, and elevated levels of negative regulators of apoptosis such as cFLIP, etc. In addition, the upregulation of cell survival and proliferation pathways through MAP kinases and NF-κB activations are crucial for resistance.

More recently, to overcome resistance, TRAIL has been used in conjunction with other treatment strategies. Several studies have constructed combination therapies with proteasome inhibitors, histone deacetylase inhibitors, ionizing radiation, etc., for enhancing apoptosis [4, 5]. Specific intracellular targets, such as tyrosine kinase inhibitors and IκBα suppressors, have also been used to show reduced survival of cancer cells [6, 7]. These studies have focused on a single mode of action by targeting either survival or apoptotic pathways. However, as cancers are known to show high activities of both survival and apoptotic pathways, it remains unclear whether the suppression of survival or the enhancement of apoptosis, independently, will yield optimal results. The clinical results so far have perhaps shown only partial response in most cases, asking for a deeper understanding of the synergistic effect of combinatorial treatments [8]. Thus, clear mechanistic insights into the conflicting roles of the cell survival and apoptotic pathways triggered by TRAIL are required. For example, when are cell survival and apoptotic pathways activated? Do they regulate each other? Are they induced at different time points? Finding answers to these questions may likely provide an improved strategy to treat cancers using TRAIL.

So, in spite of numerous studies targeting TRAIL resistance, we are still far from successfully understanding and controlling the mechanisms for resistance. Another possible reason may lie in the way intracellular data are generated, analyzed, and interpreted. For example, many studies use single time-point readout of survival or apoptotic molecules to compare treated with untreated cancer cells. Although such data provide qualitative snapshot information of cancer cell response to the treatments, they may not necessarily show the overall effectiveness in time. For example, in lipopolysaccharide-stimulated macrophages, upregulated molecules (based on mRNA expression) at early time points can become downregulated at later time points [9]. Thus, it is important to rigorously analyze the temporal data generated by TRAIL-stimulated experiments using systems biology approaches.

In this chapter, to shed light on the resistance mechanisms and to identify an effective intracellular target for TRAIL-resistant human fibrosarcoma (HT1080), the perturbation-response approach has been once again used to model the activation dynamics of key cell survival (IκB, JNK, p38) and apoptotic (caspase-8, -3) signaling molecules. As shown in the preceding chapters, the model does not require the full knowledge of all signaling species and their reaction kinetics. Using the approach of comparing experimental data with model simulations, first, novel pathway features for TRAIL signaling in HT1080 cells are uncovered. Second, by developing a theoretical cell survival metric (*CSM*), the net effects of cancer cell survival and apoptosis under various intracellular mutations are evaluated. Finally, using the computational model together with *CSM*, an optimal target for overcoming TRAIL resistance is predicted.

Dynamic Model for TRAIL-Stimulated HT1080 Cell Population Response

Previous experimental work on HT1080 cells has shown that TRAIL stimulation not only activates the apoptotic pathways (caspases), but also displays cell survival activities through NF-κB and MAPKs, resulting in overt resistance to death [10]. However, systemic understanding of the counterbalancing survival and death mechanisms remains unclear. For developing effective strategies to control TRAIL-resistant cancer cells, a mechanistic understanding of the temporal activations of the cell survival and apoptosis pathways is required.

To investigate the dynamic activations of cell survival (NF-κB, MAPKs) and apoptosis (caspases) in TRAIL-resistant HT1080 cells, a computational model of TRAIL signaling is developed. The original model uses the widely accepted TRAIL signaling topology: upon ligation of TRAIL, TRAIL-R1 (DR4), and TRAIL-R2 (DR5) form receptor clusters facilitated by *O*-glycosylation and/or palmitoylation. This step allows the intracellular death domain of TRAIL-R1 and -R2 to recruit FADD, caspase-8, and cFLIP, collectively called the primary death-inducing signaling complex (DISC). Still attached to the membrane, the DISC becomes enriched in lipid rafts, subsequently allowing caspase-8 to interact with CUL3/RbxI-based E3 ligase complex. Polyubiquitylation of caspase-8 occurs, and the ubiquitin-binding protein p62/sequestosome-1 binds with caspase-8 to detach it from the DISC. Consequently, caspase-8 interacts with RIP1, TRAF2, and IKK-γ to form secondary DISC, which activates downstream NF-κB, MAPKs, and caspase-3, a member of the cysteinyl-aspartate-specific proteases, through the extrinsic pathways (Fig. 8.1).

To develop and analyze the TRAIL model, the static TRAIL topology was converted into a perturbation-response model where each species is connected to another by first-order response equations, and the parameters were chosen from temporal experimental data (see Chap. 2 for computational modeling details). Time-course experimental data [10] of IκB, JNK, p38, and caspase-8 and -3 in wild-type, RIP1 KD, FADD KD, caspase-8 KD, and TRAF2 KD of HT1080 cells with 1,000 ng/ml TRAIL stimulation is utilized. The activation levels of IκB, JNK, p38, and caspase-8 and -3 were quantified from the Western blot data using ImageJ, and normalized according to the peak values in the wild-type for each molecule (Fig. 8.2).

With the aid of a genetic algorithm, the model parameters were fitted with the available experimental profiles in wild-type. Once the simulations for all tested molecules fit reasonably well in the wild-type, the validity of the parameter values were tested in other mutant conditions (RIP1 KD, FADD KD, etc.). If the simulations are not satisfactory in any experimental condition (based on the area between the experimental profiles and simulations curves; see Chap. 4), the current TRAIL topology will be modified according to the *response rules* (Box 4.2, Chap. 4). For example, in wild-type, if a time delay is observed in the experimental activation onset compared with simulation, then according to *response rule 1*, additional intermediary first-order terms are added to provide delay. The process of modifying the TRAIL
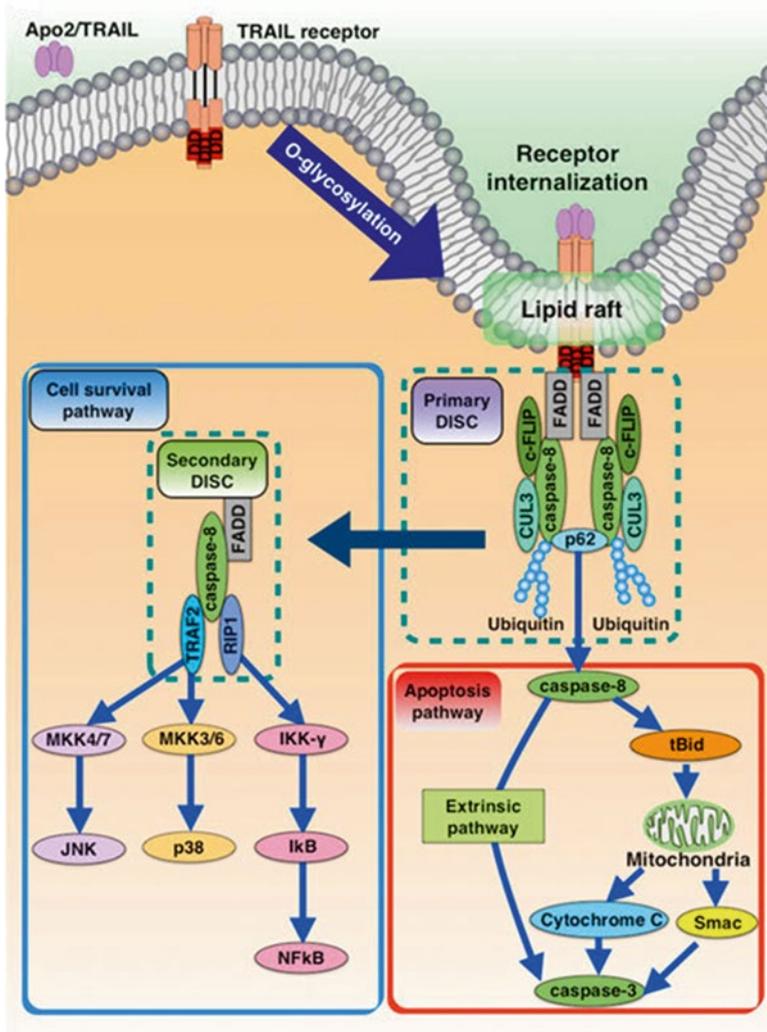
Fig. 8.1 *Schematic topology of the tumor necrosis factor (TNF)-related apoptosis ligand (TRAIL) signaling pathway* (Adapted from Piras et al. [11])

topology and parameter values for each molecule and in each condition is done iteratively until all tested molecules are able to successfully reproduce experimental data in all tested conditions (see Fig. 4.3, Chap. 4).

Overall, five experimental conditions (wild-type, RIP1 KD, FADD KD, caspase-8 KD, and TRAF2 KD) are utilized to generate a single robust model that simulates five molecules (IκB, JNK, p38, caspase-8 and -3) over five measured time points (0, 10, 30, 60, and 120 min) for TRAIL-stimulated HT1080 cells (Fig. 8.2).

Fig. 8.2 *TRAIL signaling response*. Experimental activation profiles of p38, IκB, JNK, caspase-8, and caspase-3 in wild-type, RIP1 KD*, FADD KD*, caspase-8 KD*, and TRAF2 KD in arbitrary units (a.u.) at $t=0$, 10, 30, 60**, and 120 min after TRAIL stimulation of HT1080 cells. Original source was obtained from Figure 3a of Varfolomeev et al. [10] and was processed through ImageJ. *Data unavailable for caspase-8 and -3; **data available for caspase-8 and -3 only. Note: Interpolated *dotted lines* between experimental data points are inserted as a guide; they might not represent the actual temporal dynamics (Adapted from Piras et al. [11])
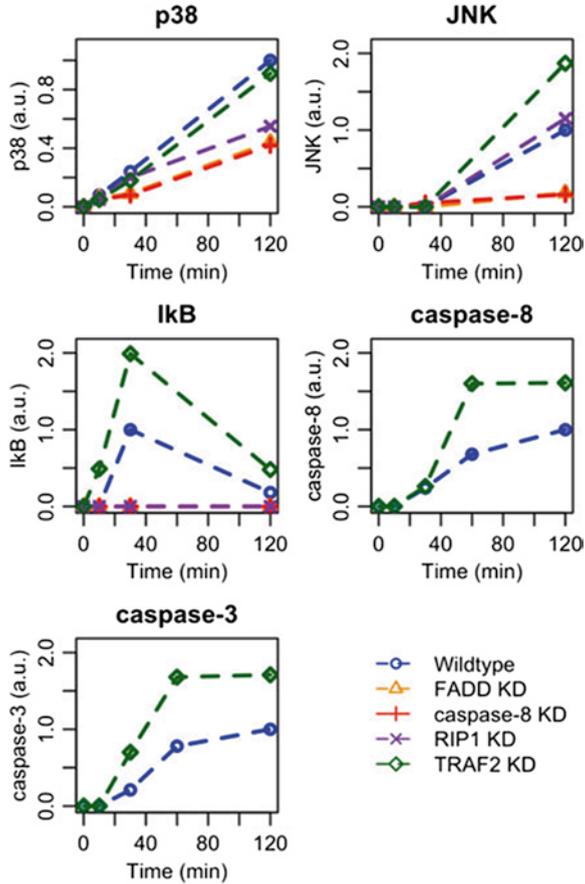
Simulations of Initial TRAIL Signaling Model

Several parameter sets of the initial model (Fig. 8.3a) are examined so that the resultant simulations could match the experimental profiles in wild-type. Apart for p38, where experiments showed rapid activation in comparison to model simulation, the IκB, JNK, and caspase-8 and -3 simulations successfully fit with their respective experimental profiles (Fig. 8.3b; wild-type).

Next, the initial model simulations are compared for other mutant conditions (RIP1 KD, FADD KD, caspase-8 KD, and TRAF2 KD). Although IκB, caspase-8, and caspase-3 simulations recapitulated experiments in all conditions, the simulations of p38 and JNK activations are not satisfactory (Fig. 8.3b). Experimental RIP1 KD showed impaired activation of p38 compared to wild-type; however, in silico RIP1 KD simulation shows similar levels to wild-type at 120 min (Fig. 8.3b; RIP1 KD). Furthermore, in contrast to experiments, RIP1 KD simulation produces delayed p38 activation, similarly to wild-type simulation.
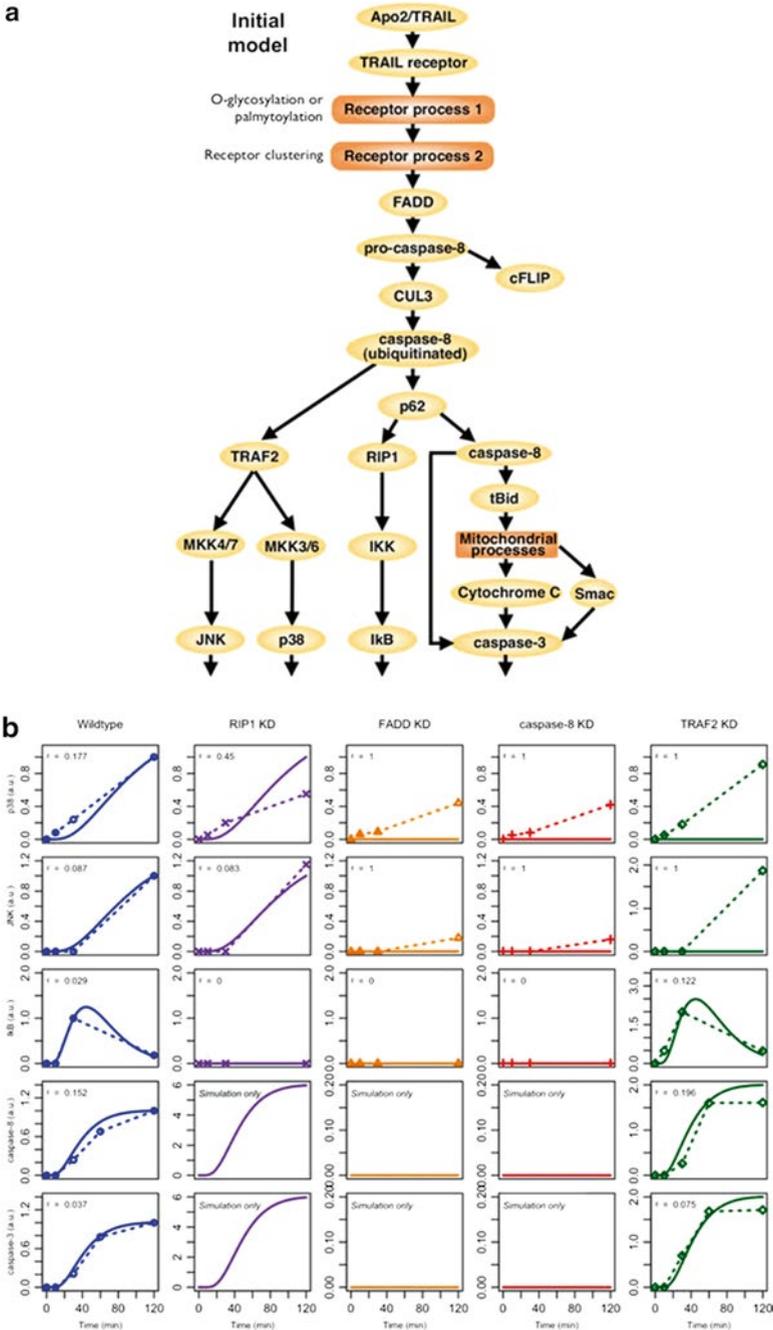
Fig. 8.3 *Simulation of initial TRAIL signaling model*. (**a**) Static topology of the TRAIL signaling pathway used for developing our computational model. Note that we lump the similar effects of DR4/5 as TRAILR1/2, and ignore the response of DcR1/R2/OPG. Also, note that we include molecular conditions such as receptor clustering as additional first-order terms. (**b**) Comparison of simulations (*solid lines*) with experimental data (*dotted lines*) in wild-type, RIP1 KD, FADD KD, caspase-8 KD*, and TRAF2 KD in arbitrary units (a.u.). *Caspase-8 KD also refers to pro-caspase-8 KD (Adapted from Piras et al. [11])

For FADD, caspase-8, and TRAF2 KDs, in contrast to experimental profiles, the simulations failed to show any p38 or JNK activation (Fig. 8.3b). Collectively, the TRAIL model developed using the current topology reasonably simulates IκB, caspase-8 and -3 temporal activation profiles in all KD conditions; however, it fails to capture the dynamics of p38 and JNK.

Revealing Novel Features of TRAIL Signaling

To overcome the shortfall of the model simulations adopting current TRAIL topology, the *response rules* (Box 4.2; Chap. 4) are utilized to modify the network to investigate whether the model simulations could be improved, especially for p38 and JNK profiles.

Investigating p38 Dynamics

In wild-type and RIP1 KD, p38 is experimentally activated within 10 min after TRAIL stimulation, whereas in model simulations it takes at least 20 min (Figs. 8.3b, 8.4a). According to *response rule 2*, the introduction of a novel bypass pathway to activate p38 more directly and specifically, perhaps not involving the primary or secondary DISC, will produce rapid activation. Thus, the initial model (M0) is modified by adding a novel bypass from receptor process 1 to MKK3/6, and this resulted in a good match between simulations, not only for wild-type data but also for FADD and caspase-8 KDs (Fig. 8.4b; M1). Note that the novel bypass is not sensitive to whether the origin starts from TRAIL-R1 or the receptor process terms. However, adding a bypass at or downstream of FADD incurs noticeable delay in p38 activation (data not shown). Hence, this novel bypass is termed the FADD-independent pathway.

Although the delayed simulations are finished by inserting a novel FADD-independent pathway, for RIP1 KD, the late-phase peak activation (at 120 min) is enhanced in M1 simulations, and for TRAF2 KD, the p38 activation is still under-predicted at 120 min (Fig. 8.4b; M1 yellow area). From RIP1 KD data, *response rule 5ii* indicates a possible link between RIP1 and p38, so that the removal of RIP1 will negatively affect p38 activation. Notably, the inclusion of this feature alone in a modified model was sufficient to reasonably match experimental and simulation results for both RIP1 KD and TRAF2 KD (Fig. 8.4c; M2).

Investigating JNK Dynamics

Using the updated model (M2), JNK dynamics is next investigated. This time, the JNK simulation for wild-type and RIP1 KD is quicker than experimental profiles (Fig. 8.4d). Hence, according to *response rule 1*, additional novel intermediates
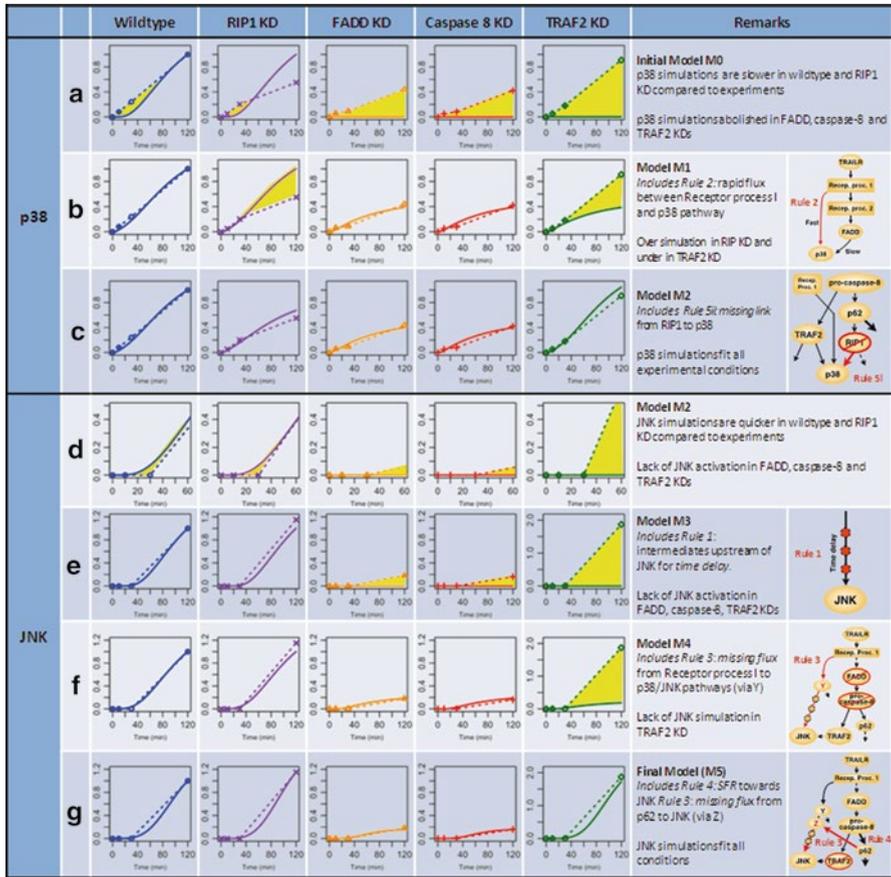
Fig. 8.4 *Revealing novel features of TRAIL signaling using modeling strategy and response rules* comparing model simulations with experiment results. For p38: M0, the initial model (**a**), M1 (**b**), with the addition of a rapid bypass, and M2 (**c**), with the addition of a missing link between RIP1 and p38 pathway. For JNK: M2 (**d**), M3 (**e**), with intermediates to introduce delay in activation, M4 (**f**), with a missing link for the activation of JNK in FADD and caspase-8 KDs, and M5 (**g**), a missing link between p62 and JNK pathway to show enhancement through *SFR* in TRAF2 KD (Adapted from Piras et al. [11])

(proteins, complex formation, etc.) specific to JNK are added to provide certain delay in activation. As expected, this improved JNK simulations for wild-type and RIP1 KD (Fig. 8.4e; M3). However, JNK simulations for FADD, caspase-8 and TRAF2 KDs were still absent and did not match experimental results. Utilizing *response rule 3* (missing flux), a link from the predicted FADD-independent pathway for p38 to also activate JNK is added. Thus, a novel molecule *Y* was introduced to branch from receptor process 1 to p38 and JNK, and the other novel intermediates (predicted by M3) are specifically inserted between *Y* and JNK via MKK4/6 (Fig. 8.4f).

This procedure resulted in significant improvement in the JNK simulations in wild-type, RIP1 KD, FADD KD, and caspase-8 KD, but not in TRAF2 KD (Fig. 8.4f; M4). To achieve specific activation of JNK in TRAF2 KD, we require a bypass from p62 to novel molecule Z (one of the novel intermediates predicted above) on the FADD-independent pathway to activate JNK (*response rules 3* and *4*; Fig. 8.4g). Overall these modifications to the initial model, based on response rules, remarkably recapitulate IκB, p38, JNK, and caspase-8 and -3 activations in all tested experimental conditions (wild-type, RIP1 KD, FADD KD, caspase-8 KD, and TRAF2 KD) with a good degree of consistency (Fig. 8.5, Table 8.1).

To evaluate the relative significance of each novel pathway branch, *response rule 6* was utilized. By quantifying signaling flux for each pathway branch, the FADD-independent pathway is estimated to contribute about 17 % and 43% of total JNK and p38 activations, respectively, and the RIP1 to p38 crosstalk provides about 45 % flux for p38 activation. The bypass from p62 to molecule Z provides about 82 % flux to JNK, whereas TRAF2 provides about 1 % flux to JNK, and the TRAF2 to MKK3/6 axis provides about 12% flux to p38. Thus, RIP1 is key for p38 and Z is crucial for JNK activation.

In summary, (i) a FADD-independent pathway to activate p38 and JNK, bypassing the primary and secondary DISC and through novel molecules Y and Z, (ii) a crosstalk between RIP1 and p38 via MKK3/6, (iii) a crosstalk between p62 and JNK via molecule Z, and (iv) intermediary step(s) or molecule(s) upstream of JNK, are proposed (Fig. 8.5b).

Identifying In Silico Targets for Enhancing Cancer Cell Death

Now that a robust model, consistent in wild-type and several mutant conditions, for TRAIL signaling in HT1080 cell populations has been developed, can this model be used to identify a promising target for overcoming TRAIL resistance? Also, what are the roles of the novel predicted molecules, Y and Z, in the survival and apoptosis activities? Can either of these molecules potentially be a crucial target for enhancing cancer cell death in TRAIL therapy?

To address these issues, in silico KDs of Y and Z molecules are next performed to investigate p38, JNK, IκB, and caspase-8 and -3 dynamics (Fig. 8.6). In silico Y KD produced about 25 % fall in p38 activation, almost unchanged JNK, and a slight enhancement of IκB and caspases activities through signaling flux redistribution (*SFR*). The in silico Z KD, however, showed more pronounced effects: complete abolition of JNK and significant enhancement of p38, IκB, and caspases. Although these results show that molecule Z is very sensitive in TRAIL signaling, the simulations, in the current form, do not directly envisage survival ratios (*SRs*) of cancer (HT1080) cells in Y and Z KDs.

Although we know the *SRs* [10] for wild-type (59 %), FADD KD (76 %), RIP KD (18 %), and TRAF2 KD (28 %), the *SR* in Y and Z KDs require evaluation. To evaluate their *SRs*, a link between *SR* and the survival and apoptotic molecule
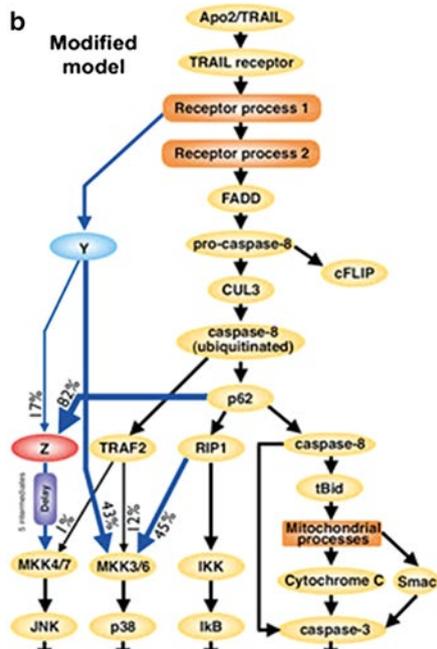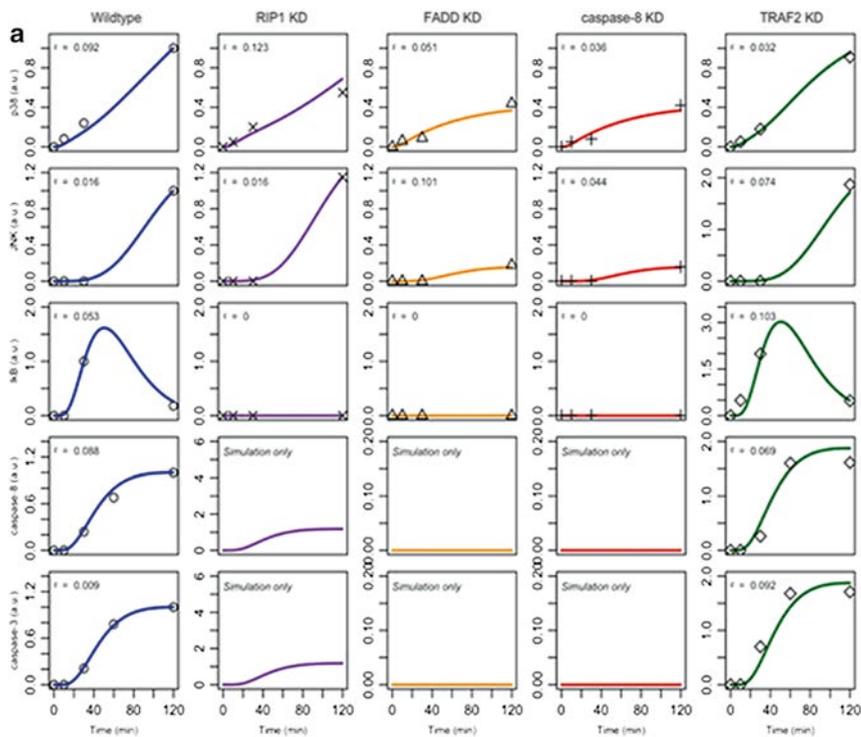
Fig. 8.5 *Simulations of the proposed TRAIL signaling topology.* (**a**) Comparison of M5 simulations (*solid lines*) with experimental data (*black points*) in wild-type, RIP1 KD, FADD KD, caspase-8 KD, and TRAF2 KD. (**b**) Static topology of the proposed model for TRAIL signaling pathway. Modifications are indicated by *blue arrows* (Adapted from Piras et al. [11])

Table 8.1 *Finalized TRAIL model reactions and parameters*. Note that to simulate each KD condition, we imposed null parameter value(s) for all reaction(s) involving the KD molecule

	Reaction/process			k (1/s)	Remarks
1	TRAIL	➜	TRAILR	8.13E-3	Binding of TRAIL ligand to receptor
2	TRAILR	➜	Receptor process 1	8.17E-3	O-glycosylation, internalization of receptors, formation of lipid rafts, etc.
3	Receptor process 1	➜	Receptor process 2	7.89E-3	
4	Receptor process 2	➜	Y	1.04E-3	Activation of novel molecule Y
5	Y	➜	MKK3/6	4.31E-1	Rapid activation of MKK3/6 via Y
6	Receptor process 2	➜	FADD	1.08E-3	FADD binds to TRAIL receptors
7	FADD	➜	pro-caspase-8	1.06E-3	pro-caspase-8 binds to FADD
8	pro-caspase-8	➜	CUL3	1,99E-3	Activation of CUL3
9	pro-caspase-8	➜	c-FLIP	1.00E-3	Activation of cFLIP
10	CUL3	➜	Ubiquitination of caspase-8	1.00E-2	Ubiquitination of caspase-8
11	Ubiquitination of caspase-8	➜	p62	9.92E-1	Activation of p62/sequestosome
12	Ubiquitination of caspase-8	➜	TRAF2	8.67E-2	Activation of TRAF2 by pro-caspase-8
13	p62	➜	Z	3.09E-1	Activation of novel molecule Z by p62
14	p62	➜	RIP1	6.77E-2	Activation of RIP1 by p62
15	p62	➜	caspase-8 (active form)	2.72E-2	Activation of caspase-8 (cleaved)
16	caspase-8 (active form)	➜	tBid	1.13E-5	Activation of tBid by caspase-8
17	caspase-8 (active form)	➜	caspase-3	1.48E-6	Activation of caspase-3 (extrinsic pathway)
18	tBid	➜	mitochondria	5.09E-2	Apoptotic intrinsic pathway via tBid
19	mitochondria	➜	Cytochrome C	2.64E-1	Activation of Cytochrome C
20	mitochondria	➜	Smac	2.79E-1	Activation of Smac
21	Cytochrome C	➜	caspase-3	2.81E-1	Activation of caspase-3 via apoptosome
22	Smac	➜	caspase-3	1.68E-1	Smac-dependent activation of caspase-3
23	caspase-3	➜	Apoptosis process	8.85E-3	caspase-3 depletion term
24	RIP1	➜	IKK	4.00E-4	Activation of IKK by RIP1
25	RIP1	➜	MKK3/6	5.04E-1	Activation of MKK3/6 by RIP1 (novel)
26	IKK	➜	IκB	3.45E-1	Activation of IκB by IKK
27	IκB	➜	NF-κB	8.99E-4	Activation of NF-κB by IκB
28	NF-κB	➜	Survival process	1.00E-1	NF-κB depletion term
29	TRAF2	➜	MKK3/6	7.24E-5	Activation of MKK3/6 by TRAF2
30	TRAF2	➜	MKK4/7	2.63E-6	Activation of JNK pathway by TRAF2
31	MKK3/6	➜	p38	2.37E-4	Activation of p38 by MKK3/6
32	p38	➜	Survival process	1.31E-5	p38 depletion term
33	Y	➜	Z	3.07E-1	Intermediates for delayed JNK activation
34	Z	➜	X1	8.76E-4	
35	X1	➜	X2	3.18E-3	
36	X2	➜	X3	7.48E-3	
37	X3	➜	MKK4/7	2.21E-3	Activation of JNK through bypass
38	MKK4/7	➜	JNK	1.81E-4	Activation of JNK by MKK4/7
39	JNK	➜	Survival process	2.36E-4	JNK depletion term

Highlighted rows indicate novel features of the TRAIL signaling pathway
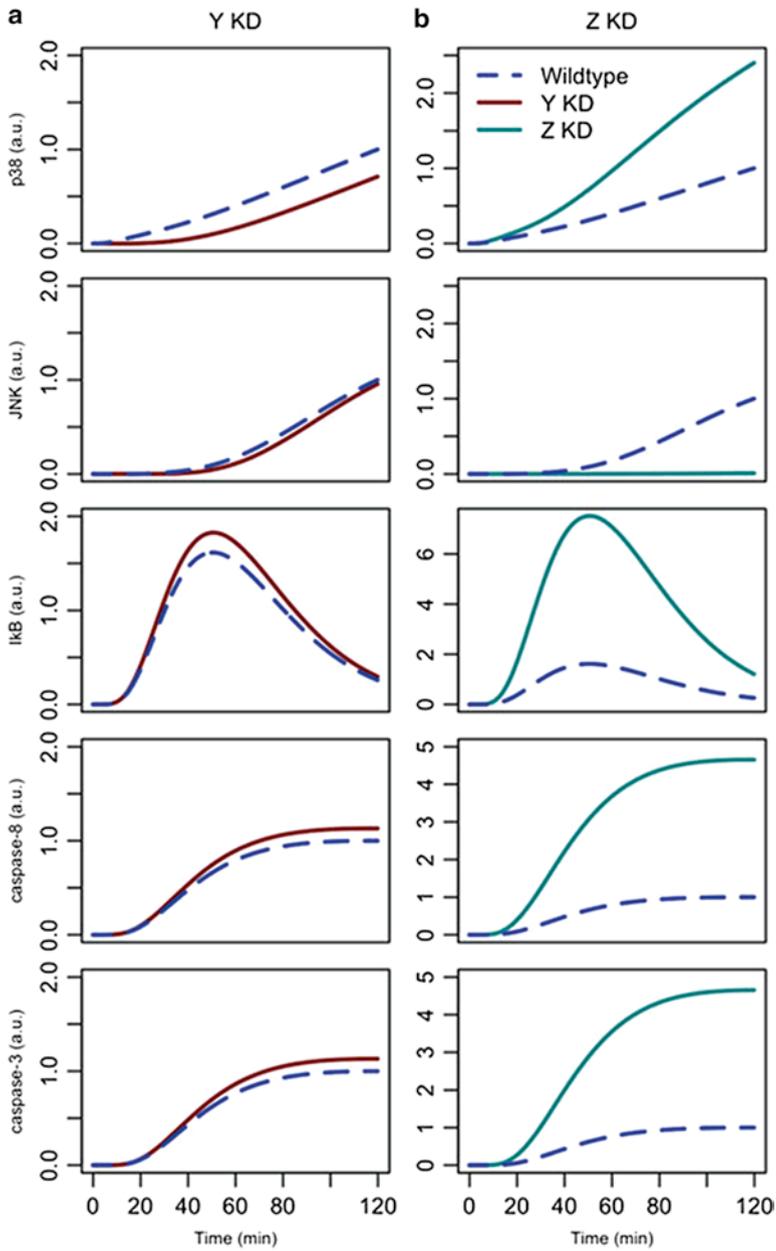
Fig. 8.6 *Simulation profiles of p38, JNK, IκB, and caspase-8 and -3 using final TRAIL model M5:* ***Y*** *KD (**a**) and **Z** KD (**b**) (Adapted from Piras et al. [11])*

temporal activation profiles are required. Because the area under the curve (*AUC*) of each apoptosis and survival molecule activation profile with time indicates an intensity measure of their respective process, the AUCs are used to connect with the *SR*.

To do this, a theoretical cell survival metric, or *CSM*, which evaluates the net AUC of survival (IκB, JNK, p38) and apoptotic (caspase-8 and -3) molecules is first introduced. The *CSM* for the *k*th condition is

$$CSM_k = \alpha AUC_k^{Survival} - \beta AUC_k^{Apoptosis} \tag{8.1}$$

$$AUC_k^{Survival} = \frac{1}{3}\left(AUC_{I\kappa B,k} + AUC_{p38,k} + AUC_{JNK,k}\right) \tag{8.2}$$

$$AUC_k^{Apoptosis} = \frac{1}{2}\left(AUC_{caspase-8,k} + AUC_{caspase-3,k}\right) \tag{8.3}$$

where survival and apoptosis AUCs are averaged over their respective molecules, and α and β are weight constants that will be determined from the actual *SR*.

Now, because the net AUCs are related to the *SR*, *CSM* is an unknown function of *SR*.

$$SR_k = f(CSM_k) \tag{8.4}$$

We tried a linear relationship:

$$SR_k = \delta(CSM_k) \tag{8.5}$$

However, this did not produce a solution. Next, we used polynomial expansion, and finally arrived at the exponential fitting:

$$SR_k = \lambda e^{CSM_k} \tag{8.6}$$

To solve Eqs. 8.1 and 8.6, which have more unknown parameters than the number of equations, we set $CSM_{WT}=0$ for wild-type (which is our benchmark), so that positive CSM_k denotes more survival than wild-type and negative denotes more death than wild-type for the *k*th condition, which now excludes the wild-type. Next, putting $CSM_{WT}=0$ in Eq. 8.6 yields $\lambda=0.59$ (because the experimental *SR* for wild-type is 0.59 and $e^0 = 1$).

Substituting λ back into Eqs. 8.1 and 8.6 for other conditions, three possible solutions for α and β (because we have two parameters for three equations) are obtained. Solving α and β using (i) SR_{FADDKD} and SR_{RIPKD}, the evaluated (predicted) *SR* for TRAF2 KD, *Y* KD, and *Z* KD is shown in Fig. 8.7a. Alternatively, solving α and β using (ii) SR_{FADDKD}, $SR_{TRAF2KD}$ and (iii) SR_{RIPKD}, $SR_{TRAF2KD}$ also produces similar *SR* for TRAF2 KD, *Y* KD, and *Z* KD (Fig. 8.7b, c). Notably, among the three solutions, the most conservative *SR* is about 0.05 for *Z* KD. That is, based on the survival ratio calculations, *Z* KD in TRAIL-stimulated HT1080 cells will likely produce 95% cell death.
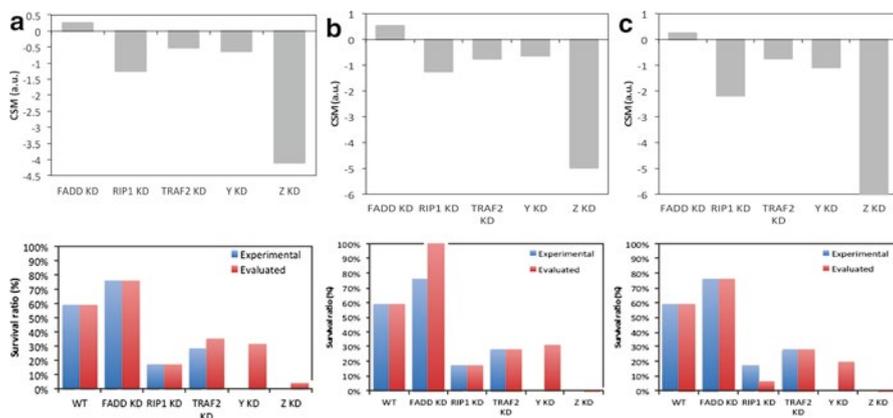
Fig. 8.7 *Identifying key target for sensitizing TRAIL resistance.* Cell survival metric (*CSM*) and survival ratio (*SR*), for all KDs relative to wild-type $CSM = 0$ solving α and β using experimental *SR* of (**a**) RIP1 and FADD KDs, (**b**) RIP1 and TRAF2 KDs, and (**c**) FADD and TRAF2 KDs (Adapted from Piras et al. [11])

Thus, among all investigated KDs, the *Z* KD results in the most negative *CSM* and the least *SR* (with only about 5 % surviving cells compared with 18 % and 36 % for RIP1 and *Y* KDs, respectively; Fig. 8.7). This result occurs because, through *SFR* (*response rule 4*), the *Z* KD enhances the caspases activations more than the survival molecules (Fig. 8.6b). Thus, *Z* KD shows the most desirable outcome of maximizing cell death in all tested conditions, making it clearly the best predicted target candidate for TRAIL-resistant HT1080 cells.

To verify the overall result, experiments on wild-type TRAIL-stimulated HT1080 cells were performed. Although it is not possible to perform experiments on the still uncharacterized *Z* KD cells, the *SR* of wild-type cells is reinvestigated. Notably, our experiments successfully reproduced approximately 60 % *SR* observed for 1,000 ng/ml of TRAIL stimulation (Fig. 8.8). The validation of wild-type data demonstrates that the average response model can be legitimately used to identify an appropriate candidate, through computational simulations, for enhancing TRAIL-based strategy.

To summarize, there has been great interest during the past decade on the usage of TRAIL, because of its ability to trigger the apoptotic pathways, as a strategy to fight the progression of cancer. Although successful in certain cancer types, TRAIL has not become a general candidate as many types of cancers are able to evade the apoptotic property of TRAIL. Recent work has shed light on the resistance mechanisms in TRAIL-based therapies; nevertheless, the understanding of counteracting cell survival and apoptotic pathways and finding ways to sensitize TRAIL-based strategy remain poor.

Drugs that upregulate TRAIL receptors (e.g., proteasome inhibitors) in resistant cancers may not be effective as they are likely to enhance both cell survival and apoptotic pathways, with the net effect not necessarily enhanced cell death.
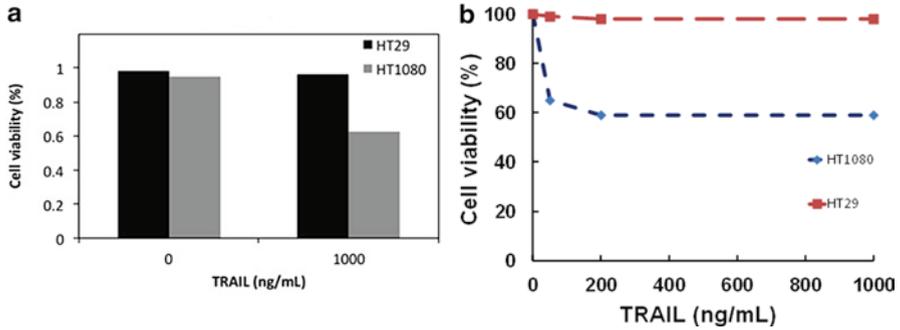
Fig. 8.8 *Experimental verification of wild-type HT1080 and HT29 cells to TRAIL stimulation*. (**a**) Wild-type HT1080 and HT29 (control) cells show 60 % and 95 % survival, respectively, for 1,000 ng/ml of TRAIL stimulation. HT1080 and HT29 cells were cultured in 12-well plates (60,000 cells/well) and incubated for 24 h. Cells were transferred to a culture medium containing TRAIL/Apo2L (0 and 1,000 ng/ml) and incubated for 18 h, then washed using phosphate-buffered saline (PBS) solution, detached from the plate using trypsin-EDTA, and centrifuged. Cell pellets were resuspended in 200 μl 1× binding buffer, 5 μl AnnexinV-FITC, and 10 μl propidium iodide, and incubated at room temperature, protected from light, for 15 min. Cell suspension was pipetted into poly round tubes through the cell-strainer cap; fluorescence intensity was then measured using an EPICS XL flow cytometer. TRAIL stimulation did not induce noticeable apoptosis of HT29 cells (negative control). On the other hand, 40 % of HT1080 cells underwent apoptosis after 18 h upon TRAIL stimulation (1,000 ng/ml) (From Piras et al. [11]) (**b**) Cell viability for HT1080 (*blue*) and HT29 (*red*) cells for indicated dosage of TRAIL (Data obtained from Varfolomeev et al. [10])

Further studies on using combinatorial treatment of TRAIL with downstream targets that selectively suppress cell survival, such as NF-κB and MAP kinase inhibitors, or enhancing apoptosis by suppressing the suppressors of caspases, have recently been investigated. The reduced cell survival activity or increased apoptosis produced, generally, an increase in the net effect of cell death, providing good prospective for increasing the efficacy of TRAIL-based strategies. However, these strategies have focused on suppressing either the cell survival or apoptosis activity, independently. It remains unclear which strategy among these is optimal for the various TRAIL-resistant cancer types. Thus, we require a strategy that considers the dual mode of suppressing survival and enhancing the apoptosis pathway simultaneously.

In this chapter, a systemic strategy that considers both the cell survival and apoptotic dynamics to provide a more mechanistic way to target TRAIL resistance is shown. The dynamic perturbation-response approach, successful to model the Toll-like receptor (TLR) (Chaps. 4, 5, 6) and TNF (Chap. 7) pathways, is used to examine the signaling mechanisms of NF-κB, MAP kinases, and caspase activation in TRAIL-stimulated HT1080 cells. Starting from the literature created a generalized TRAIL signaling topology, first, using response rules novel features, namely, (i) a FADD-independent pathway(s) to activate p38 and JNK, bypassing the primary and secondary DISCs and through novel molecules *Y* and *Z*, (ii) a crosstalk between RIP1 and p38 via MKK3/6, (iii) a crosstalk between p62 and JNK via *Z*, and (iv) intermediary step(s) or molecule(s) upstream of JNK are inferred.

These inclusions are necessary for the computational model to successfully reca-pitulate experimental outcome in all investigated conditions (wild-type, RIP1 KD, FADD KD, caspase-8 KD, and TRAF2 KD).

Second, to determine the best strategy to induce apoptosis in TRAIL-resistant HT1080 cells, the net effect of NF-κB, MAP kinases, and caspase activation by evaluating their cell survival metric, *CSM*, and making a link to the survival ratios (*SRs*) for various KD conditions was investigated. Overall, the simulations suggest that the optimal target is the novel molecule *Z*, whereby its removal is predicted to produce about 95 % HT1080 cell population death (Fig. 8.7).

Recent studies have indicated the roles of PI3K, Akt, and MADD for TRAIL resistance [12, 13]. These entities may belong to the novel FADD-independent path-ways, and one of these could well represent the molecule *Y*. On the other hand, the novel molecule *Z*, which is activated by p62 to specifically activate JNK in the model, acts as a connector between the primary and secondary DISC. Performing a search of the protein–protein interaction database [14] for p62 interacting partners shows protein kinase C (PKC) family members as likely candidates. Further litera-ture search supports PKC-ζ [15] as a possible candidate.

It is important to note that although the average response model may not pinpoint a specific molecular target exactly, nevertheless, it will be worthwhile to investigate molecules that interact with p62 for the search for optimal target for effective cell death in TRAIL-resistant HT1080 cells. Taken as a whole, the approach presented here provides a promising contribution toward systemically analyzing the dynamics of cell survival and apoptotic pathways for the sensitization strategy for TRAIL-based cancer therapy.

This chapter provides further data that show novel features of the TRAIL signaling can be revealed through the law of conservation and first-order response equations. From this result, we theoretically demonstrate that targeting a molecule at the survival and apoptosis pathway junction can provide an optimal solution to treat TRAIL resis-tance. It suppresses JNK and, at the same time, enhances caspase activities.

This result can be considered as surprising because the vast diversity of molecu-lar constituents, issues of heterogeneity, and spatiotemporal effects such as diffu-sion and crowding within cells are likely to make the TRAIL signaling response nonlinear and difficult to conceptualize computationally (see the following chap-ter). In contrast, our data suggest that cells, as a population, are able to discard individual differences to achieve a global average response that follows simple rules [16–18]. This is clearly the underlying success that the final first-order response model is able to simulate multiple experimental conditions.

Because biological complexity such as heterogeneity and fluctuations or noises are observed at single-cell resolution, it will be interesting to compare the single-cell dynamics of HT1080 cells in wild-type and PKC-ζ mutants with the population response presented here. Also, it will be crucial to investigate how the heteroge-neous single-cell responses in TRAIL signaling could be guided to provide a pos-sible 100 % cell death, at least in a dish. In this light, the study of single-cell noise will be critical to enhance our modeling aspects further to generate and investigate single-cell response models. The subsequent chapters focus on such complex issues.

References

1. Finn OJ (2008) Cancer immunology. N Engl J Med 358:2704–2715
2. Zitvogel L, Apetoh L, Ghiringhelli F, Kroemer G (2008) Immunological aspects of cancer chemotherapy. Nat Rev Immunol 8:59–73
3. Yang A, Wilson NS, Ashkenazi A (2010) Proapoptotic DR4 and DR5 signaling in cancer cells: toward clinical translation. Curr Opin Cell Biol 22:837–844
4. Frew AJ, Lindemann RK, Martin BP, Clarke CJ, Sharkey J, Anthony DA, Banks KM, Haynes NM, Gangatirkar P, Stanley K, Bolden JE, Takeda K, Yagita H, Secrist JP, Smyth MJ, Johnstone RW (2008) Combination therapy of established cancer using a histone deacetylase inhibitor and a TRAIL receptor agonist. Proc Natl Acad Sci USA 105:11317–11322
5. Dimberg LY, Anderson CK, Camidge R, Behbakht K, Thorburn A, Ford HL (2012) On the TRAIL to successful cancer therapy? Predicting and counteracting resistance against TRAIL-based therapeutics. Oncogene. doi:10.1038/onc.2012.164
6. Jin CY, Park C, Kim GY, Lee SJ, Kim WJ, Choi YH (2009) Genistein enhances TRAIL-induced apoptosis through inhibition of p38 MAPK signaling in human hepatocellular carcinoma Hep3B cells. Chem Biol Interact 180:143–150
7. Ammann JU, Haag C, Kasperczyk H, Debatin K, Fulda S (2009) Sensitization of neuroblastoma cells for TRAIL-induced apoptosis by NF-κB inhibition. Int J Cancer 124:1301–1311
8. Baxevanis CN, Perez SA, Papamichail M (2009) Combinatorial treatments including vaccines, chemotherapy and monoclonal antibodies for cancer therapy. Cancer Immunol Immunother 58:317–324
9. Tsuchiya M, Piras V, Choi S, Akira S, Tomita M, Giuliani A, Selvarajoo K (2009) Emergent genome-wide control in wildtype and genetically mutated lipopolysaccharides-stimulated macrophages. PLoS One 4:e4905
10. Varfolomeev E, Maecker H, Sharp D, Lawrence D, Renz M, Vucic D, Ashkenazi A (2005) Molecular determinants of kinase pathway activation by Apo2 ligand/tumor necrosis factor-related apoptosis-inducing ligand. J Biol Chem 280:40599–40608
11. Piras V, Hayashi K, Tomita M, Selvarajoo K (2011) Enhancing apoptosis in TRAIL-resistant cancer cells using fundamental response rules. Sci Rep 1:144
12. Xu J, Zhou J, Wei W, Wu GS (2010) Activation of the Akt survival pathway contributes to TRAIL resistance in cancer cells. PLoS One 5:e10226
13. Li P, Jayarama S, Ganesh L, Mordi D, Carr R, Kanteti P, Hay N, Prabhakar BS (2010) Akt-phosphorylated mitogen-activated kinase-activating death domain protein (MADD) inhibits TRAIL-induced apoptosis by blocking Fas-associated death domain (FADD) association with death receptor 4. J Biol Chem 285:22713–22722
14. He M, Wang Y, Li W (2009) PPI finder: a mining tool for human protein–protein interactions. PLoS One 4:e4554
15. Hirai T, Chida K (2003) Protein kinase Cζ (PKCζ): activation mechanisms and cellular functions. J Biochem 133:1–7
16. Selvarajoo K (2011) Macroscopic law of conservation revealed in the population dynamics of Toll-like receptor signaling. Cell Commun Signal 9:9
17. Selvarajoo K (2012) Understanding multimodal biological decisions from single cell and population dynamics. Wiley Interdiscip Rev Syst Biol Med 4:385–399
18. Piras V, Tomita M, Selvarajoo K (2012) Is central dogma a global property of cellular information flow? Front Physiol 3:439

Chapter 9
Stochasticity and Variability: Insights from Single-Cell Dynamics

The population-wide averaging approaches discussed so far have been instrumental not only for cell signaling but also in our basic understanding of myriad deterministic biological processes such as growth and metabolism (see Chap. 1). For developmental biology, on the other hand, the major challenge has been to understand how multimodal decisions are undertaken. For instance, a single stem or progenitor cell can produce distinct lineages, which can be tilted by even small external perturbations [1, 2].

Also, it is astounding to observe how genetically identical cells produce diverse phenotypes, such as during cell cycles, aging, and epigenetic regulation. Moreover, the cooperative behavior of microorganisms, such as *Escherichia coli* and yeast, to form biofilms that enhance their survival capacity to environmental threats is distinct from their individual activity. Thus, the study of phenotypic diversity or individual to cooperative response cannot lend itself to population-based readout because multiple measurements of each cell across time are required to unravel the multifaceted decision capability of living cells.

The concept and importance of cellular variability, spatiotemporal effects of molecules and entropy in living systems, was already investigated several decades ago, when trained physicists such as Max Delbrück and Erwin Schrödinger switched their interest to biology. Adding probability events to differential equations, Delbrück investigated the fluctuations of chemical interactions and proposed that the outcome of cellular decisions can be variable, as he observed in the number of phage produced per virus-infected *E. coli* [3, 4]. In his famous book *What Is Life?* [5], Schrödinger searches for physical laws to explain molecular events such as cell divisions and appreciates the presence of quantum (stochastic or heterogeneous) information in living systems to produce diverse behaviors. Three decades later, Spudich and Koshland showed that bacteria grown in a homogeneous environment display heterogeneous behavior over a sustained period and reasoned the phenomenon was the result of fluctuations of a small number of key molecules [6].

The pioneering and fundamental observations from such studies that consider beyond average response behaviors have reinforced the fact that not all cells behave the

same, or possess the same amount of intracellular constituents or reaction kinetics. One key reason is that each cell within a population is not identical to other cells in morphology or shape, and the intracellular molecular environment is highly inhomogeneous. Population-wide average techniques are, therefore, not suitable to understand cellular variability and, subsequently, experimental techniques progressed toward addressing the issue of heterogeneity and their implications from single-cell approaches. Thus, the understanding of how multimodal cellular decisions can be undertaken by living systems, for example, in the multifaceted outcomes of stem cell differentiation, requires nonaveraging and nonlinear approaches considering variability.

Biological Noise: Stochasticity and Heterogeneity

The advent of modern microscopes (e.g., confocal, electron, fluorescence), laser techniques, imaging technologies, and microfluidics has enabled the measurement and comparison of intracellular biological components in space–time and between single cells in high definition (Box 9.1) [7–13]. For example, Elowitz and colleagues built strains of *E. coli*, tagging the distinguishable cyan (*cfp*) and yellow (*yfp*) alleles of green fluorescent protein (*gfp*) in the chromosome, and showed that their expression fluctuated rapidly in time (Fig. 9.1a) [14]. Such fluctuating responses of gene and protein expression over time have been observed in numerous other studies

---

Box 9.1 Popular Single-Cell Experimental Approaches

Fluorescence correlation spectroscopy (*FCS*): Single molecules are fluorescently labeled and counted to track their mobility, interactions, or concentrations. A detector captures the fluorescence of the single molecule that travels through a subspace within the optical system. A correlation analysis of fluctuation of the fluorescence intensity produces the rate of diffusion and absolute number of the fluorescent molecules. Using an extrapolation method, the concentration and size of the molecules are subsequently determined [7].

Fluorescence in situ hybridization (*FISH*): Fluorescent probes are used to detect a specific region of DNA sequences and chromosomes where it binds with a high degree of sequence complementarity. Next, fluorescence microscopy determines the location of the probe bound to the chromosomes. Using various combinations of fluorochromes, FISH generates different colors in chromosomes that allows monitoring each one independently. FISH is also used to detect and localize specific mRNAs, to identify the spatiotemporal patterns of gene expression within a single cell or population of cells [8].

(continued)

Box 9.1 (continued)

Confocal laser scanning microscopy (*CLSM or LSCM*): Using the aid of computational imaging techniques, CLSM produces high-resolution in-focus images of fluorescent proteins, especially signaling molecules. This microscopy has been successfully used to compare the spatial temporal localization of key molecules in live cells. Several dyes has been recently developed, and it is now possible to tract several molecules at the same time [9].

Fluorescence resonance energy transfer (*FRET*): This method measures the excitation energy when two colored molecules collide. The efficiency of FRET is obtained by tracking the binding interaction, which results in changes in the fluorescence intensity between donor and acceptor molecules. FRET allows the investigation of several biological processes that produce changes in molecular mobility and proximity with high-definition spatial resolution, compared with conventional optical microscopy [10].

Fluorescence-lifetime imaging microscopy (*FLIM*): Similar in principle to FRET, FLIM measures the differences in the exponential decay rate of the fluorescence of the donor molecules. That is, instead of measuring intensity, the FLIM lifetime imaging allows differentiation between behavior of molecules of the same color over time [11].

Fluorescence recovery after photobleaching (*FRAP*): Target fluorescent molecules are photobleached within a cell by exposure to high-intensity blue light. A microscope is then used to track the movements of the fluorescent molecules. The measurement of the intensity with time enables quantifying the recovery of fluorescence. It has been principally used to analyze movement of proteins within a membrane and protein binding [12].

Microfluidics: A microfabricated device is used together with cytometry devices that allows a small volume of cells in liquid to pass through microstructures and form cell cultures. These cells are then imaged using real-time fluorescent imaging. Microfluidics allows high-throughput monitoring of several single cells at the same time on a chip, so could have advantages of cost and speed [13].

[15–17]. On the other hand, flow cytometry analyses have revealed cell-to-cell heterogeneity, Gaussian-like distributions for the abundance of a given protein per cell, in a clonal population of cells (Fig. 9.1b) [18, 19].

Thus, each cell within a tissue population possesses varying amounts of individual molecular constituents, in a highly inhomogeneous intracellular environment with spatiotemporal effects of molecular crowding and diffusion (Fig. 9.2a). The low abundance of numerous molecules produces stochastic cellular response or
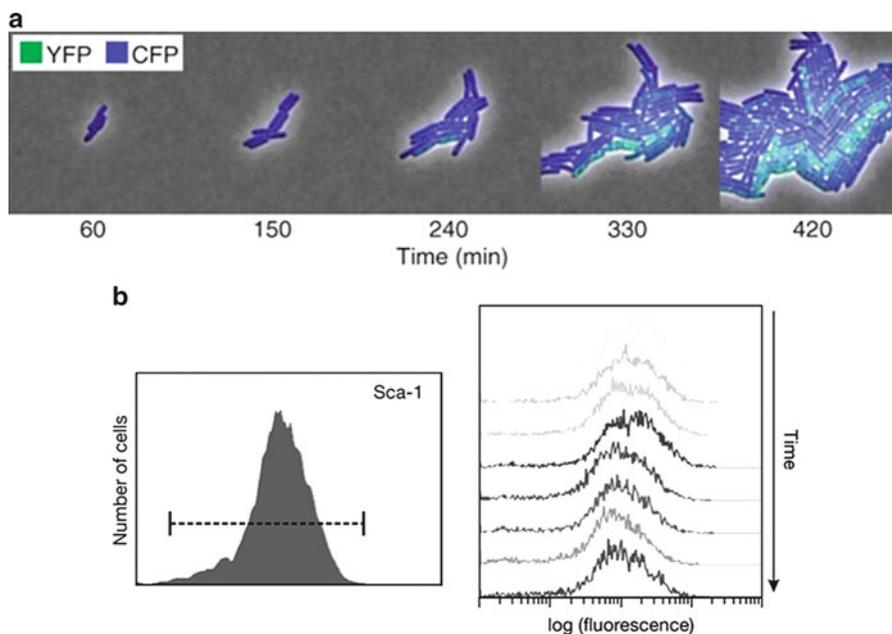
Fig. 9.1 Stochasticity and variability observed in single cells. (**a**) Time-series schematic of green fluorescent protein (GFP) in single cells. Stochasticity or fluctuations in protein (*YFP* and *CFP*) expression show *color* variations between each cell as time evolves in *Escherichia coli* (Adapted from Dunlop et al. [15].) (**b**) Variation (*left*) and stability in time (*right*) of Sca-1 expression in a multipotent mouse hematopoietic cell line (Adapted from Chang et al. [19])

noise, such as in the dynamics of gene transcription and decay. Together, the effect of space, crowding, stochasticity, and heterogeneity of molecular constituents make single-cell response variable, noisy, and highly complex (Fig. 9.2b).

The spatiotemporal organization of intracellular molecules is important for distinct signal transduction of key conserved molecules, such as IκB kinase (IKK) complexes, between distinct stimuli, for example, lipopolysaccharide (LPS) and tumor necrosis factor (TNF) stimulation [22]. Moreover, the cellular environment is heterogeneous with macromolecular complexes and crowding. The diffusive rates of molecular reactions, under such situations, are variable and able to produce vastly unanticipated responses. For example, it was believed that Tom40, a key component in the mitochondrial protein import machinery, freely diffuses in the mitochondrial outer membrane. However, a recent single-molecule tracking method demonstrates that Tom40, although is highly mobile, is confined in its behavior [23].

In the cell cycle of human cells, fluorescence microscopy in combination with laser micro-irradiation revealed different spatiotemporal dynamics of Nbs1 and Chk2, key mediators maintaining genomic stability for ataxia-telangiectasia-mutated (ATM)-controlled checkpoint pathways induced by DNA double-strand breaks, and as a result, indicated their distinct roles [24]. These in vivo analyses demonstrate the
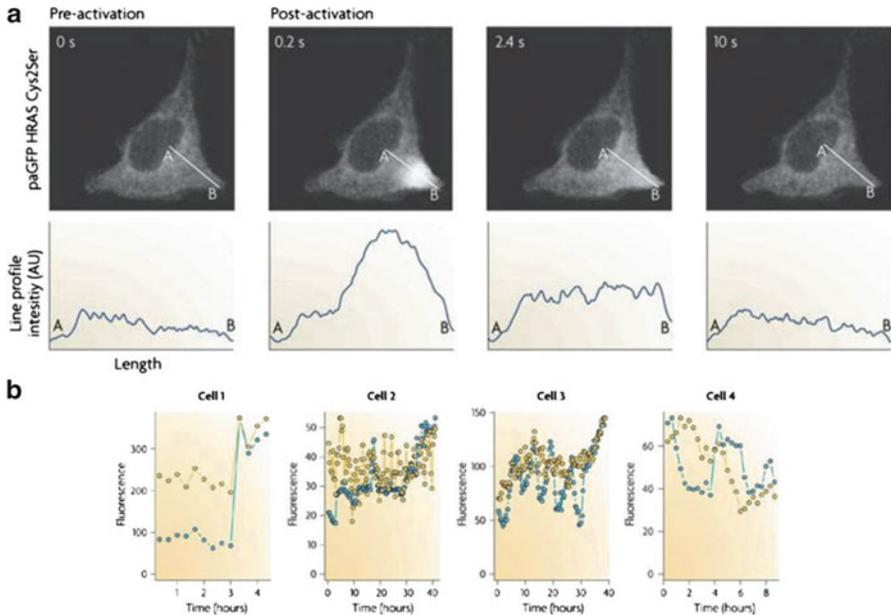
Fig. 9.2 Noisy dynamics of individual molecules and cells. (**a**) Illuminating green fluorescent protein (*paGFP*) with *blue* light on a single photo-activatable cell (*upper panel*) results in paGFP diffusing away from the source in a stochastic manner, as shown by the intensity plots (*lower panels*). Intensity was measured in arbitrary units (AUs) (Adapted from Dehmelt and Bastiaens [20].) (**b**) Fluorescence levels for four individual cells show stochastic response. *Blue circles* represent tumor suppressor protein p53 dynamics; *yellow circles* represent the dynamics of ubiquitin E3 ligase MDM2 (Adapted from Wilkinson [21])

importance of the spatiotemporal nature of individual proteins that cannot be observed from in vitro analyses. Thus, putting together the effect of space–time, crowding, and heterogeneity of molecular constituents can make single-cell responses highly variable and noisy. However, are single-cell responses predictable?

The Origins of Biological Noise

The single-cell heterogeneity within cell populations, measured by transcription, phosphorylation, morphology, and motility, arises from a combination of intrinsic and extrinsic elements. Increasingly, investigators recognize that the stochasticity in gene or protein expression results from two main sources of noise: (i) intrinsic or 'uncorrelated' noise, the random nature of biochemical reactions, for example, from low copy numbers of intracellular molecules in a Poisson process; and (ii) extrinsic or 'correlated' noise, fluctuations in other cellular components or states that indirectly affect the expression of a specific gene or protein [14, 25].

It has now been demonstrated, both computationally and experimentally, that stochasticity in mRNA and variability in protein expression are not simply the result of the effect of low copy number on a Poisson gene regulatory process, but rather are caused by the quantal or bursting nature of promoter activity (Fig. 9.3) [26, 27]. Moreover, by varying the rates of transcription and translation of a bacterial protein, it is now known that increasing transcriptional, and not translational, noise is responsible for the variability in reporter protein expressions [15, 28].

Noise in a Simple Gene Regulatory Network Is Crucial for Bimodal Decisions

For a long time, noise has been considered as unwanted obstacle or nuisance in many disciplines, resulting in numerous efforts that focused on suppressing the causes and effects of noise. However, the usefulness of noise has gained valuable recognition across disciplines in the past few decades. In biology, only in the early part of the past decade have we seen much interest and progress. This is mainly due to the lack of experimental techniques that could measure noise reliably.

In physics, it is well known that a small deviation in the initial condition could lead to diverse response of a deterministic process. This phenomenon, termed chaos, can be illustrated using a ski slope with bumps (mogul skiing; Fig. 9.4a, insert). Here, gravitational force drives the skier to the finish point and the bumps create a landscape to develop error or noise that changes the lineage of each trajectory (attractor) to distinct pathways on different attempts. Hence, noise in a chaos process can be used to switch deterministic fates. For the cell differentiation process, how does a single cell diversify its lineage in time (Fig. 9.4b)? The clue may lie in biological noise on a chaos process (see Chap. 12).

In *Saccharomyces cerevisiae*, the control of the transcription rate of GAL contributed to the heterogeneity of reporter yeast-enhanced green fluorescent protein (yEGFP protein) expression within a clonal population [17]. Moreover, it was shown that increasing the transcriptional noise propagation in the corresponding gene regulatory network resulted in the generation of bistable expression states of yEGFP. This pioneering work on actual cells is a good example of how the control of noise can nonintuitively regulate the diversity of molecular constituents in living systems. But how is noise or heterogeneity important for cellular behavior? Or, what is the purpose of biological noise?

Certain types of bacteria, as an alternative to sporulation, capture DNA from the surroundings in nutrient-limited conditions for their survival. This phenomenon is termed as competence. In *Bacillus subtilis*, this process is known to be random and binary, with only about 10–20 % cells achieving competence. The master regulatory transcription factor for the behavior is ComK, where the low or high concentration of this protein is associated with the vegetative or competent state, respectively, with a threshold level shifting the balance (Fig. 9.5a) [32, 33]. The level of stochasticity,
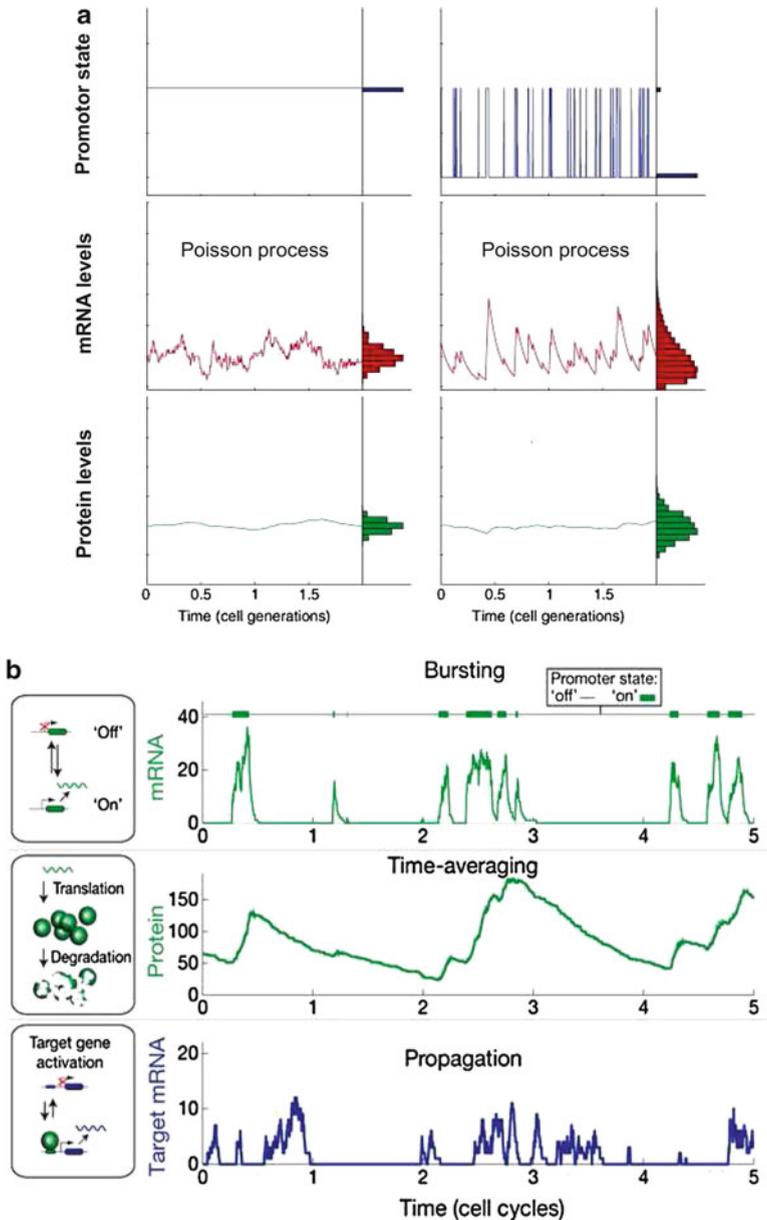
Fig. 9.3 Bursting origins for stochastic gene and variable protein expression. (**a**) Theoretical observation. *Left*: When the promoter state is always on, and the production and degradation of mRNA occur randomly in a Poisson process, the resultant protein expressions follow a narrow distribution. *Right*: When promoter state on–off is quantal, and the production and degradation of mRNA occur randomly in a Poisson process, the resultant protein expressions follow a Gaussian-like distribution (Adapted from Kaern et al. [28].) (**b**) Schematic of experimental observation in *Escherichia coli* or *Bacillus subtilis* (Adapted from Eldar and Elowitz [29])
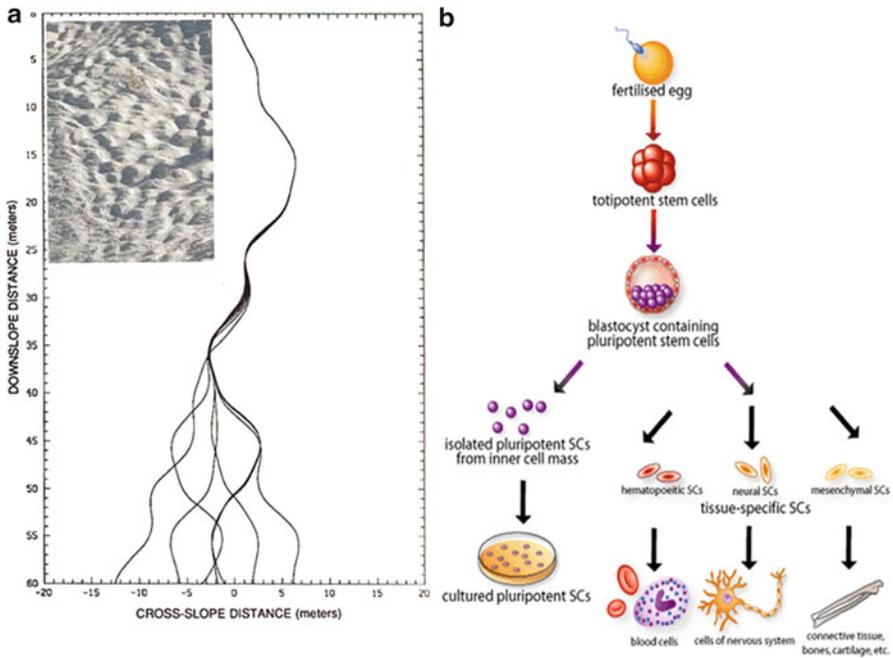
Fig. 9.4 Cell differentiation process mimicking a chaotic trajectory. (**a**) Diverging endpoints of the trajectories of seven boarders with minute (1-mm) changes in course maneuver at a ski slope with moguls (*insert*) (Adapted from Chaudry [30].) (**b**) Schematic of mammalian cell differentiation process. *SC*, stem cells (Obtained from Lorenz [31])

or noise, in the expression of *comK* mRNA was initially demonstrated to be responsible for switching between the states. Subsequently, further work showed that the entry into and exit from the competent state occurred through an excitable core module with positive and negative feedback loops of ComK with ComS. Notably, the excitable dynamics of ComG and ComS generated by stochasticity was crucial for the regulation of *B. subtilis* competence (Fig. 9.5b) [34].

In genetics, the investigation of penetrance considers the nondeterministic or probabilistic outcomes in biological phenotype for a particular mutation of a gene. For example, if a variant in a particular gene is associated with a disease with 80 % penetrance, then one would expect 80 % of a population with that gene mutation will develop the disease. The remaining 20 % displays incomplete penetrance.

In the study of incomplete penetrance of *Caenorhabditis elegans* intestinal differentiation, the mutation of the *skn-1* gene affected the transcriptional network of intestinal specification and produced indeterminate outcomes where some embryos failed in the development of intestinal cells, whereas others became intestinal precursors [35]. The differentiation phenotype of *skn-1* mutant *C. elegans* was determined when the fluctuating expression of a downstream gene, *end-1*, reached a certain threshold. Notably, the mutation of *skn-1* caused the *med-1/2* and *end-3* transcripts to
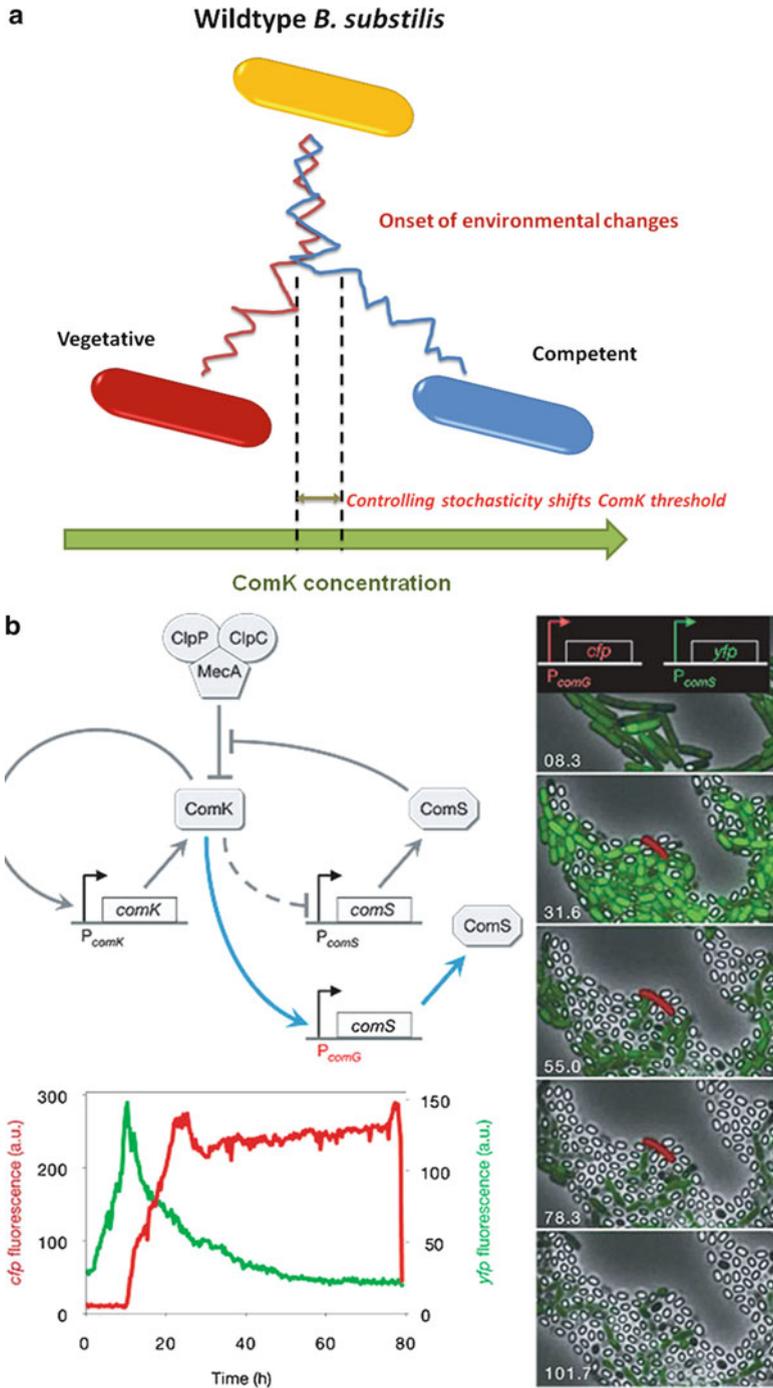
Fig. 9.5 Transition from vegetative to competent state in *Bacillus subtilis*. (**a**) Threshold in the concentration of ComK, with stochastic noise switching between the two fates. (**b**) The excitable dynamics of ComS (*green*) and ComG (*red*) in a feedback system controls competent state (From Süel et al. [34])
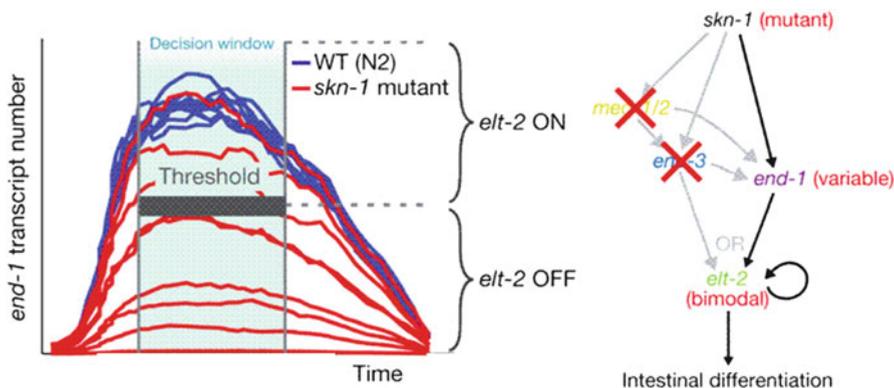
Fig. 9.6 Stochasticity and threshold effects in intestinal cell fate decision. Incomplete penetrance in *Caenorhabditis elegans* is also guided by noise in *end-1*, threshold expression (*left*), and topology (*right*) contributing to the decision (Adapted from Raj et al. [35])

essentially diminish and effectively be removed from the intestinal gut gene network (Fig. 9.6). As a result, the modified network increased the variability in *end-1*, which was crucial for changing the attractor state of intestinal cell differentiation. The error or noise generated by the resultant compromised gut network resembles the example of the changing fate of ski trajectories to error (Fig. 9.4a). Thus, the modification of a biological network through genetic mutants can change cell or attractor states of the relevant biological process via cellular noise (see Chap. 12).

For induced pluripotent stem cells (iPS) cells, we now fully appreciate the so-called Yamanaka factors (Oct3/4, Sox2, Klf4, c-Myc) that are crucial for changing attractor states of cell differentiation [36]. How do these factors trigger a different cell differentiation path? It is, perhaps, the insertion of these crucial molecules generating variability or noise in some key molecules, currently still unknown, along the cellular differentiation network that allows differentiated cells to become iPS cells. Although this may be a speculation, the next chapter recognizes the presence of certain key molecules that are able to suppress the single-cell noise response in cancer.

In summary, we have investigated the issue of biological noise measured from single cells and their implications in generating heterogeneity and diversity in cell response, especially for cell fate decision. Intriguingly, even though living systems possess thousands of genes, proteins, and metabolites, the foregoing examples investigating single-cell noise still support the population examples shown in Chap. 1, in that simple regulatory models are crucial in shaping the desired cell response. However, the major difference between the population-average and the single-cell studies is that the latter are able to produce bimodal or multimodal response when the level of stochastic noise are adjusted. In contrast, for the population models, where noise is not factored, additional regulatory features, such as feedback loops, are necessary to generate a non-unique response [37].

References

1. Losick R, Desplan C (2008) Stochasticity and cell fate. Science 320:65–68
2. Zernicka-Goetz M, Huang S (2010) Stochasticity versus determinism in development: a false dichotomy? Nat Rev Genet 11:743–744
3. Delbruck M (1940) Statistical fluctuations in autocatalytic reactions. J Chem Phys 8:120–124
4. Ellis EL, Delbruck M (1939) The growth of bacteriophage. J Gen Physiol 22:365–384
5. Schrödinger E (1944) What is life? Cambridge University Press, Cambridge
6. Spudich JL, Koshland DE Jr (1976) Non-genetic individuality: chance in the single cell. Nature 262:467–471
7. Marquer C, Lévêque-Fort S, Potier MC (2012) Determination of lipid raft partitioning of fluorescently-tagged probes in living cells by fluorescence correlation spectroscopy (FCS). J Vis Exp 62:3513
8. Ji Z, Zhang L (2012) Chromosomics: detection of numerical and structural alterations in all 24 human chromosomes simultaneously using a novel OctoChrome FISH assay. J Vis Exp 60:3619
9. Renda A, Nashmi R (2012) Spectral confocal imaging of fluorescently tagged nicotinic receptors in knock-in mice with chronic nicotine administration. J Vis Exp 60:3516
10. Hukasova E, Silva Cascales H, Kumar SR, Lindqvist A (2012) Monitoring kinase and phosphatase activities through the cell cycle by ratiometric FRET. J Vis Exp 59:3410
11. Suhling K, Levitt JA, Chung PH, Kuimova MK, Yahioglu G (2012) Fluorescence lifetime imaging of molecular rotors in living cells. J Vis Exp 60:2925
12. Nissim-Rafinia M, Meshorer E (2011) Photobleaching assays (FRAP & FLIP) to measure chromatin protein dynamics in living embryonic stem cells. J Vis Exp 52:2696
13. Huang Y, Agrawal B, Clark PA, Williams JC, Kuo JS (2011) Evaluation of cancer stem cell migration using compartmentalizing microfluidic devices and live cell imaging. J Vis Exp 58:3297
14. Elowitz MB, Levine AJ, Siggia ED, Swain PS (2002) Stochastic gene expression in a single cell. Science 297:1183–1186
15. Dunlop MJ, Cox RS 3rd, Levine JH, Murray RM, Elowitz MB (2008) Regulatory activity revealed by dynamic correlations in gene expression noise. Nat Genet 40:1493–1498
16. Raser JM, O'Shea EK (2004) Control of stochasticity in eukaryotic gene expression. Science 304:1811–1814
17. Blake WJ, Kaern M, Cantor CR, Collins JJ (2003) Noise in eukaryotic gene expression. Nature 422:633–637
18. Bar-Even A, Paulsson J, Maheshri N, Carmi M, O'Shea E, Pilpel Y, Barkai N (2006) Noise in protein expression scales with natural protein abundance. Nat Genet 38:636–643
19. Chang HH, Hemberg M, Barahona M, Ingber DE, Huang S (2008) Transcriptome-wide noise controls lineage choice in mammalian progenitor cells. Nature 453:544–547
20. Dehmelt L, Bastiaens PIH (2010) Spatial organization of intracellular communication: insights from imaging. Nat Rev Mol Cell Biol 11:440–452
21. Wilkinson DJ (2009) Stochastic modelling for quantitative description of heterogeneous biological systems. Nat Rev Genet 10:122–133
22. Verstrepen L, Bekaert T, Chau TL, Tavernier J, Chariot A, Beyaert R (2008) TLR-4, IL-1R and TNF-R signaling to NF-kappa-B: variations on a common theme. Cell Mol Life Sci 65: 2964–2978
23. Kuzmenko A, Tankov S, English BP, Tarassov I, Tenson T, Kamenski P, Elf J, Hauryliuk V (2011) Single molecule tracking fluorescence microscopy in mitochondria reveals highly dynamic but confined movement of Tom40. Sci Rep 1:195
24. Lukas C, Falck J, Bartkova J, Bartek J, Lukas J (2003) Distinct spatiotemporal dynamics of mammalian checkpoint regulators induced by DNA damage. Nat Cell Biol 5:255–260
25. Swain PS, Elowitz MB, Siggia ED (2002) Intrinsic and extrinsic contributions to stochasticity in gene expression. Proc Natl Acad Sci USA 99:12795–12800

26. Thattai M, van Oudenaarden A (2001) Intrinsic noise in gene regulatory networks. Proc Natl Acad Sci USA 98:8614–8619
27. Kaufmann BB, van Oudenaarden A (2007) Stochastic gene expression: from single molecules to the proteome. Curr Opin Genet Dev 17:107–112
28. Kaern M, Elston TC, Blake WJ, Collins JJ (2005) Stochasticity in gene expression: from theories to phenotypes. Nat Rev Genet 6:451–464
29. Eldar A, Elowitz MB (2010) Functional roles for noise in genetic circuits. Nature 467: 167–173
30. Chaudry A (2004) Stem cell bioengineering. Available at http://www.scq.ubc.ca/stem-cell-bioengineering/. Accessed on 2nd July 2013
31. Lorenz E (1995) The essence of chaos (The Jessie and John Danz Lecture Series). University of Washington Press, Seattle
32. Maamar H, Raj A, Dubnau D (2007) Noise in gene expression determines cell fate in *Bacillus subtilis*. Science 317:526–529
33. Mettetal JT, van Oudenaarden A (2007) Necessary noise. Science 317:463–464
34. Süel GM, Garcia-Ojalvo J, Liberman LM, Elowitz MB (2006) An excitable gene regulatory circuit induces transient cellular differentiation. Nature 440:545–550
35. Raj A, Rifkin SA, Andersen E, van Oudenaarden A (2010) Variability in gene expression underlies incomplete penetrance. Nature 463:913–918
36. Takahashi K, Yamanaka S (2006) Induction of pluripotent stem cells from mouse embryonic and adult fibroblast cultures by defined factors. Cell 126:663–676
37. Bhalla US, Iyengar R (2001) Robustness of the bistable behavior of a biological signaling feedback loop. Chaos 11:221–226

Chapter 10
Investigating Single-Cell Stochasticity in TRAIL Signaling

The development and analyses of the tumor necrosis factor (TNF)-related apoptosis ligand (TRAIL) signaling model for resistant cancer cell populations in Chap. 8 are described using simple linear response equations. Although the approach is indispensable for understanding deterministic and well-coordinated macroscopic response of cell population averages, the effect of biological noise revealed from single-cell approaches, mentioned in the previous chapter, requires consideration. This consideration is especially necessary for cancer populations, which consist of highly variable and heterogeneous cells. Thus, to consider the implications of cellular variability in TRAIL signaling, this chapter extends the TRAIL population model into a variable single-cell response model. The extension will allow the investigation of how biological noise, particularly the effect of stochasticity, on signaling reactions can affect the overall resistance mechanisms in human fibrosarcoma or HT1080 cells.

Stochastic Algorithm

The Gillespie algorithm is popularly used to generate probabilistic outcome of original deterministic reaction equations by converting them into a discrete and stochastic process [1]. The basic principle behind the Gillespie algorithm is that it transforms the average response model into memory-less Poisson or stochastic processes, where each reaction occurs stochastically based on a probability at the current state of the system, independently of previous states. The probability of a reaction, P_r, is related to its kinetic constant, k_r, by

$$P_r = \frac{k_r}{\sum_{i=1}^{R} k_i} \tag{10.1}$$

where R is the total number of reactions in the network. In other words, the probability of a reaction occurring is proportional to its kinetic constant.

To initialize a stochastic algorithm, the initial number of molecules of each species and their reaction rates are first specified. A Monte Carlo [1] step next generates random numbers to determine the next reaction to occur, and the time interval size τ is chosen:

$$\tau = \frac{1}{\sum_{i=1}^{R} k_i} ln \frac{1}{z} \tag{10.2}$$

where z is a random number from uniform (0,1) distribution. After each time interval, both the number of molecules and the reaction rates (based on probability distribution) are updated. The next time step is also determined, and the process iterates until the desired simulation period.

Stochastic TRAIL Signaling Model

The average TRAIL response model (Chap. 8, Table 8.1) was converted into a stochastic model based on the Gillespie algorithm. Apart from the first reaction, TRAIL → TRAILR, all other reactions and their parameters are kept identical to the original deterministic model. The first reaction in the average response model is represented by a first-order mass-action equation. This simplification was found to be reasonable for fixed concentrations of stimulation. Here, as the effect of stochasticity is being investigated for variable response, the model is required to be tested by varying the concentration of stimulation. Furthermore, cancer cells possess varying number of TRAIL receptors across their heterogeneous population. Hence, the first reaction cannot be modeled using the first-order mass-action equation and requires a new expression for the variable stochastic model.

Cancer cells are known to possess approximately 8,000 to 20,000 apoptosis-inducing TRAIL receptors (Death Receptor-4/5) on their surface. It is, therefore, reasonable to limit the maximum number of active TRAILR for inducing apoptosis to be about 20,000. Also, it is important to note that TRAILR activation saturates at a TRAIL concentration about 200 ng/mL, following a hyperbolic velocity profile for cellular apoptosis for HT1080 cells (see Fig. 8.8b) [2]. Thus, a Michaelis–Menten type equation is assumed for the TRAIL → TRAILR reaction:

$$\frac{d[\text{TRAILR}]}{dt} = \frac{V_{max}[\text{TRAIL}]}{K_M + [\text{TRAIL}]} - k[\text{TRAILR}] \tag{10.3}$$

where V_{max} is maximum or saturation reaction velocity (M/s) and K_m (M) and k (1/s) represent rate constants and are determined by fitting with a experimental velocity profile.

In contrast to the population-level deterministic model, where a fixed concentration of stimulation of TRAIL is given, here, to investigate the effects of stochasticity in signaling reactions leading to variable cell survival and apoptosis responses in individual cells, three initializing conditions for low (1,000), medium (5,000), and high (20,000) copy numbers of TRAIL stimulation are chosen. As the model represents relative, rather than absolute, activation levels of signaling molecules, only the TRAIL copy numbers are initialized. The model will, therefore, show how the TRAIL molecular flux distributes stochastically through the downstream pathways over time.

For each initialization condition, 1,000 simulations representing 1,000 single-cell responses are performed. Figure 10.1a–c shows the resultant stochastic simulations,
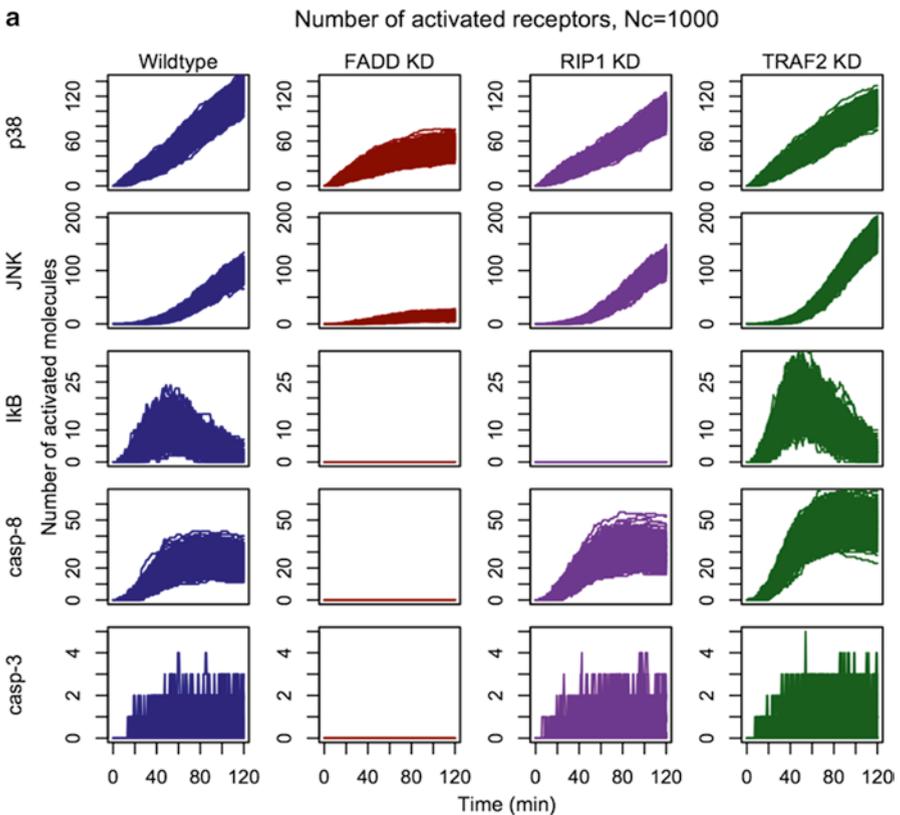
Fig. 10.1 *Stochastic simulations of tumor necrosis factor (TNF)-related apoptosis ligand (TRAIL) signaling*. Simulation profiles of p38, JNK, IκB, caspase-8, and caspase-3 in wild-type (*blue*), FADD KD (*brown*), RIP1 KD (*purple*), and TRAF2 KD (*green*) for 1,000 cells with low (1,000) (**a**), medium (5,000) (**b**), and high (20,000) (**c**) numbers of activated TRAIL receptors. Apart from the first reaction, TRAIL → TRAILR, where $V_{max} = 3 \times 10^{-11}$ M/s and $K_m = 1.5 \times 10^{-11}$ M were estimated based on experimental data [2] (see text), the reaction topology and all other parameters were obtained from Table 8.1 (see Chap. 8)

b Number of activated receptors, Nc=5000

c Number of activated receptors, Nc=20000
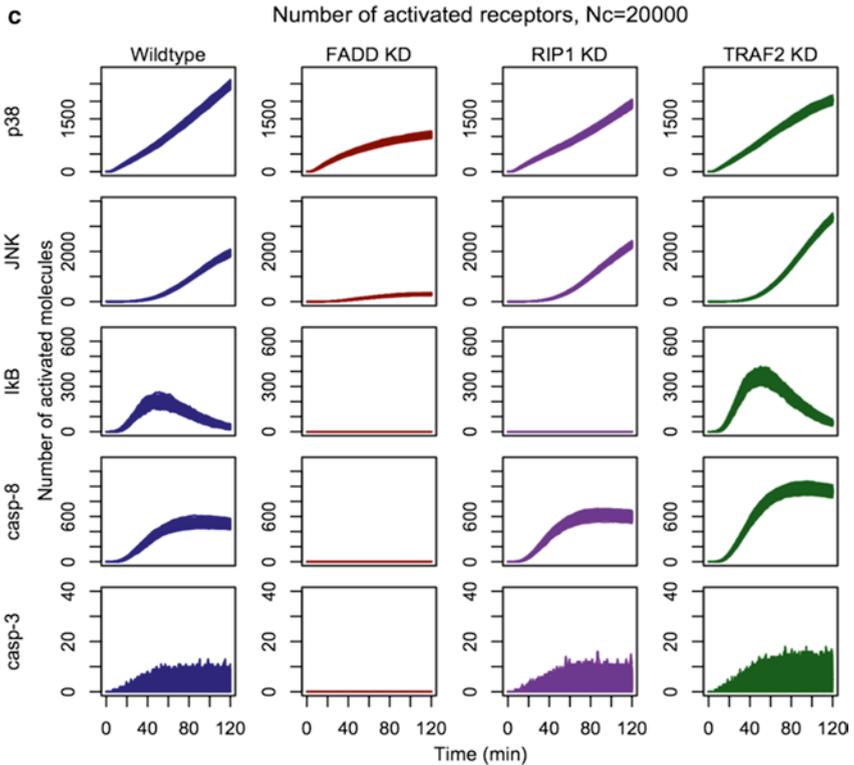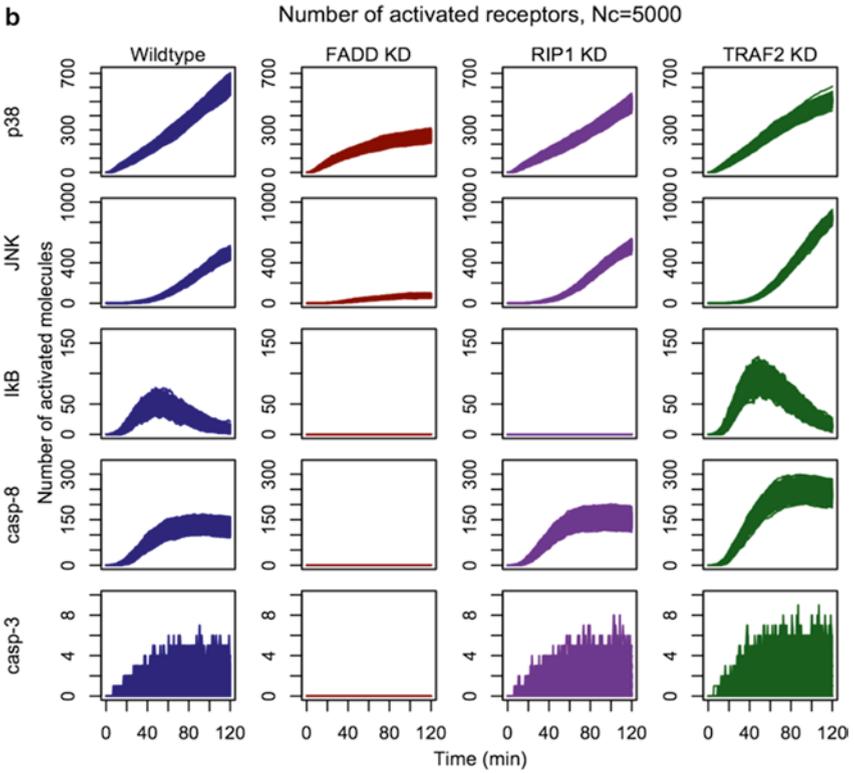
Fig. 10.1 (continued)
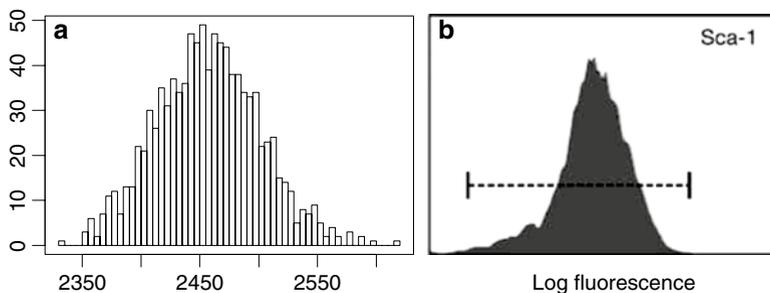
Fig. 10.2 *Gaussian-like distribution of signaling molecules*. (**a**) Distributions of simulated activation of p38 in wild-type condition for stimulation with 20,000 TRAIL molecules at $t = 120$ min. Similar distributions are obtained for all investigated molecules (data not shown) at all investigated conditions and concentrations. (**b**) Distribution representing the heterogeneity among clonal cells in *Sca-1* protein expression, from flow cytometry in murine erythroid myeloid lymphoid (EML) hematopoietic cells (Adapted from Chang et al. [3])

using reaction topology and most kinetic parameters from the deterministic TRAIL model (Chap. 8, Table 8.1), for cell survival (p38, JNK, IκB) and apoptosis (caspase-8 and -3) molecules.

Stochastic or noisy dynamics leading to variations in the temporal profiles for each of the 1,000 cells for IκB, JNK, p38, and caspase-8 and -3 in each condition are observed. As expected, the variability of all molecules between cells in all conditions is proportional to the number of receptors activated relative to the TRAIL concentrations, with a lower number showing noisier response (Fig. 10.1a, b) and a higher number converging toward the average cell response (Figs. 10.1c and 8.5a). Notably, the distribution of the activation of each molecule at any time point for all stimulation levels of TRAIL follows a Gaussian-like distribution. For example, Fig. 10.2a shows p38 at high numbers of TRAIL stimulation. Such distributions of activation profiles are consistent with the variability profiles of protein expressions observed for clonal populations of hematopoietic stem cells, such as for the *Sca-1* protein in single-cell measurements [3] (Fig. 10.2b).

Although the stochastic simulations demonstrate variability in signaling response, it is unclear how these results will affect overall cell survival or death for the various levels of TRAIL stimulations. Hence, similar to the deterministic TRAIL model in Chap. 8, the cell survival metric (*CSM*), based on the area under curve (*AUC*) between the cell survival and death molecules, and the survival ratio (*SR*) are utilized (see Eqs. 8.1, 8.2, 8.3, 8.4, 8.5, and 8.6, in Chap. 8). Here, the *CSM* and *SR* are investigated for 1,000 single cells at low, medium, and high TRAIL simulation, rather than for a population average where only a single *SR* at saturation TRAIL concentration (200 ng/mL) is used. For example, in the wild-type population, the SR_{WT} follows a hyperbolic profile with maximum apoptosis of 0.59 for TRAIL > 200 ng/mL (see Fig. 8.8b). This value is taken for high (20,000) TRAIL copy number stimulation (SR_{WThi}). For medium and low numbers, SR_{WTmed} and SR_{WTlow} are estimated to be 0.7 and 0.9, respectively, based on the hyperbolic plot.
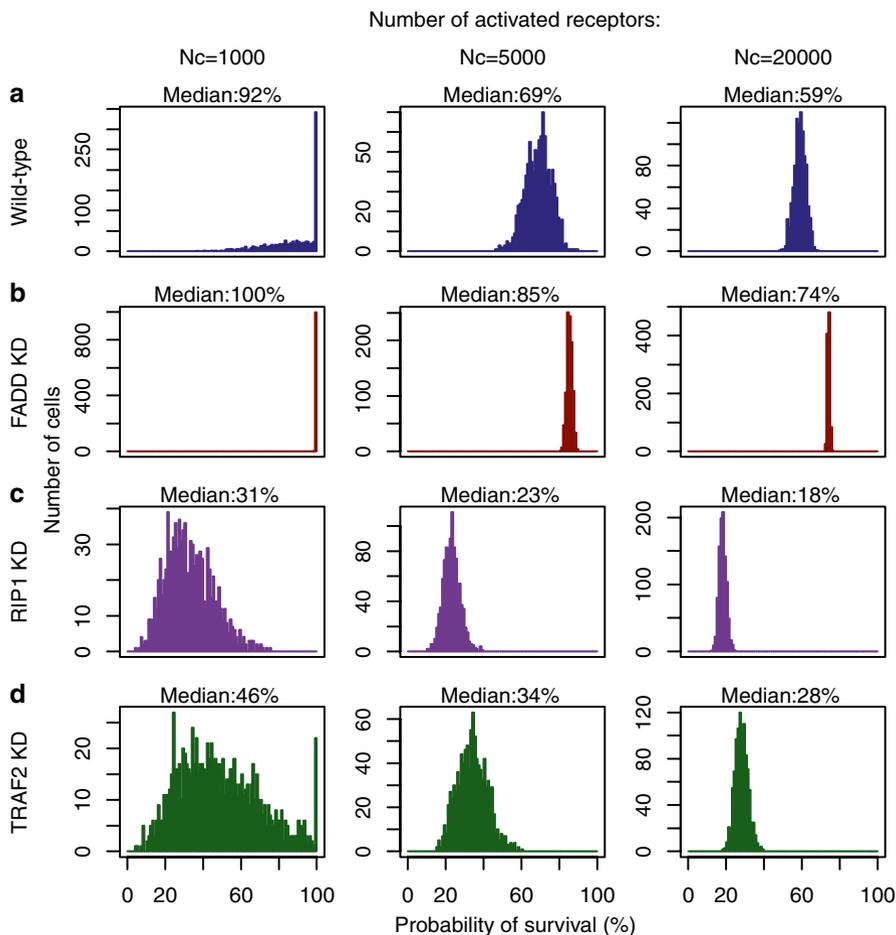
Fig 10.3 Probability of survival for single TRAIL-stimulated cells. Distribution of the probabilities of survival (*pS*) for single cells for 1,000 simulated cells in wild-type (**a**), FADD KD (**b**), RIP1 KD (**c**), and TRAF2 KD (**d**) after stimulation with low, medium, and high numbers of activated TRAIL receptors. The median *pS* is indicated at the *top* of each panel. It is important to note that *pS* is based on activation curves up to 120 min upon TRAIL stimulation, which may not take into account feedback mechanisms from autocrine or paracrine signaling

To distinguish single-cell response from population-average response, the *SR* is renamed to *pS* (probability of survival) as it is plotted as a distribution for each of the 1,000 single-cell simulations, rather than an individual average value (Fig. 10.3).

At low TRAIL stimulation, notably, FADD KD simulations indicate complete or deterministic survival of all cells, whereas the wild-type display 92 % surviving cells (Fig. 10.3a–b, left panels). For RIP1 KD and TRAF2 KD, however, the response is highly noisy with cells displaying a large variation in their survival or death capacity (Fig. 10.3c–d, left panels). These data indicate that, at low concentrations of TRAIL

stimulation, the stochasticity effects on cell survival become profound for RIP1 KD and TRAF2 KD, but not for wild-type or FADD KD. The mechanistic reason for this behavior could be their location at branching pathways, where the effect of *SFR* likely increases the variability in signaling flux (see Chap. 5). Thus, RIP and TRAF2 can be considered as noise-suppressing molecules in TRAIL signaling.

At medium TRAIL stimulation, the median cell survival decreases for all conditions, demonstrating the increased effectiveness of cell death through TRAIL. The FADD KD still maintain a more deterministic average response whereas RIP1 KD and TRAF2 KD show the most variable response, albeit less pronounced compared with low TRAIL stimulation. Finally, at high copy numbers of TRAIL, the simulated *pS* distributions show median values that are almost identical to average-response *SRs* (59 % for wild-type, 76 % for FADD KD, 18 % for RIP1 KD, and 28 % for TRAF2 KD). Moreover, the variation of *pS* become significantly less for all conditions compared to lower TRAIL stimulation. Thus, the lower effect of noise in cell signaling at higher concentrations of TRAIL leads to more a deterministic response by lowering variable response and, at the same time, increasing cell death.

To summarize, the effect of stochasticity on the response of HT1080 cancer cells stimulated with TRAIL is investigated. Using the cell population model for TRAIL signaling shown in Chap. 8, a single-cell stochastic response model based on the Gillespie algorithm is derived. The model is simulated 1,000 times to represent 1,000 single-cell responses in each experimental condition (wild-type, RIP1 KD, FADD KD, TRAF2 KD) for three stimulation levels of TRAIL receptors: low (1,000 copies), medium (5,000 copies), and high (20,000 copies). As expected, for higher number of activated TRAIL receptors, the stochastic simulations produced an overall result that is similar to the average population model shown in Chap. 8. With lower numbers of activated receptors, the variability of the signaling molecules becomes larger, especially for RIP1 and TRAF2 KDs, indicating that these molecules suppress stochastic noise in TRAIL signaling.

In all cases, the Gaussian-like spread around the median shows that even with stochastic variations in signaling, the median response of single cells globally follows the population-average dynamics of the deterministic model, especially when receptors are fully activated. This finding indicates that the effect of stochasticity in signaling networks may not be as 'fragile' to fluctuations as witnessed for nuclear transcriptional activation for cell fate decisions (Chap. 8). This effect occurs because cell signaling has been shown to display linear response, whereas cell fate decisions are governed by nonlinear behavior where it becomes sensitive to noise for tipping states [4]. In the future, the TRAIL model could be extended and exploited further for considering other sources of variability arising from extrinsic factors, such as unknown environmental factors and cell size. Such studies could improve the search for potential drug targets that enhance apoptosis of heterogeneous and resistant cancer cells.

Overall, this chapter highlights the necessity to understand variable responses of cell-signaling reactions to different levels of stochasticity. Thus, before the actual development of potential drug targets for killing cancer cells, the effect of stochastic variance could be investigated through dynamic perturbation-response models.

References

1. Gillespie DT (2007) Stochastic simulation of chemical kinetics. Annu Rev Phys Chem 58: 35–55
2. Varfolomeev E, Maecker H, Sharp D, Lawrence D, Renz M, Vucic D, Ashkenazi A (2005) Molecular determinants of kinase pathway activation by Apo2 ligand/tumor necrosis factor-related apoptosis-inducing ligand. J Biol Chem 280:40599–40608
3. Chang HH, Hemberg M, Barahona M, Ingber DE, Huang S (2008) Transcriptome-wide noise controls lineage choice in mammalian progenitor cells. Nature 453:544–547
4. Selvarajoo K (2012) Understanding multimodal biological decisions from single cell and population dynamics. Wiley Interdiscipl Rev Syst Biol Med 4:385–399

Chapter 11
The Distinction Between Single-Cell and Population Dynamics

The first eight chapters of this book focused on the population-level average cell dynamics, which can be modeled by linear response equations using simple rules on a macroscopic scale. In these dynamics, the parameters governing the reaction system are relatively insensitive to large variations in their outcome. However, any changes to the network structure or topology can produce drastic consequences. On the other hand, Chap. 9 introduced the issue of uncertainty at the microscopic scale where specific biological processes, such as cell fate decisions, require biological randomness or noise of single cells to determine the final outcome. So, do these data indicate that interaction between single cells when they form a cell population lead to a deterministic governing principle, as an emergent property, on a global scale?

Let us consider the movement of ants when building their nests (Fig. 11.1a). On a local scale, each ant makes a random walk. However, the communication between the ants through the use of a pheromone, a chemical factor secreted for social response, leads to collective behavior that develops a highly organized structure at a deterministic location. Similar behavior has also been observed in cells. The neurotransmitter protein GABA diffuses and interacts with randomly growing microtubules, leading to stability in growth rates and, subsequently, highly organized neurite protrusions are formed (Fig. 11.1b). Thus, local random interactions within a living system can lead to highly organized global structures.

To examine this point more scientifically, let us consider statistical analysis of a biological dataset. One simple, yet highly useful technique for searching global properties in high-throughput datasets is statistical correlation analysis. There are several kinds of correlation analyses that evaluate both linear (e.g., Pearson product–moment) and nonlinear (e.g., Spearman's rank, mutual information) dependencies [2, 3], and these have been widely and successfully used to observe global patterns of complex systems such as the weather, stock markets, and cosmology. In particular, the Pearson product–moment correlation, or simply Pearson's R, analysis has become most popular because of its ability to show
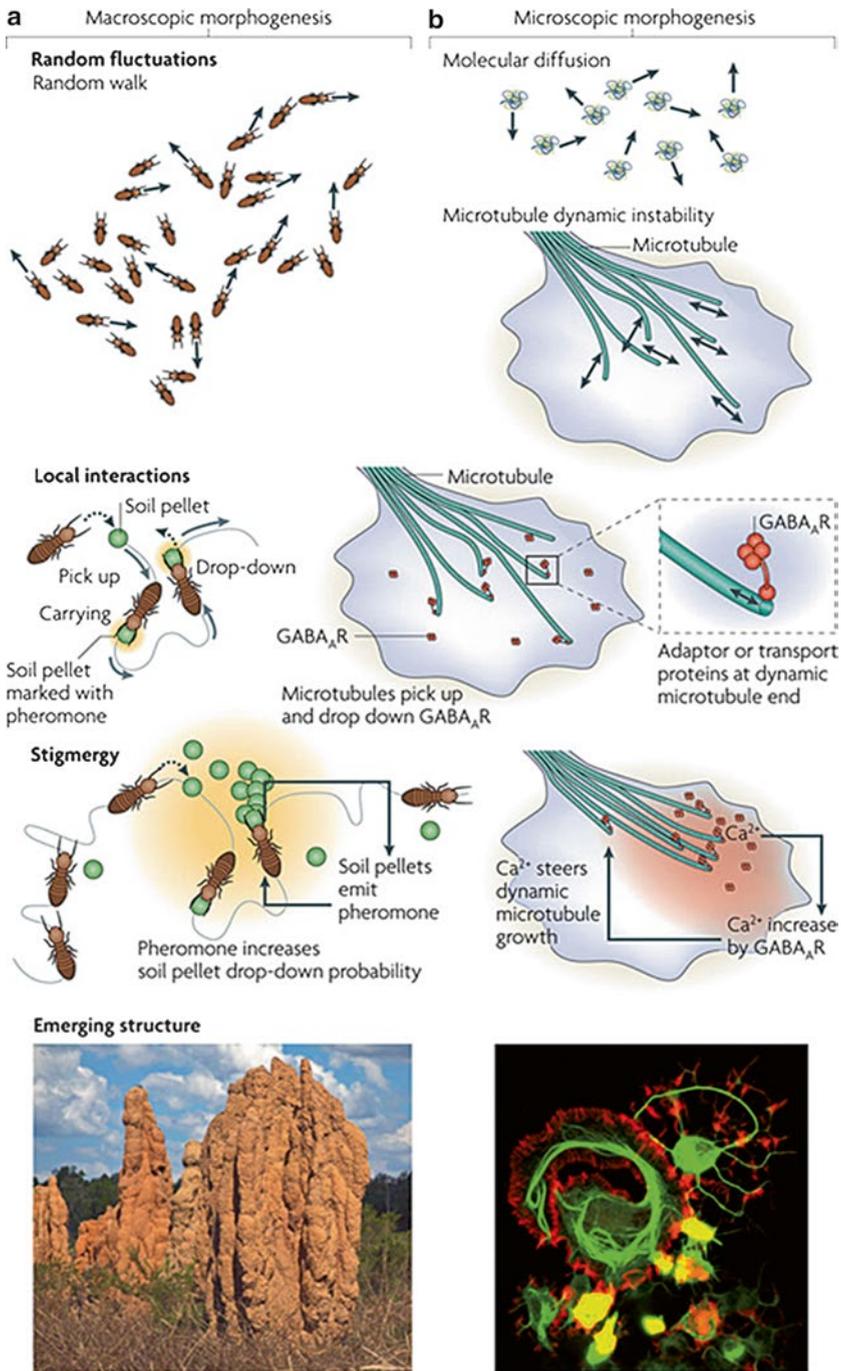
Fig. 11.1 *Self-organizing structures derived from random interactions*. (**a**) Random movement of an ant results in emergent nest formation by local interactions of ants that are guided through pheromones. (**b**) Formation of neurite protrusions by the local interactions of diffusing GABA$_A$ receptor with randomly growing microtubule in the growth cone (Adapted from Dehmelt and Bastiaens [1])

organizational structure in the simplest form. The Pearson correlation compares two samples or variables X and Y:

$$R = r(X,Y) = \frac{\sum_{i=1}^{N}(x_i - \mu_X)(y_i - \mu_Y)}{\sqrt{\sum_{i=1}^{N}(x_i - \mu_X)^2}\sqrt{\sum_{i=1}^{N}(y_i - \mu_Y)^2}} \tag{11.1}$$

where $X = (x_1,...,x_i,...,x_N)$ and $Y = (y_1,...,y_i,...,y_N)$ are $2N$-dimensional variables, x_i and y_i are the ith observation ($i=1,...,N$) of X and Y, respectively. μ_X and μ_Y are the statistical means of the two variables.

In biology, there have been numerous studies of Pearson correlations in gene and protein expression data. In theory, when two samples containing high-dimensional (such as microarray and proteomic) data are compared, the correlation analyses provide a measure of deviation from unity as a source of difference between the samples. Briefly, two samples with identical and completely nonidentical information will show unit ($R^2=1$) and null ($R^2=0$) correlation, respectively.

For single cells, stochastic fluctuations or intrinsic noise cause mRNA or protein expression to vary in time and between cells (see Chap. 9). Figure 11.2a (left panel) compares two theoretical samples where the individual expression level of each species is generated using the Poisson (stochastic) process. Although the overall sample correlation is high ($R^2=0.98$), species with low copy numbers show significantly lower correlations (e.g., $R^2<0.15$ for $\log(X)<2$). Correspondingly, when noise ($\eta^2 = \sigma^2_{XY} / \mu^2_{XY}$) is quantified, it becomes evident that an intrinsic factor (Poisson process) is the key for generating noise at low expressions, whereas at higher expressions, the noise reduces and approaches zero (Fig. 11.2c, left panel).

Apart from stochasticity, other sources of biological noise can be lumped into extrinsic factors: these include variability in cell size, molecular copy numbers, and environmental fluctuations between individual cells. These factors distort the deterministic response and alter strong correlations into weaker ones (Fig. 11.2a, middle panel). However, in contrast to intrinsic noise, extrinsic noise is not lowered at high expression levels (Fig. 11.2c, middle panel). Notably, when investigating actual single-cell mRNA comparison between two oocytes, the resultant correlation structure displayed stochastic noise as the dominant noise source (Fig. 11.2a, c, right panel).

For cell populations, both the intrinsic and extrinsic noise is reduced (Fig. 11.2b, c, left and middle panels), possibly because of the canceling of positive and negative noise across all range of molecular expressions. Such a phenomenon is also observed for an actual mouse fibroblast (NIH/3 T3) cell culture (Fig. 11.2b, c, right panels). Hence, reduction of biological noise occurs in cell populations, and this reveals the deterministic average response.

To further emphasize cell population determinism, let us look at another example. In a laboratory experiment on a microbial closed system with well-controlled initial conditions, several individual systems of three species (*Chlamydomonas reinhardtii*, *Escherichia coli*, and *Tetrahymena thermophila*) were analyzed for growth behavior over 90 days (Fig. 11.3a) [5]. Although individual system
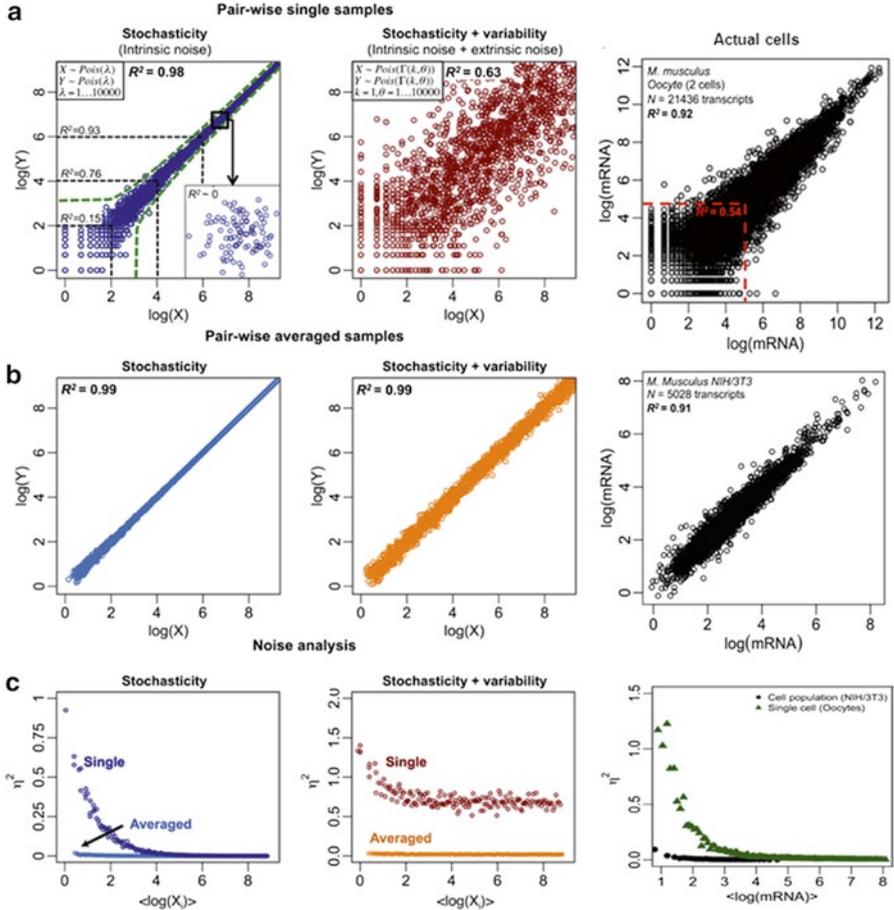
Fig. 11.2 *Biological and nonbiological noise reduces the between-samples correlation structure.* (**a**) *Left*: Stochastic fluctuation lowers correlation, especially for low copy number of molecular species ($R^2 \sim 0.15$ for $\log(X) < 2$). *Green dotted lines* represent the intrinsic noise region generated by Poisson process. *Insert:* The correlation structure disappears when zooming at smaller or single molecule scale. *Middle*: Stochastic fluctuations (intrinsic) on variable (extrinsic) noise reduce the overall correlation structure. Variable noise is represented by gamma distribution. *Right*: mRNA expressions between two oocytes (single cells). *Red dotted lines* indicate regions of low mRNA expression [$\log(\text{mRNA}) < 5$]. (**b**) Stochastic (*left*) and total (stochastic and variable) (*right*) noise are reduced when single samples are averaged into a population. (**c**) Noise, $\eta^2 = \sigma^2_{XY} / \mu^2_{XY}$, versus $<\log(X_i)>$ for stochastic process (*left*), stochastic and variable (*middle*), and actual cells (*right*, with oocytes in *green triangles* and NIH/3 T3 as *black dots*). $\sigma_{XY} = \sqrt{\frac{1}{2P} \sum_{j=1}^{P} (x_{i,j} - y_{i,j})^2}$, $\mu_{XY} = \frac{1}{2P} \sum_{j=1}^{P} (x_{i,j} + y_{i,j})$, and the *j*th element of vectors $X_i = (x_{i,1}, ..., x_{i,j}, ..., x_{i,P})$ and $Y_i = (y_{i,1}, ..., y_{i,j}, ..., y_{i,P})$. is the expression of the *i*th gene in the *j*th sample for P (= 100) pairs of samples (Adapted from Piras et al. [4])
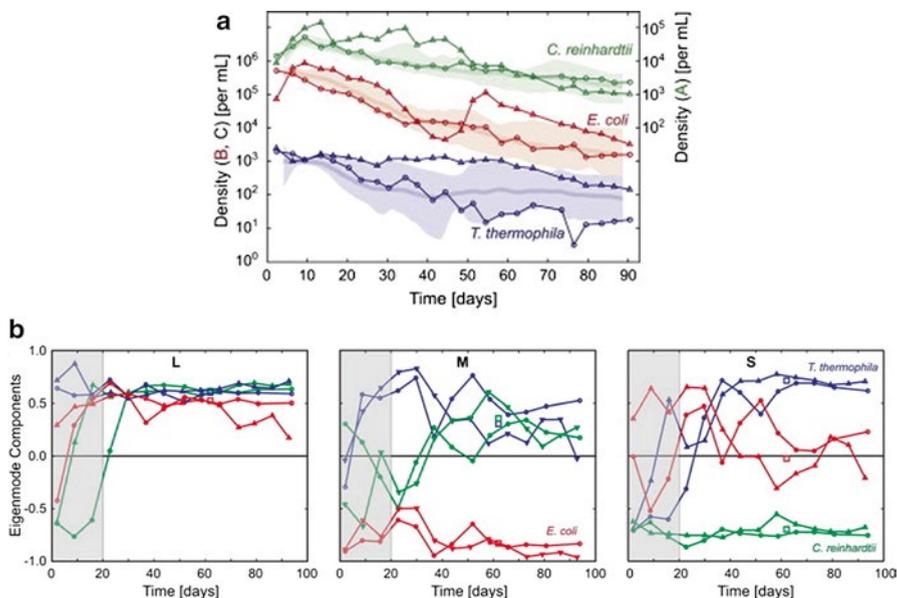
Fig. 11.3 *Complex ecosystem dynamics and ecomodes.* (**a**) Population dynamics of *Chlamydomonas reinhardtii*, *Escherichia coli*, and *Tetrahymena thermophila* kept under constant light and temperature. (**b**) Ecomodes *L*, *M*, and *S* labeled according to their corresponding eigenvalues labeled *L*, *M*, and *S* (Adapted from Hekstra and Leibler [5])

displayed variability in their dynamics, the variations between the three species correlated (Fig. 11.3b). Notably, their covariation showed a stable structure that was decomposed into "ecomodes," where the largest ecomode follows the population-average dynamics. Furthermore, the fluctuations around the average dynamics displayed a power law consistent with geometric random walk. Thus, despite variability at the individual level, average deterministic population dynamics are observed for all three species investigated.

Recent single-cell analyses displaying biological complexity such as heterogeneity and fluctuations or noise are important new discoveries. However, from the examples from this chapter, we do need to accept that biology, similar to any other complex system, possesses both microscopic (single-cell) and macroscopic (population-average cell) dynamics. It is necessary to treat the two dynamics as distinct and to investigate their individual merits. As briefly discussed in Chap. 9, stochastic fluctuations are necessary to induce probabilistic differentiation from genetically identical cells, allowing multicellular organisms to switch fates and states to yield diversity, such as for development or stress, which otherwise may be impossible from a purely deterministic system. On the other hand, the well-coordinated response of cell populations, such as differentiation or growth, demonstrates that the single-cell noise cancels out when ensembles of cells are formed to

generate a stable and robust response. The observation of guided average behavior in the synchronization of neuronal signaling and the persistence mechanisms of bacteria are other noteworthy examples [6, 7].

Therefore, as observed in other physical sciences, biology is a system that possesses both microscopic and macroscopic dynamics. For example, in the study of fluid dynamics, at the microscopic level we observe the motion of each individual particle to be highly random and unpredictable. However, at a macroscopic level, airflow velocity follows the fundamental law of fluid mechanics (the law of conservation of mass, energy, and momentum). Thus, it is necessary to treat the two dynamics separately.

It is also interesting to ponder the origins of averaging effect from stochastic response of a single cell when ensembles of cells form a population. The emergence of average cell deterministic response from single-cell stochastic response may likely complement each other.

Thus, the search for governing laws arising from single-cell dynamics will enable us to better understand the coordinated response of cell populations. Most importantly, finding the connection between microscopic and macroscopic dynamics and the unifying laws are crucial for understanding the origins of evolutionary and developmental robustness of living systems.

References

1. Dehmelt L, Bastiaens PI (2010) Spatial organization of intracellular communication: insights from imaging. Nat Rev Mol Cell Biol 11:440–452
2. Rosner B (2011) Fundamentals of biostatistics, 7th edn. Duxbury Press, Boston
3. Steuer R, Kurths J, Daub CO, Weise J, Selbig J (2002) The mutual information: detecting and evaluating dependencies between variables. Bioinformatics 18(suppl 2):S231–S240
4. Piras V, Tomita M, Selvarajoo K (2012) Is central dogma a global property of cellular information flow? Front Physiol 3:439
5. Hekstra DR, Leibler S (2012) Contingency and statistical laws in replicate microbial closed ecosystems. Cell 149:1164–1173
6. Pasquale V, Massobrio P, Bologna LL, Chiappalone M, Martinoia S (2008) Self-organization and neuronal avalanches in networks of dissociated cortical neurons. Neuroscience 153:1354–1369
7. Smith PA, Romesberg FE (2007) Combating bacteria and drug resistance by inhibiting mechanisms of persistence and adaptation. Nat Chem Biol 3:549–556

Chapter 12
Finding Chaos in Biology

The preceding chapters have indicated that biology should be appreciated from both microscopic (uncertainty) and macroscopic (certainty) perspectives. For instance, although the control of stochasticity led to a distinct cell fate in the competence of *Bacillus subtilis* and incomplete penetrance of *Caenorhabditis elegans*, the nuclear reprogramming by eggs and oocytes is deterministic, as it occurs in an ordered and precise timing [1]. Furthermore, the early events of reprogramming mouse embryonic fibroblasts to pluripotency factor colonies also showed deterministic, rather than stochastic, steps [2]. In contrast to probability theories, these works suggest that well-defined deterministic processes must exist within the noisy cellular environment. Hence, the circumstances in which cells utilize noise (single cell) on the deterministic (population) process remains unclear. As such, it is worthwhile to investigate further underlying mechanisms, apart from causal networks shown in Chap. 8, which could utilize biological noise to change decisions.

In physics, the chaos theory appreciates the complexity in natural systems and attempts to formulate it using simple rules. Today, its utility is recognized in diverse systems such as weather, natural structures, the economy, and the stock market. The discovery of the chaos concept has not been fully attributed to one person. Although it was Henri Poincare, a mathematician, who originally proposed the phenomenon of chaos, through phase–space plots in 1889 [3], the person to be recognized as the 'father' of chaos is Edward Lorenz. Lorenz is credited for his elegant demonstration of the existence of deterministic patterns from a highly nonlinear weather system from experimental, theoretical, and computational aspects [4, 5].

Lorenz created a simple model for studying atmospheric conditions and found that results from the simulations were not reproducible each time. He initially believed that this was a mistake in the model. Subsequently, he considered that it was caused by low decimal round-off errors introduced by numerical schemes used to linearize the convection equation of the 1960s computer that resulted in the variability of the results of each run. More careful analysis later revealed that his atmospheric model is sensitive to small changes in model parameters (Fig. 12.1a, b), and he was convinced that something else might exist that is not quite well understood.
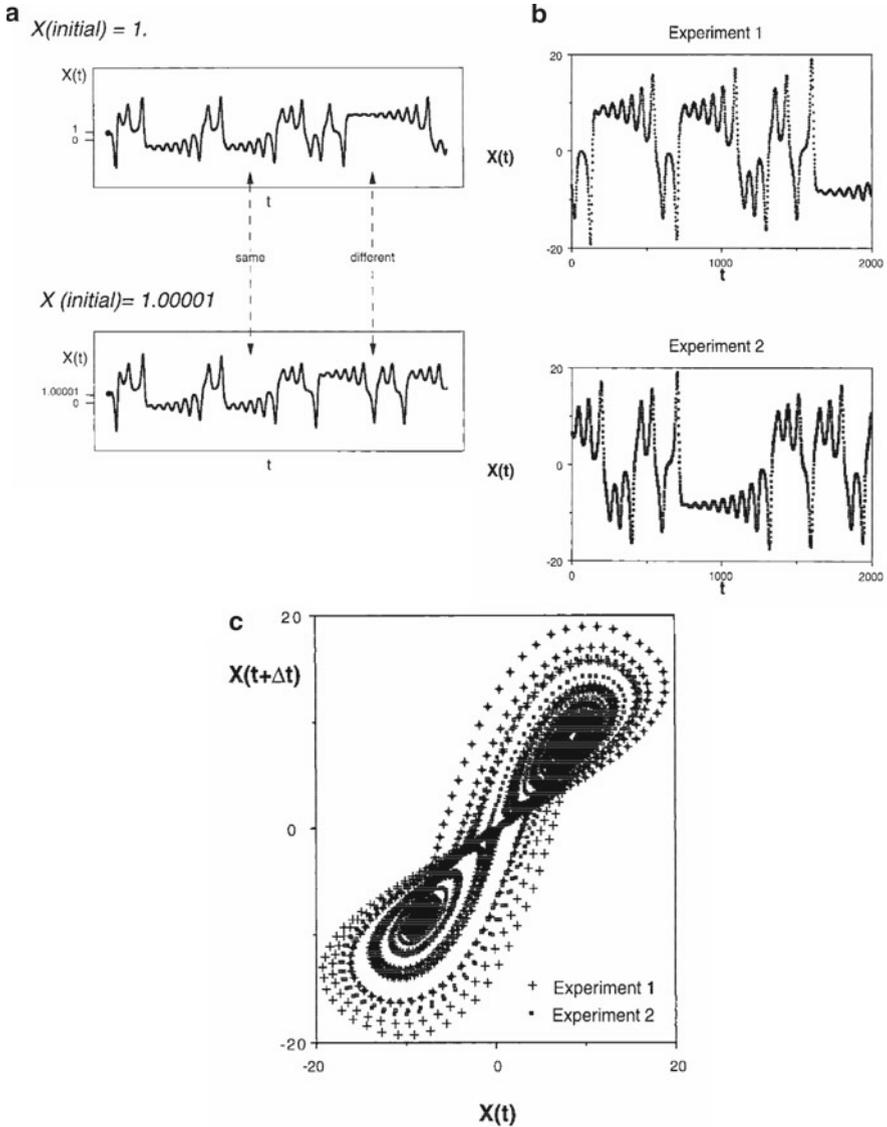
Fig. 12.1 *Chaos dynamics.* Simulations of Lorenz atmospheric model. (**a**) Initial values of $X=1$ and 1.00001 yield very different values over time, demonstrating sensitivity to initial conditions. (**b**) Different initial values of X show very different time-series pattern. (**c**) The phase–space plot $(X(t+\Delta t))$ versus $(X(t))$ of the Lorenz model shows clear patterns despite being sensitive to initial conditions in time-series plots (From Liebovitch and Scheurle [6])

How could a model based on a fixed governing master equation be so unstable to linearization schemes?

When visualizing his result on a time-series scale, each simulation, within a sensitive parameter region, produced unstable response. However, when the overall results were transformed into a phase–space plot (introduced by Poincare), clear patterns of the "unstable" behavior appeared with a core region, called the 'attractor,' around which the solution tracks (Fig. 12.1c). Thus, the stability, through the presence of an attractor, of the atmospheric model simulations is revealed in a phase–space plot, not in a time-series, and this simple transition enabled seeing deterministic patterns from chaotic responses.

Today, there are several characteristics that a chaotic system is known to possess. (1) *Attractors*: when a system is perturbed, it evolves toward certain steady states. This response could be the return to the original state, or to a new state. Regular pendulum movements and circadian rhythms are good examples of attractors. Attractors can be fixed point, limit cycle, strange, or chaotic. (2) *Sensitive to initial conditions*: this is sometimes referred to as the butterfly effect. Any changes to the initial conditions can create very drastic changes to the final response. (3) *Fractals or self-similarity*: the scalable structure seen across the entire geometric construct. That is, as we go deeper and deeper into a chaos, we realize that the smallest structure resembles that of the overall structure. (4) *Bifurcations*: the abrupt changes to system dynamics at specific point(s). (5) *Plasticity*: the ability to achieve multiple stable states to the system perturbations; for example, the self-organization of bacteria (individual) to form biofilms (population structure) when exposed to threats. (6) *Feedback loops*: information from one time point to the next could be fed back to the system for robustness to changing conditions. That is, system dynamics or trajectory is controllable by a feedback system. (7) *Phase locking*: the process when an individual diversion in a population could lead to a global shift in population behavior. A shoal of tuna responding to attacks from whales is an example.

Attractors

Attractors are used to describe systems that evolve toward a specific state set by the initial conditions. To examine attractors in biology, high-dimensional gene expression analysis was performed for the differentiation of human pro-myelocytic leukemia HL-60 cells into neutrophils by the action of two different reagents, dimethyl sulfoxide (DMSO) and all-*trans* retinoic acid (atRA) [7]. The time-course investigations showed the convergence of cell differentiation despite different initial transcriptome dynamics, demonstrating the existence of attractors for a preferred cell fate (Fig. 12.2a). Subsequently, another investigation sorting mouse hematopoietic cell lines into distinct concentrations (low, medium, and high) of the stem cell-surface marker *Sca-1* reestablished the parental clonal heterogeneity
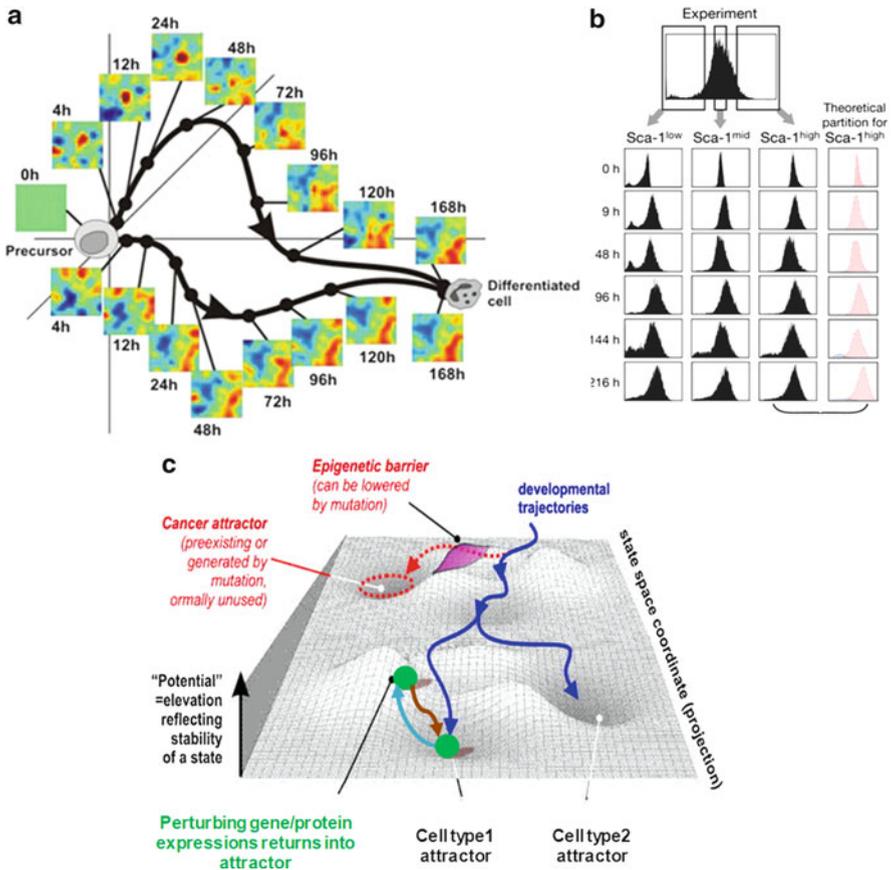
Fig. 12.2 *Attractor states in biology.* (**a**) The convergence of gene expression patterns, using clustering statistics, reflects the same cell fate attractor to distinct stimulation of atRA and DMSO (Courtesy of Sui Huang.) (**b**) Reestablishment of the parental state of clonal cells after 216 h of cell culture despite distinct initial expression of Sca-1 (*low, medium, high*) in a mouse hematopoietic cell line (Adapted from Chang et al. [8]). (**c**) Schematic three-dimensional (3-D) landscape for cellular attractors. Each *hole* represents a distinct attractor, such as a cell type or cancer subtype (Modified from Huang et al. [9])

profiles (Fig. 12.2b). More recently, human cancer cell lines showed that sorting cells into distinct phenotypes (stem-like, basal, and luminal) from the parental population also returned the daughter subpopulations that resembled the parental population over time [10]. These data suggest the presence of strong equilibrium or attractor states in cell populations, whereby sorted (perturbed) subpopulations eventually return to their original state (Fig. 12.2c).

Self-Similarity and Patterns

In cancer, the comparison of individual molecules between normal and disease often leads to information that is highly variable and difficult to be conclusive. It is often the case that physicians are unable to detect cancers in early stages when analyzing a few molecules at a time (biomarkers). In a human lung cancer study, a self-organizing map (SOM)-based statistical clustering technique was used to analyze the microarray data of several tumor types [11]. Remarkably, the SOM approach resulted in clear visual global gene expression patterns corresponding to distinct tumor subtypes of three randomly chosen individuals (Fig. 12.3a). Thus, despite the individual variability, the use of a statistical algorithm on a global scale allows one to detect the relationships between datasets, thereby revealing the presence of distinct cancer attractors and subtypes.

In observing whole genome expression patterns to innate immune response, the Toll-like receptor 4 (TLR4) stimulation of murine macrophages in 12 experimental readouts (i.e., four genotypes at three time points)—wild-type, MyD88 knockout (KO), TRIF KO, and MyD88/TRIF double KO (DKO)—at 0, 1, and 4 h was investigated [12, 13]. Temporal Pearson correlation analysis (see Chap. 11) on the whole genome (more than 20,000 genes/ORFs) was performed. To investigate whether 'scalability' or self-similarity of a gene expression network exists, a random selection of 100 genes (repeated 30 times) was analyzed and compared with the whole genome response for the four genotypes. Figure 12.3b shows that the temporal correlations of the random extraction followed the small, but reliable and monotonically related to time, departure from unit correlation, pointing to similarity to the whole genome response. This pattern between the whole and random grouping of genes, however, was absent for a selected 157 proinflammatory genes, especially in DKO where the monotonic response is almost absent. Thus, TLR4-induced gene expression shows self-similar structures found in chaos.

In another study relevant to TLR4 stimulation, the tracking of about 3,000 genes over longer periods (up to 24 h) in wild-type macrophages revealed coordinated dynamics among specific clusters of genes that became active at different times [14]. The subnetworks of genes are connected with master or 'hub' genes, comprising mainly the well-known transcription factors of diverse cellular processes (e.g., ATF-3, NRF-2, ETS) into a scale-free topology, providing the means for the genomic order of TLR4 response. Pondering deeper into genome character, it has been shown for hematopoietic progenitor cell differentiation that gene coregulation moves from ordered to disordered and then returns to the ordered entropy state over several days, through the self-organizing lineage-specific chromosomal networks [15]. Overall, these investigations show biology as a system that resembles the characteristics of chaos theory, that is, the presence of order from what apparently seems to be unpredictable or random information.
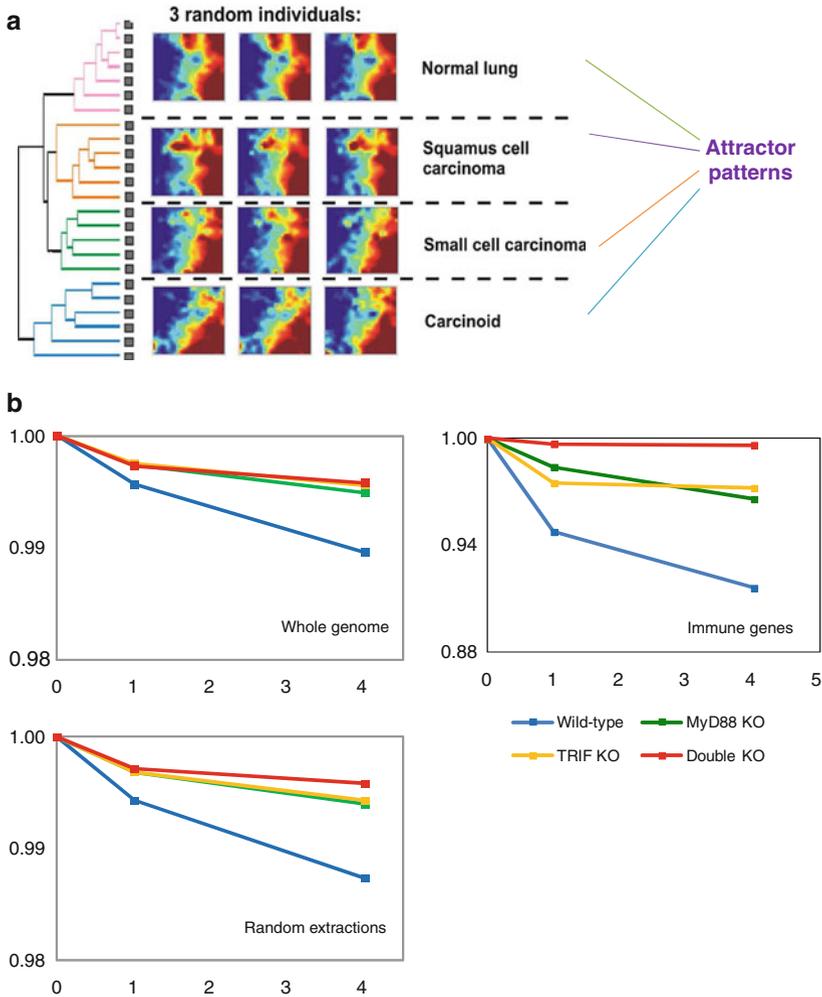
Fig. 12.3 *Self-organizing patterns and scalability*. (**a**) The emergence of distinct clustering patterns in lung tumor transcriptome data. Despite variation between individual gene readouts, the global analysis reveals a clear attractor pattern for each cancer subtype (Adapted from Guo et al. [11]). (**b**) Scalable gene expression response. Temporal Pearson (auto)-correlations of whole genome (*top left*), random extractions of 100 genes (*bottom left*), and 157 immune-related (IR) genes (*top right*). In DKO, the response is abolished for IR genes but not for random genes. The random extractions were repeated 30 times, yet displayed a similar structure with the whole genome for all genotypes (From Tsuchiya et al. [12, 13]

Sensitivity to Initial Conditions or Noise

Chaos is also characterized by its high sensitivity to initial conditions, resulting in divergent outcomes. The study of weather patterns showed that the addition of a small periodic signal to a dynamic system that presents stochasticity amplified the original signal, resulting in multistable states [16]. This phenomenon was termed stochastic resonance (*SR*) [17]. It follows that only when the signal-to-noise ratio reaches approximately a threshold level that such state changes occur (Fig. 12.4). Just as the periodic signal is crucial in *SR* for drastic weather changes that occurred over historical periods, for multifaceted decisions in biology, it is necessary for us to understand the underlying mechanisms (or governing principles) that convert stochastic or noisy response into binary or multiple outputs.

The concept of *SR* has been tested in biology. In neuroscience, the interspike intervals of periodically stimulated sensory neurons are multimodal. To uncover the mechanisms for the distribution behind the dynamics of bistability and excitability in neurons, Longtin [20] used a FitzHugh–Nagumo model, a simplified version of the Hodgkin–Huxley model [21], and showed that noise on additive periodic forces is crucial to generate a multimodal distribution of interspike intervals of neurons firing to a specific phase of the input signal. Although the model could not fully interpret the peak heights of the spikes, nevertheless it demonstrated neuron firing activity is positively governed by a simple nonlinear model, with *SR* phenomenon controlling the multimodal response.
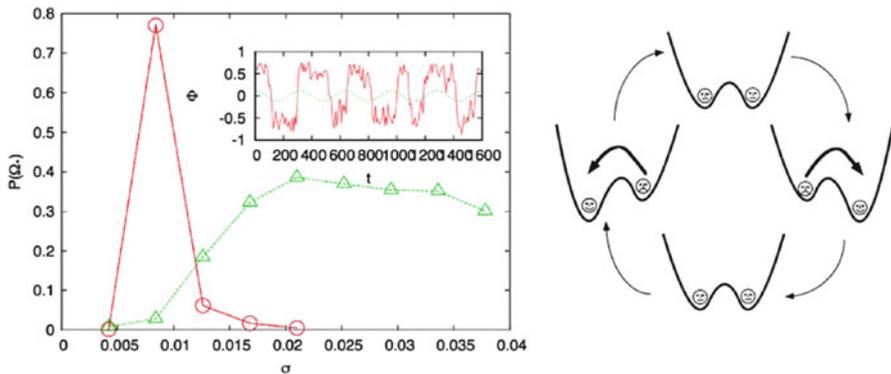
Fig. 12.4 *Stochastic resonance.* Consider a dynamic system governed by $dx/dt = V(x) + A\cos(\omega t) + \xi(t)$, where *V(x)* is a generic nonlinear expression of *x*, *Acos(ωt)* is an oscillatory periodic force with frequency *ω*, and *ξ(t)* represents a noise function (such as Gaussian white noise) [18]. Taking $V(x) = \alpha\psi - \psi^3$ and $\xi(t) = \sigma^{1/2}\eta(t)$, it can be shown for $A = 0.023$, $2\pi/\omega = 1{,}600$ and the modulation of noise within a threshold range $(0.005 < \sigma < 0.015)$ produces bistable states (*left*), which could statistically switch orientations between the two stable states (*right*). Note that *P(ω)* is the power spectrum of *ω* (see [19] for details and for other multistable states) (Adapted from Benzi [19])
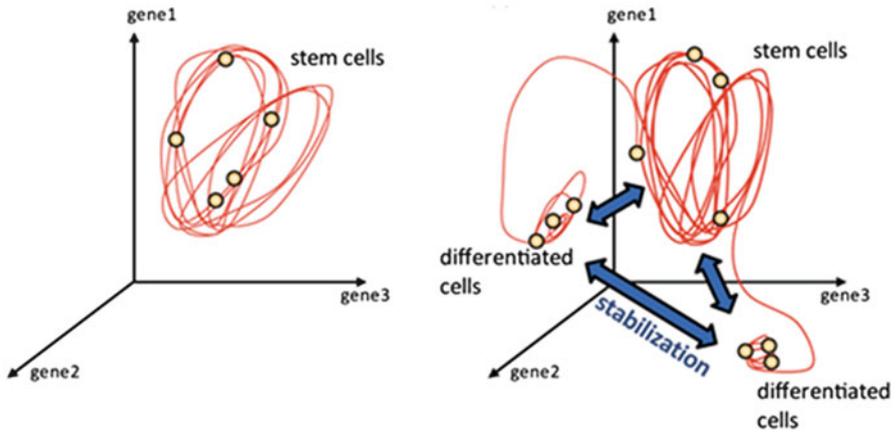
Fig. 12.5 *Schematic state–space plots of stem cell differentiation.* Gene expression variation in undifferentiated stem cells (*left*) compared with noise-induced differentiation (*right*). *Right panel* shows the stabilization in gene expression localization for each differentiated state, revealing attractor states (Adapted from Suzuki et al. [22])

The sensitivity to noise for stem cell differentiation was recently investigated with the aid of a dynamic computational model [22]. To understand the fundamental mechanisms for stemness and plasticity in multipotent stem cell differentiation, dynamic gene regulatory network (GRN) models using simple nonlinear equations that considered cell-to-cell interaction and the effects of heterogeneity were developed. Notably, among more than a 100 million GRNs tested, GRNs that produce oscillatory protein expression dynamics and whose synchronies are lost between cells were shown to be crucial for stem cell differentiation and proliferation. This result, which is in agreement with experimental observations [23, 24], indicates that the complex process of cell differentiation may be regulated by GRNs governed by simple nonlinear reactions that produce multistable outcomes (attractors) when biological noise in terms of stochasticity or heterogeneity is added (Fig. 12.5).

In summary, the examples presented so far demonstrate that biology possesses several characteristics of a chaotic system that can operate far from equilibrium: (i) biological noise can destabilize original steady states and induce transitions for new regularity in a time-dependent manner [25–28], for example, in the bifurcations of comK expressions [29]; (ii) cell differentiation and synaptic transmission processes have been shown to cross the barrier between stable attractors by noise [30, 31]; (iii) the robustness of several key processes to biochemical variation was witnessed in bacterial chemotaxis [32]; (iv) bimodality behavior in yeast required noise on a feedback mechanism [33]; (v) phase locking of bacteria was seen in biofilm formation [30]; and (vi) suppression of bursting mRNA moved into ordered decision in a yeast transcriptional system [33]. These properties, collectively, enable biology to attain a multiple but finite number of attractor states.

References

1. Jullien J, Pasque V, Halley-Stott RP, Miyamoto K, Gurdon JB (2011) Mechanisms of nuclear reprogramming by eggs and oocytes: a deterministic process? Nat Rev Mol Cell Biol 12:453–459
2. Smith ZD, Nachman I, Regev A, Meissner A (2010) Dynamic single-cell imaging of direct reprogramming reveals an early specifying event. Nat Biotechnol 28:521–526
3. Poincaré H (1899) Les méthodes nouvelles de la méchanique céleste, vol III. Gauthiers, Paris
4. Lorenz E (1995) The essence of chaos, The Jessie and John Danz Lecture Series. University of Washington Press, Seattle
5. Lorenz E (1963) Deterministic nonperiodic flow. J Atmos Sci 20:130–148
6. Liebovitch LS, Scheurle D (2000) Two lessons from fractals and chaos. Complexity 5:34–43
7. Huang S, Eichler G, Bar-Yam Y, Ingber DE (2005) Cell fates as high-dimensional attractor states of a complex gene regulatory network. Phys Rev Lett 94:128701
8. Chang HH, Hemberg M, Barahona M, Ingber DE, Huang S (2008) Transcriptome-wide noise controls lineage choice in mammalian progenitor cells. Nature 453:544–547
9. Huang S, Ernberg I, Kauffman S (2009) Cancer attractors: a systems view of tumors from a gene network dynamics and developmental perspective. Semin Cell Dev Biol 20:869–876
10. Gupta PB, Fillmore CM, Jiang G, Shapira SD, Tao K, Kuperwasser C, Lander ES (2011) Stochastic state transitions give rise to phenotypic equilibrium in populations of cancer cells. Cell 146:633–644
11. Guo Y, Eichler GS, Feng Y, Ingber DE, Huang S (2006) Towards a holistic, yet gene-centered analysis of gene expression profiles: a case study of human lung cancers. J Biomed Biotechnol 2006:69141
12. Tsuchiya M, Piras V, Choi S, Akira S, Tomita M, Giuliani A, Selvarajoo K (2009) Emergent genome-wide control in wild-type and genetically mutated lipopolysaccharides-stimulated macrophages. PLoS One 4:e4905
13. Tsuchiya M, Selvarajoo K, Piras V, Tomita M, Giuliani A (2009) Local and global responses in complex gene regulation networks. Physica A 388:1738–1746
14. Nilsson R, Bajic VB, Suzuki H, di Bernardo D, Björkegren J, Katayama S, Reid JF, Sweet MJ, Gariboldi M, Carninci P, Hayashizaki Y, Hume DA, Tegner J, Ravasi T (2006) Transcriptional network dynamics in macrophage activation. Genomics 88:133–142
15. Rajapakse I, Perlman MD, Scalzo D, Kooperberg C, Groudine M, Kosak ST (2009) The emergence of lineage-specific chromosomal topologies from coordinate gene regulation. Proc Natl Acad Sci USA 106:6679–6684
16. Nicolis C, Nicolis G (1981) Stochastic aspects of climatic transitions—additive fluctuations. Tellus B 33:225–237
17. Benzi R, Parisi G, Sutera A, Vulpiani A (1982) Stochastic resonance in climatic change. Tellus B 34:10–16
18. Gammaitoni L, Hänggi P, Jung P, Marchesoni F (1998) Stochastic resonance. Rev Mod Phys 70:1223–1287
19. Benzi R (2009) Stochastic resonance in complex systems. J Stat Mech 1:1052
20. Longtin A (1993) Stochastic resonance in neuron models. J Stat Phys 70:309–327
21. Hodgkin A, Huxley A (1952) A quantitative description of membrane current and its application to conduction and excitation in nerve. J Physiol 117:500–544
22. Suzuki N, Furusawa C, Kaneko K (2011) Oscillatory protein expression dynamics endows stem cells with robust differentiation potential. PLoS One 6:e27232
23. Lander AD, Gokoffski KK, Wan FY, Nie Q, Calof AL (2009) Cell lineage and the logic of proliferative control. PLoS Biol 7:e1000015
24. Kirouac DC, Madlambayan GJ, Yu M, Sykes EA, Ito C, Zandstra PW (2009) Cell–cell interaction networks regulate blood stem and progenitor cell fate. Mol Syst Biol 5:293
25. McAdams HH, Arkin A (1997) Stochastic mechanisms in gene expression. Proc Natl Acad Sci USA 94:814–819

26. Rao CV, Wolf DM, Arkin AP (2002) Control, exploitation and tolerance of intracellular noise. Nature 420:231–237
27. Capp JP (2005) Stochastic gene expression, disruption of tissue averaging effects and cancer as a disease of development. Bioessays 27:1277–1285
28. Hornung G, Barkai N (2008) Noise propagation and signaling sensitivity in biological networks: a role for positive feedback. PLoS Comput Biol 4:e8
29. Maamar H, Raj A, Dubnau D (2007) Noise in gene expression determines cell fate in *Bacillus subtilis*. Science 317:526–529
30. Ribrault C, Sekimoto K, Triller A (2011) From the stochasticity of molecular processes to the variability of synaptic transmission. Nat Rev Neurosci 12:375–387
31. Lee HH, Molla MN, Cantor CR, Collins JJ (2010) Bacterial charity work leads to population-wide resistance. Nature 467:82–85
32. Alon U, Surette MG, Barkai N, Leibler S (1999) Robustness in bacterial chemotaxis. Nature 397:168–171
33. To TL, Maheshri N (2010) Noise can induce bimodality in positive transcriptional feedback loops without bistability. Science 327:1142–1145

Chapter 13
Concluding Remarks

We have come to the end of this introductory book on immune cell signaling from a systems biology perspective. Chapters 1, 2, 3, 4, 5, 6, 7, and 8 have highlighted that biological pathways are guided by deterministic response waves at the cell population level. These response waves can be modeled using the perturbation-response approach utilizing first-order mass-action equations. From the examples of TLRs, TNF, and TRAIL signaling, it is shown that network topology, rather than reaction parameter values, is crucial for interpreting complex signaling dynamics. In other words, from population cell-average dynamics, we observe simple statistical laws, such as linear response and power law, which are important to shape global response. In this book, several feedback mechanisms in the immune signaling were skipped as the experimental data available for analysis were limited. Nevertheless, many of the simulations are still consistent with the overall experimental outcome.

Chapters 9, 10, 11 and 12 introduce the significance of recent single-cell and single-molecule investigations, where biological noise, such as stochastic molecular interactions and cell-to-cell variability, initiate uncertainty in responses crucial for multimodal cellular decisions. There are also indications for behaviors in biology that resemble chaotic systems through attractor states, self-similarity, and sensitivity to noise.

Thus, this book emphasizes that biology, as does any other complex system, possesses both microscopic (single-cell) and macroscopic (population-average cell) dynamics. The well-coordinated response in the synchronization of yeast populations, neuronal signaling, persistence mechanisms of bacteria, and collective decisions in ants are good indications that the single-cell/animal noise could cancel out when ensembles of cells/animals are formed to generate a stable and robust macroscopic response. Combining cell population and single-cell behaviors suggests that biology is regulated by deterministic governing equations and is sensitive to parameter variations (noise) over a specific range, as witnessed in other disciplines such as physics, chemistry and engineering.

I believe this book provides the reader key insights into the microscopic and macroscopic behavior of living cells. Nevertheless, there are still myriad cellular processes that cannot be represented or understood by physical laws or statistics.

Another challenge is that the experimental data generated for analysis are still highly limited, both in terms of space and time information. As biologists become more and more confident with the power of multidisciplinary contributions, the future looks optimistic for continuous successes in unlocking further secrets governing the self-organizing nature and complex behaviors of living systems.

ERRATUM

Chapter 2
Perturbation-Response Approach
for Biological Network Analysis

DOI 10.1007/978-1-4614-7690-0_14

In the original publication of the print and online versions of this book, equation 2.7 is incorrect in chapter 2 page 21. The correct equation is given below.

$$\frac{\partial \delta X}{\partial t} = \frac{\partial F(X)}{\partial X}\delta X + \frac{\partial^2 F(X)}{\partial X^2}\delta X^2 + \dots \tag{2.7}$$

Index